
**Studies of the Machine Induced
Background, simulations for the
design of the Beam Condition
Monitor and implementation of
the Inclusive ϕ Trigger at the
LHCb experiment at CERN.**

Dissertation

Zur Erlangung des akademischen Grades
Doctor rerum naturalium
(Dr. rer. nat.)
vorgelegt von
Magnus Hov Lieng
geboren am 12.07.1980 in Oslo, Norwegen

Lehrstuhl für Experimentelle Physik 5
Fakultät Physik
der Technischen Universität Dortmund

Mai 2011

1. Censor: Prof. Dr. Bernhard Spaan
2. Censor: PD. Dr. Reiner Klingenberg

Date of submission: 06. May 2011

Abstract

LHCb is one of the four major experiments of the LHC at CERN, built to perform precision measurements of CP violation and rare decays. In order to protect the sensitive elements of the experiment from adverse beam conditions the Beam Condition Monitor has been created. Such conditions increase the particle flux arriving from the LHC, known as Machine Induced Background. These particles interfere with the experiment, for example through the physics trigger.

In this thesis software development and simulations for the design and validation of the Beam Condition Monitor is shown, ranging from LHCb-specific algorithm implementation to beam dump threshold determination. Furthermore, software development in order to attain a complete simulation chain of machine induced background is shown. The results of these simulations are compared to early data collected at LHCb. Lastly, the development and implementation of the Inclusive ϕ trigger line for the High Level Trigger is presented. This line aims to reconstruct and select the two prong decay $\phi \rightarrow K^+K^-$, where ϕ is a daughter of a B-meson decay. This chain is characteristic of several key channels of the LHCb physics programme.

Contents

1	Introduction	1
2	The Large Hadron Collider	3
2.1	Machine Parameters and Running Modes	4
2.2	Beam Halo	5
2.3	IR3: Momentum Cleaning Section	6
2.4	IR6: Beam Dump Section	6
2.5	IR7: Betatron Cleaning Section	7
3	The LHCb Experiment	8
3.1	CP Violation	8
3.2	The CKM Matrix	9
3.3	Physics Measurements at LHCb	10
3.4	Design of the LHCb Experiment	13
3.5	The LHCb Sub-Detectors	14
3.5.1	The Vertex Locator	15
3.5.2	The Ring Imaging Cherenkov Detectors	16
3.5.3	Tracker Turicensis	18
3.5.4	The Dipole Magnet	19
3.5.5	The Inner and Outer Tracker	19
3.5.6	The Muon System	19
3.5.7	The Calorimeters	19
3.6	The LHCb Trigger System	20
3.7	The LHCb Software Suite	21
3.7.1	The Gauss Application	22
3.7.2	Event Types	22
3.7.3	Simulated Sample Production	23
4	Machine Induced Background and Related Concepts	25
4.1	The Beam Condition Monitor	26
4.2	The MBXW Compensator Magnets	27
4.3	Apertures	27
4.3.1	Tertiary Collimators	27

4.3.2	Local Apertures	28
4.4	Types of Machine Induced Background	29
4.4.1	Betatron Cleaning Inefficiency	31
4.4.2	LHC-wide Beam-Gas Elastic Interactions	31
4.4.3	Local Beam-Gas Interactions	31
4.4.4	Momentum Cleaning Inefficiency	32
4.4.5	Elastic and Diffractive Interactions at ATLAS	32
5	Machine Induced Background Simulations	34
5.1	Estimation Procedure	34
5.1.1	Proton Loss Estimation	34
5.1.2	Particle Shower Transport	35
5.1.3	Source Rescaling	36
5.2	The Machine Induced Background Generator	36
5.2.1	The MIB Estimate Input Format	37
5.2.2	The TimeCorrSource Tool	39
5.2.3	Gas Profile Rescaling Tool	41
5.2.4	Current Status of LbMIB	43
5.3	Effect of Machine Induced Background	43
5.3.1	Properties of the MIB Estimates	44
5.3.2	Simulated Samples	52
5.3.3	Recorded Data Samples	53
5.3.4	VELO Multiplicity	53
5.3.5	MIB Selection	56
5.3.6	MIB Effect on Trigger	60
5.3.7	MIB Rate Measurements	64
5.4	Status of the MIB Simulation Work	67
6	Simulations Performed for the Beam Condition Monitor	69
6.1	Algorithms and Components Developed for the BCM	69
6.1.1	Extension of the LHCb Detector Description	69
6.1.2	The BCM Specific Simulation Algorithms	70
6.1.3	The Multiple Magnetic Field Service	71
6.1.4	Sensitivity Scan Tool	71
6.1.5	Beam Shape Tool	75
6.2	Simulations for Determining the Optimal BCM Position and Configuration	76
6.2.1	Position and Design of the Downstream BCM	76
6.2.2	Position and Design of the Upstream BCM	77
6.3	Simulations for Determining the Beam-Dump Thresholds	77
6.4	Simulations for Estimating the Covering Range of the BCM	78
6.4.1	Signal correlations between the BCM and sensitive elements at nominal conditions	79
6.4.2	Estimates of the coverage range of the BCM	80
6.4.3	7 TeV Local Beam Scraping, VELO Closed	86

6.5	Status of the BCM at LHCb	89
7	Inclusive ϕ Trigger	91
7.1	The RICH Algorithms	92
7.1.1	Track and Ring Projection	92
7.1.2	Likelihood Optimization	93
7.2	Relevant Physics Channels	93
7.3	Efficiency Determination	94
7.4	Cuts on Robust Tracks for the Inclusive ϕ Trigger	94
7.4.1	Kaon Impact Parameter	95
7.4.2	Kaon Transverse Momentum	95
7.4.3	Kaon Distance of Closest Approach	95
7.4.4	ϕ Measured Mass	95
7.4.5	ϕ Transverse Momentum	96
7.4.6	Cut Optimization	96
7.5	Cuts on Fitted Tracks for the Inclusive ϕ Trigger	98
7.5.1	Kaon Impact Parameter Significance	98
7.5.2	ϕ Vertex χ^2	98
7.5.3	Cut Optimization	99
7.6	Cuts on RICH Information for the Inclusive ϕ Trigger	100
7.7	Sidebands	101
7.8	Timing Issues	101
7.9	Alternative Settings	102
7.10	Status of the Inclusive ϕ Trigger Line	102
8	Conclusions	104
A	Acronym List	106
B	Inclusive ϕ Trigger Optimization Plots for Reduction Factor 50, 100, 200 and 400	108

List of Figures

2.1	The LHC Accelerator	4
3.1	CKM Triangles	10
3.2	CKM Triangle Measurements	11
3.3	$B_{(s)}^0 - \bar{B}_{(s)}^0$ Oscillation Feynman Box Diagram	12
3.4	$B^0 \rightarrow \pi^+\pi^-$ and $B_s^0 \rightarrow K^+K^-$ Feynman Diagrams	12
3.5	$B_s^0 \rightarrow \phi\phi$ Feynman Diagram	13
3.6	bb Pair Production Angles	14
3.7	LHCb Layout	15
3.8	VELO Layout	17
3.9	Cherenkov Angle	17
3.10	The RICH Layout	18
3.11	The LHCb Trigger Scheme	20
3.12	The LHCb MC Sample Simulation Procedure	23
3.13	The LHCb Data Sample Procedure	24
4.1	Machine Elements Close to LHCb	25
4.2	BCM Layout	26
4.3	LHCb Crossing Angle	28
4.4	LHCb Vertical TCT	29
4.5	LHCb Apertures	30
4.6	Quartiary Halo Generation	32
5.1	Proton Loss Map Example	35
5.2	MIB Particle Timing	42
5.3	MIB Radial Distribution	45
5.4	MIB Transverse Distribution	45
5.5	MIB Particle Multiplicity	46
5.6	MIB Particle Time Offset	47
5.7	Multi-Frame Particle Timing at IT	48
5.8	Beam-Gas in LSS Origin Example	51
5.9	Recorded High Multiplicity Event at 450 GeV	54
5.10	Simulated MIB High Multiplicity Event at 450 GeV	55
5.11	Multiplicity of VELO Clusters at 450 GeV	56

5.12	Multiplicity of VELO Clusters at 3.5 TeV	56
5.13	MIB Selection Variables	58
5.14	MIB Selection Efficiency at 3.5 TeV	59
5.15	Track Slope Mix	65
5.16	Radial Distance to IP Mix	66
6.1	LHCb DDDDB Extension	70
6.2	Initial Compensator Magnetic Fields	72
6.3	Current Compensator Magnetic Fields	73
6.4	Beam Scraping Plot	74
6.5	Beam Dump False Positive Probability for RS0 Algorithm	79
6.6	Correlations Between BCM and VELO	80
6.7	450 GeV Beam Scraping Sensitivity	81
6.8	Pilot Bunch Sensitivity	83
6.9	Beam Dump Range, 450 GeV	85
6.10	7 TeV Beam Scraping Sensitivity	87
6.11	Beam Dump Range, 7 TeV	88
6.12	BCM Online Monitoring Page	90
7.1	RICH Photons and Reconstructed Rings	92
7.2	Robust Cut Efficiency Plots	97
7.3	Track Fitted Cut Efficiency Plots	99
7.4	RICH Cut Efficiency Plots	100
B.1	Factor 50 Cut Efficiency Plots	109
B.2	Factor 100 Cut Efficiency Plots	110
B.3	Factor 200 Cut Efficiency Plots	111
B.4	Factor 400 Cut Efficiency Plots	112

List of Tables

3.1	The Major Gaudi Applications	21
5.1	MIB Source Re-scalability	36
5.2	CollimatorSource File Format	37
5.3	The New Source File Format	39
5.4	Currently Available MIB Sources	44
5.5	Beam Life-Times	48
5.6	Fraction of Proton Losses on the IR8 TCTs	49
5.7	MIB Particles per Lost Proton	49
5.8	MIB Flux from Global Losses	50
5.9	MIB Particles per Lost Proton for LSS BG	51
5.10	MIB Particles flux for LSS BG	51
5.11	Cut Efficiencies at 3.5 TeV	59
5.12	Cut Efficiencies at 450 GeV	60
5.13	450 GeV L0 Trigger Efficiencies total and per Line	61
5.14	3.5 TeV Early L0 Trigger Efficiencies per Trigger Category	62
5.15	3.5 TeV Late L0 Trigger Efficiencies per Trigger Category	63
5.16	7 TeV L0 Trigger Efficiencies per Line	64
5.17	Beam-Gas Fractions from Difference Minimization	65
5.18	Beam-Gas Fractions from Cut Based Approach	67
6.1	Beam Parameters	75
6.2	Average BCM Signal per Sensor at Nominal Conditions	78
6.3	450 GeV Beam Scraping Energy Deposition	82
6.4	7 TeV Beam Scraping Energy Deposition	86
7.1	Robust Cut Values	96
7.2	Robust Cut Efficiencies	97
7.3	Track Fitted Cut Values	99
7.4	Track Fitted Cut Efficiencies	100
7.5	RICH Cut Efficiencies	101
7.6	Overall Inclusive ϕ Cut Efficiencies	101
7.7	Alternative Cut Values	103
7.8	Alternative Inclusive ϕ Cut Efficiencies	103

Chapter 1

Introduction

Though the existence of antiparticles has been known since the discovery of the positron in 1932, still today, 80 years later, questions remain with respect to the difference between matter and antimatter. Astronomical data indicates that the whole universe, not just our corner of space, is dominated by matter. It is believed that a matter/antimatter equilibrium existed directly after the point of generation, i.e. the big bang, and the following physical processes have biased this state to the benefit of matter. The asymmetry is measured through the ratio of baryonic matter to photons, as matter-antimatter annihilation results in photon production. According to measurements performed by the WMAP experiment, the asymmetry is of the order of 10^{-10} [1].

In 1967 Andrei Sakharov proposed three conditions that must be fulfilled in order to account for the dominance of matter in the universe as we know it [2]. These are the violation of the baryon number, interactions occurring out of thermal equilibrium and the existence of CP violation.

In the Standard Model of particle physics this CP violation is parametrized in the form of the so called CKM matrix and multiple experiments have been dedicated to its measurement. However, current results show that even though CP violation exists in the standard model, its measured value is far too small to account for the observed inequality [3, 4].

The LHCb experiment at the Large Hadron Collider (LHC) at CERN in Geneva has been created in order to investigate this effect further. This task is two-fold. Firstly further precision measurements can over-constrain the parameters of the standard model, checking its self-consistency. Secondly the investigation into rare decays can give indications of new currently unknown physics effects, which can potentially contribute to the observed discrepancy. The LHCb experiment is primarily designed to investigate the charm and beauty quark sector.

The LHC, and LHCb, was successfully commissioned in October 2009 and is currently running, producing data for the various measurements. In addition to the desired interactions between the two beams at the interaction point inside the experiment, a certain particle flux due to machine induced background (MIB) is expected to enter the LHCb cavern. This background is a result of several sources, ranging from interactions

with gas residue inside the beam pipe to inefficiencies in the collimation system. Particles of this sort are liable to interfere with the experiment, and thus an understanding of their flux and physical properties is of importance.

As the accelerator runs at an unprecedented beam energy and current, adverse beam conditions or component failure can cause an increase in the machine induced background or result in direct proton losses as the beam core attains an incorrect orbit and scrapes on machine apertures. To protect LHCb against such effects a device called the beam condition monitor (BCM) has been created. It consists of multiple diamond sensors located close to the beam line and has been designed to order the removal of the beams in case of dangerous radiation conditions, thus protecting other more sensitive components of the experiment. Furthermore, unlike the standard LHCb detector systems, the beam condition monitor is constantly active. It can thus aid in the understanding of machine induced background during periods of unstable beam conditions, as for example during energy ramp-up.

The expected proton-proton interaction frequency in the LHCb at the ultimate design settings is of the order of 15 MHz. Hardware, software and cost limitations hinders data from all events to be saved. As such, a multi-stepped trigger system is used. The first trigger level, Level Zero, is hardware based and reduces the event rate output to 1 MHz. Surviving events are passed to an online computer farm, running the High Level Trigger. This software trigger reduces the rate in two steps, first to 30 kHz and finally 2 kHz. These events are saved for further processing.

The inclusive ϕ trigger is a selection line in the last step of the High Level Trigger. This trigger aims at selecting ϕ mesons having decayed into two kaons, itself resulting from a B-meson decay. Several key channels of the LHCb physics programme displays this characteristics, including $B_s \rightarrow \phi\phi$ currently under study at TU Dortmund [5].

The work contained in this thesis is threefold. After the introduction of the various relevant concepts and components in chapter 2, 3 and 4, investigations into the machine induced background will be shown in chapter 5. This covers the implementation of tools and algorithms needed to simulate the transport and interactions of such particles, as well as estimation of the resulting particle flux and its impact on the LHCb experiment. Where possible the simulations are compared to the currently available data samples.

Secondly, in chapter 6, the simulation work performed in connection with the design and deployment of the beam condition monitor is covered. This involves estimates of cover range, correlations with other detectors as well as beam dump threshold determination.

Lastly in chapter 7 the design and optimization of the inclusive ϕ trigger line of the LHCb high level trigger will be shown. This includes estimation of rates and efficiency for various versions of this trigger line.

Chapter 2

The Large Hadron Collider

The Large Hadron Collider (LHC) [6, 7] is a circular particle accelerator located at the European Organization for Nuclear Research (CERN) in Geneva, Switzerland. With a circumference of 27 km it is the largest of its kind and has been designed to run at an unprecedented particle beam energy of 7 TeV. In order to achieve this goal over 1600 superconducting magnets are utilized, making the LHC is the largest cryogenic facility in the world.

As the name indicates, the LHC is a hadronic machine, primarily accelerating two counter rotating beams of protons, though modes using nuclei are also possible. For this thesis only proton runs are of interest, and thus any reference to the beams assume proton beams unless otherwise indicated.

Having been built as a replacement of the Large Electron Positron Collider (LEP), the LHC has inherited part of the infrastructure of this machine, most notably the tunnel in which it is located. This tunnel is, as mentioned, of a circular design and is located at a depth of between 50 m and 175 m. As can be seen from figure 2.1 there are 8 access points distributed around the ring referred to as Interaction Regions (IR). These regions follow an numbering scheme where the numbers increment in the revolution direction of beam 1. This beam turns clockwise in the accelerator when viewing the LHC from above. Furthermore the designation of the tunnel sections are given as a combination of the two points to which it connects. Thus point 1 is connected to point 2 through tunnel section 12 (one-two, not twelve). Listed ascending order, from IR1 to IR8, the systems located at the various interaction regions are:

- IR1** The ATLAS experiment
- IR2** The ALICE experiment
- IR3** Momentum cleaning
- IR4** Beam acceleration
- IR5** The CMS experiment
- IR6** Beam dump
- IR7** Betatron cleaning
- IR8** The LHCb experiment

For this thesis the LHCb experiment is of main interest and will be further investigated in section 3, however in order to understand certain aspects of this thesis, beam halo buildup, the betatron cleaning, momentum cleaning and beam dump systems will be briefly introduced.

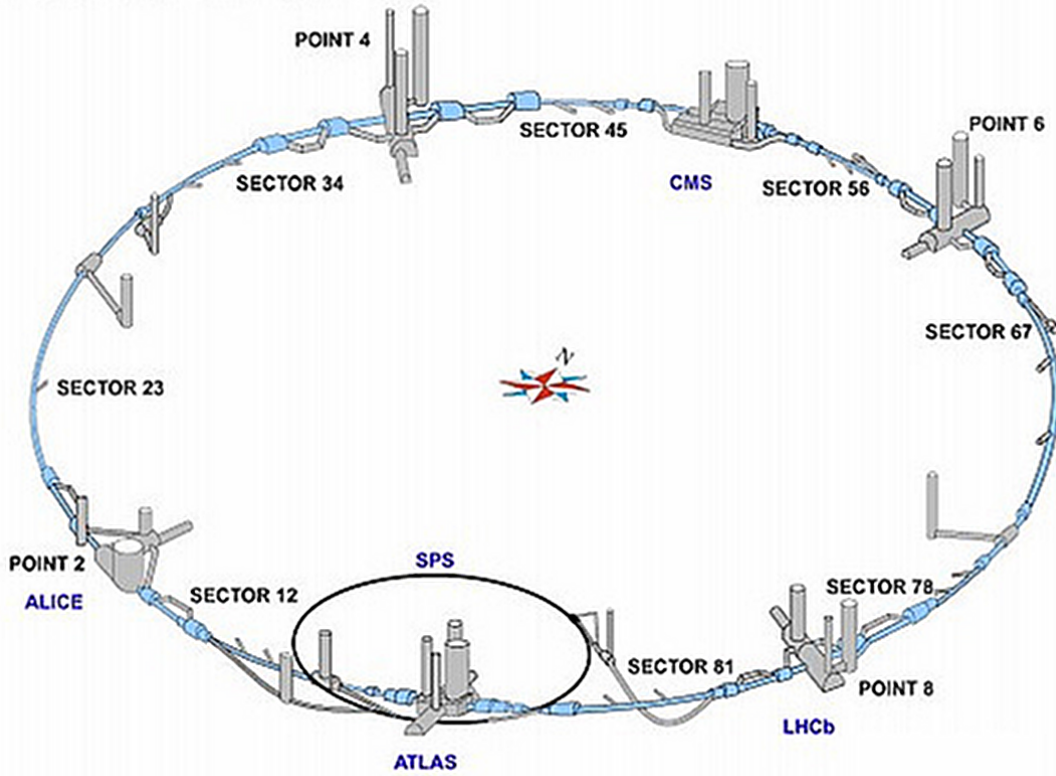


Figure 2.1: The LHC accelerator. The underground complex contains the accelerator ring as well as regions for beam cleaning, acceleration and dumping. At four of the interaction regions, or access points, the major experiments ATLAS, CMS, LHCb and ALICE are located. [8]

2.1 Machine Parameters and Running Modes

The LHC beams consist of multiple bundles of protons referred to as bunches. At regular intervals in the beam, locations exist where proton bunches can be retained. These are referred to as Radio Frequency (RF)-buckets and can be filled or not depending on whether protons reside in it or not. The nominal RF-bucket crossing frequency, or machine frequency, seen from a fixed point along the accelerator is 40.08 MHz. The orbital frequency of a bunch, however, is 11.245 kHz.

The LHC design specifications accommodate two beams of protons with an energy of up to 7 TeV contained in 2808 bunches with a nominal population of 1.15×10^{11}

protons. This mode is referred to as nominal and results in a bunch crossing frequency of up to 31.6 MHz. This number is lower than the 40 MHz of the machine frequency due to the fact that not all RF-buckets can be filled in order to accommodate for a beam abort gap. This concept will be further explained in section 2.4.

Before each run a small (5×10^9 protons) 450 GeV bunch is injected in order to confirm that all machine settings are within the safe range. The size of this bunch has been chosen such that it can be lost instantly and completely at any aperture without causing damage to nearby components. This energy level was also used for the first data taking in 2009, though with a varying number of bunches. Through most of 2010 a beam energy of 3.5 TeV was used. The number of bunches as well as bunch population varied over this time period, however, with a trend of increasing current.

7 TeV beam energy was up till 2009 the standard mode used for simulations and estimate productions. As such many of the results presented in these thesis are obtained at this energy level. When it was known that a lower energy run would be conducted, the focus shifted to 450 GeV and 3.5 TeV. As a result, more estimates and simulations exist for 7 TeV than for the other energy levels, while on the other hand the 450 GeV and 3.5 TeV samples have the benefit of comparison with real data.

In this thesis all three modes will be addressed, though to larger or lesser degree depending on the subject at hand.

2.2 Beam Halo

In order to understand the design and usage of the beam cleaning sections the concept of beam halo must be introduced. Beam halo is defined as protons accompanying the beam, which have an adverse orbit and/or are off-momentum. Such protons can attain large offsets in the traverse or longitudinal direction with respect to the bunch centroid and are thus eligible to interact with the various machine apertures, resulting in energy deposition on the related component.

As the LHC is a super conducting machine, the majority of the magnets need to be kept at cryogenic temperatures. A highly populated halo leads to excessive particle loss, and thus high energy deposition in the cold elements. The resulting heating can cause a local loss of superconductivity forcing the magnet to be quenched in order to avoid damage to the affected region. In addition to aborting the current run, such an action requires a machine stop until cryogenic temperatures are again reached. Understandably, in order for the LHC to be a reliable machine with a high availability, the halo must be kept under control. This is done through the use of various beam cleaning systems. Furthermore, secondary particles resulting from halo interacting on various machine components can interfere with the experiments, thus a clean beam is also beneficial for good physics measurements.

Several beam dynamic processes are involved in the continuous halo buildup. These include synchrotron radiation, intra-beam scattering, Touschek scattering and others [9]. Synchrotron radiation cause energy loss through the emittance of photons in magnetic fields. Intra-beam and Touschek scattering are involve proton-proton in-

teractions in the beam where the first couple particle momenta and the second cause a momentum transfer from transverse to longitudinal phase space.

The size and impact of these factors depend on the design of the machine as well as run specific parameters. In this document the aforementioned beam halo is referred to as primary while secondary, tertiary and quadriary refers to halo surviving the various stages of the beam cleaning systems. I.e. the primary halo is cleaned by the primary cleaning system, resulting in a potential secondary halo of surviving particles. As will be described in later chapters, the quadriary halo arriving from the tertiary cleaning systems are of interest for LHCb and will be studied in this thesis.

2.3 IR3: Momentum Cleaning Section

As the name indicates the Momentum Cleaning Section [6] has been designed to remove off-momentum particles from the beam before they are lost in the superconducting components of the LHC arcs.

Momentum cleaning is performed by placing the collimators in an area with high dispersion and small optical beta function [10]. In such areas the off-momentum protons are radially spread away from the beam centroid, while the bunch itself is kept tight. The spread protons are scattered by a set of primary collimators and are absorbed by the secondary. In addition absorbers, as the name implies, are present to absorb the resulting particle shower.

The opening of the collimators jaws depend on the machine mode, however, the secondary collimators are always located in the shadow of the primary. Only protons have been scattered by the primary are eligible to strike the secondary. By design, particles with a momentum offset of more than $\pm 1 \times 10^{-3}$ with respect to the nominal are eligible to be absorbed. The halo surviving this process is called the tertiary momentum halo.

2.4 IR6: Beam Dump Section

The beam dump section [6] contains the systems responsible for aborting the beam from the accelerator both in the case of an incident and at the end on a normal run. Both beams have a non-populated bunch gap, allowing the kicker magnets to ramp up and direct the beam out of the main ring. This means that a dump can only be performed once per turn of the beam. A dumped beam is defocused and deposited in a water cooled graphite block surrounded by iron and concrete.

A system called the Beam Interlock System (BIS) [11] is responsible for triggering a beam dump in the case of a beam incident or a major malfunction. As indicated by the name, it works as an interlock, consisting of an uninterrupted current loop. Various systems are connected serially to this loop, and resultingly any component can break the loop causing the beams to be dumped.

2.5 IR7: Betatron Cleaning Section

Protons radially offset from the beam center obtain oscillations around this reference orbit. This is known as the betatron oscillations and the amplitude of these oscillations can increase over time as a result of the non-ideal machine optics.

The betatron cleaning section [6] is located at IR7 right in front of the LHCb experiment w.r.t. beam 1. Like the momentum cleaning, this section contains primary and secondary collimators, responsible for removing protons with a large transverse orbit. That is, protons that move too far out from the center of the beam are eligible to strike the jaws of the collimators and thus be removed from the beam. Complementary to the momentum cleaning, the betatron cleaning collimators are located in an area of low dispersion.

The primary collimator system consists of a vertical, horizontal and skew collimator, scraping off the respective halo components, followed by a set of absorbers and secondary collimators. Like for momentum cleaning the secondary collimators lay in the shadow of the primary, and the opening depends on the current machine mode. The surviving halo is referred to as the tertiary betatron halo.

Chapter 3

The LHCb Experiment

The LHCb experiment has been designed to investigate CP violation (CPV) by performing precision measurements of the CKM matrix and searching for new physics in rare decays. These concepts will be introduced in the two following sections while section 3.3 shows a few of the decay processes relevant to the experiment. Section 3.4 and 3.5 cover the concept and features of the LHCb detector including various major components of the experiment. The trigger system and experiment specific software is introduced in section 3.6 and 3.7, respectively.

3.1 CP Violation

In order to understand the concept of *CP violation* one must first introduce C, P and CP *symmetries* and their implications. A symmetry exists if the chosen transformation can be applied to a given state and the resulting state is physically equivalent to the original. Conversely a violation implies that some physical process is different in the two states, for example decay rates.

The transformation C represents the charge conjugation of a the state. When this transformation is applied, all additive quantum numbers are inverted, i.e. the sign is changed. Additive quantum numbers include, amongst others, electric and flavor charge. This transformation in effect changes a particle into its anti-particle.

P or parity transformation involves the inversion of all spatial directions. The state is mirrored on all axis, turning up to down, left to right and forward to backward. This is also known as point mirroring. Applying this transformation to a particle results in the inversion of the helicity from left-handed to right-handed and inversely.

These two symmetries are, however, maximally violated in the neutrino sector. All neutrinos are left-handed while all anti-neutrinos are right-handed. The application of C transformation on a left-handed neutrino returns a left-handed anti-neutrino, while the application of P transformation on the same particle returns a right-handed neutrino. Neither of these two states have been shown to exist in nature.

If both C and P transformations are performed simultaneously, a left-handed neutrino results in a right-handed antineutrino, which does exist. This CP symmetry

was believed to be conserved until 1964 when CP violation was discovered in neutral kaons [12]. Neutral kaons can transform into their anti-particles and back again, and it was discovered that this process had a bias in one direction, leaving an inequality between the two states, thus the states are not equivalent. The parameterization of this effect is realized through the CKM matrix in the Standard Model.

3.2 The CKM Matrix

The electroweak interaction does not couple to the mass eigenstates of the quarks, but rather to an electroweak eigenstate. The relation between the mass and electroweak states can be parameterized using a transformation matrix. The standard convention is to link the down quark states with a 3×3 unitary matrix called the Cabibbo-Kobayashi-Maskawa (CKM) matrix [13]. This is depicted in equation 3.1.

$$\begin{pmatrix} d' \\ s' \\ b' \end{pmatrix}_{\text{weak}} = V_{CKM} \cdot \begin{pmatrix} d \\ s \\ b \end{pmatrix}_{\text{mass}} = \begin{pmatrix} V_{ud} & V_{us} & V_{ub} \\ V_{cd} & V_{cs} & V_{cb} \\ V_{td} & V_{ts} & V_{tb} \end{pmatrix} \begin{pmatrix} d \\ s \\ b \end{pmatrix}_{\text{mass}} \quad (3.1)$$

The square of the magnitude of each element V_{ij} is proportional to the probability of conversion from quark mass state q_i to q_j , as well as that of the inverse process. From this follows directly that if the CKM matrix would be a unity matrix, quark conversion could not occur across generations.

Through the assumption that the matrix is unitary, the nine complex parameters can be reduced to five relative quark phases, three angles and a CP-violating phase. The quark phases can be changed or absorbed by rephasing the quark fields. In the standard parameterization, as shown in equation 3.2, the three rotation angles are used in combination with the CP-violating phase δ_{13} . In this nomenclature s_{kl} and c_{kl} represent the sine and cosine of the angle θ_{kl} , whereas k and l stands for the three quark generations. If the CKM matrix was proven not to be unitary this would be an indication of physics beyond the standard model, or new physics. In general the concept of new physics cover all extensions to the Standard Model for example through the existence of a fourth particle generation or super symmetric particles.

$$V_{CKM} = \begin{pmatrix} c_{12}s_{13} & s_{12}c_{13} & s_{13}e^{-i\delta_{13}} \\ -s_{12}c_{23} - c_{12}s_{23}s_{13}e^{i\delta_{13}} & c_{12}c_{23} - s_{12}s_{23}s_{13}e^{i\delta_{13}} & s_{23}c_{13} \\ s_{12}s_{23} - c_{12}c_{23}s_{13}e^{i\delta_{13}} & -c_{12}s_{23} - s_{12}c_{23}s_{13}e^{i\delta_{13}} & c_{23}c_{13} \end{pmatrix} \quad (3.2)$$

The matrix is often approximated through the Wolfenstein parameterization [14] related to the standard representation through the equations 3.3. This simplifies the CKM matrix to equation 3.4, where $\lambda \approx 0.23$ and works as an expansion parameter. In this parameterization CPV is present as long as $\eta \neq 0$.

$$\begin{aligned}
\lambda &= s_{12} \\
A\lambda^2 &= s_{23} \\
A\lambda^3(\rho - i\eta) &= s_{13}e^{-i\delta_{13}}
\end{aligned} \tag{3.3}$$

$$V_{CKM} \approx \begin{pmatrix} 1 - \lambda^2/2 & \lambda & A\lambda^3(\rho - i\eta) \\ -\lambda & 1 - \lambda^2/2 & A\lambda^2 \\ A\lambda^3(1 - \rho - i\eta) & -A\lambda^2 & 1 \end{pmatrix} + \mathcal{O}(\lambda^4) \tag{3.4}$$

Unitarity enables the matrix to be broken down into multiple equations, where six of these contain the complex phase and can be represented as triangles in the complex plane. Two of these (equation 3.5 and 3.6) are particularly useful as all terms are of the same order, $\mathcal{O}(\lambda^3)$. The triangles are thus not flattened through the expansion factor.

$$V_{ud}V_{ub}^* + V_{cd}V_{cb}^* + V_{td}V_{tb}^* = 0 \tag{3.5}$$

$$V_{tb}V_{ub}^* + V_{ts}V_{us}^* + V_{td}V_{ud}^* = 0 \tag{3.6}$$

Figure 3.1 shows the related triangles in the complex plane. The independent measurement of the angles and side lengths can over-constrain the model by searching for discrepancies between the measurements. The current measurements of the CKM triangle as represented by equation 3.5 is shown in figure 3.2. The LHCb experiment has been designed to improve the measurement these parameters as well as searching for effects not consistent with the Standard Model (new physics).

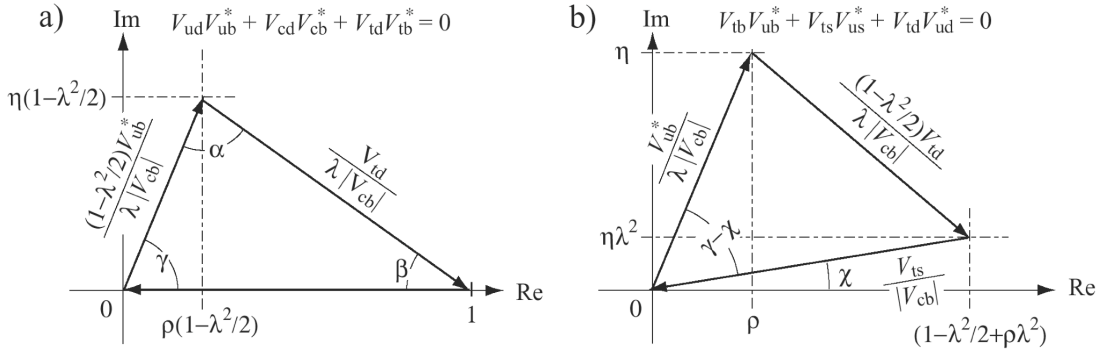


Figure 3.1: The CKM triangles represented by equations 3.5 and 3.6. [15]

3.3 Physics Measurements at LHCb

The LHCb experiment has primarily been constructed to investigate CPV in B_d , B_s and D meson decays. During proton-proton interactions at the LHC such particles are

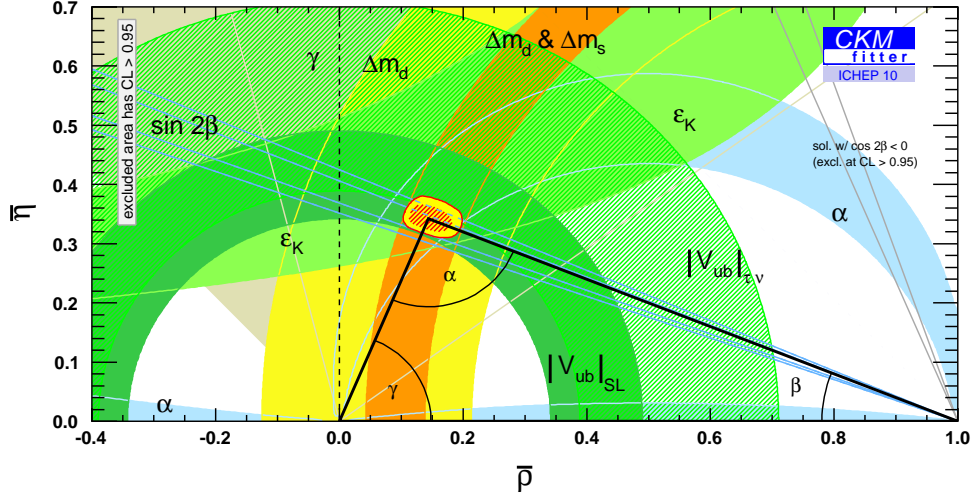


Figure 3.2: The CKM triangle measurements as of 2010 [16] for the triangle represented by equation 3.5.

created in copious amounts, and the challenge consists in correctly reconstructing the decay chain using the electronic signals left in the various sensors of the experiment. In particular the heavier mesons like B_s will have a significantly higher production rate than currently seen at other accelerators.

By analyzing the frequency and characteristics of various decay chains relevant parameters can be measured, whether related to standard flavor physics, CP violation or physics beyond the Standard Model. Some key measurements for the LHCb experiment are described in [17].

The oscillations between a neutral meson state and its charge-conjugate, in combination with their respective decays, can be used for the time dependent measurement of CPV. In the Standard Model this is described through Feynman box-diagrams shown in figure 3.3. In the case of new physics further processes could contribute, typically by the appearance of beyond Standard Model particles inside the box. In such an event, the measured values of the CKM parameters would be modified accordingly.

Decays can occur through tree level processes, loop level (penguin) processes or both as show in figure 3.4. Tree level processes are direct decays, whereas a penguin decay contains one or more loops. New physics can modify the loop by the existence of beyond the standard model particles. Measurements of, in particular, the CKM angle γ can be conducted purely at the tree level as well as with loops involved. This gives the possibility of checking for inconsistencies between the two measurements potentially caused by the existence of new physics.

Certain rare decays like $B_s \rightarrow \phi\phi$ can not occur at the tree level and thus only have higher level contributions, dominated by single loop processes. This is a theoretically clean decay, where investigations into the existence of new physics can be

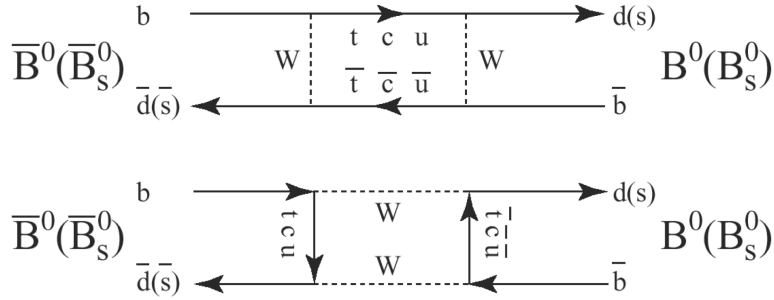


Figure 3.3: $B^0 - \bar{B}^0$ oscillation Feynman box diagram as described by the standard model. [15]

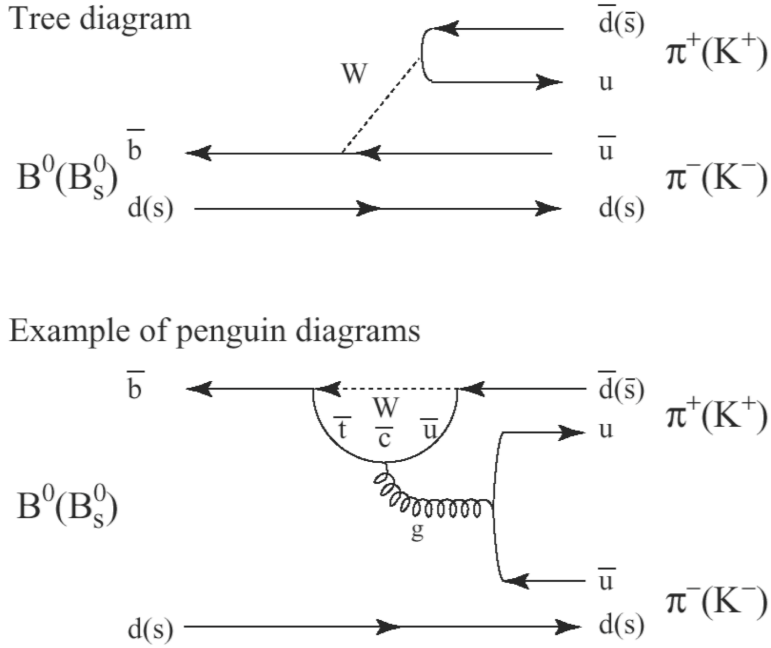


Figure 3.4: $B^0 \rightarrow \pi^+ \pi^-$ and $B_s^0 \rightarrow K^+ K^-$ Feynman diagrams. Both a tree level and penguin diagram contribute to the decay. [15]

performed through the analysis of interference between $B_s \leftrightarrow \bar{B}_s$ oscillations and the decay. Currently preparations for the analysis of this channel are being performed at TU Dortmund [5]. In order to attain the statistics and measurement accuracy needed to improve our current knowledge of CPV and rare decays, the LHCb experiment has been designed and built.

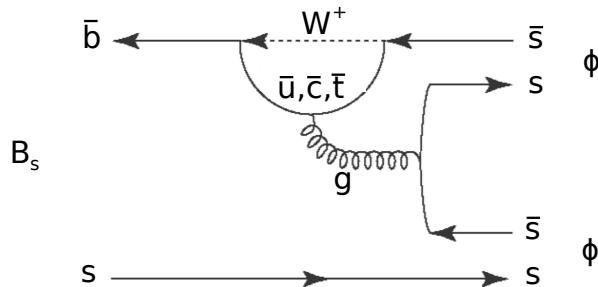


Figure 3.5: $B_s^0 \rightarrow \phi\phi$ Feynman diagram. No tree level decay is allowed.

3.4 Design of the LHCb Experiment

As previously mentioned, LHCb was created to investigate CPV and rare decays. As the name indicates the physics program is dominated by the b-sector, i.e. the decay of hadrons containing one or more bottom quark. Major features of the experiment is excellent vertex resolution, enabling precision measurement of decay times, and reliable particle identification, enabling the differentiation of various particle species.

Unlike the larger experiments ATLAS and CMS, the LHCb does not aim to maximize the overall luminosity, but rather optimize to one proton-proton interaction per bunch crossing. This is realized through a local beam tuning system. The advantages of such a scheme is the simplification of event reconstruction and analysis, and the reduction of radiation damage. In addition this means that the LHCb will be able to reach its design luminosity at an early stage.

At the design luminosity of $2 \times 10^{32} \text{cm}^{-2} \text{s}^{-1}$ about 10^{12} $b\bar{b}$ pairs are expected to be produced at the LHCb per LHC year (defined as 10^7 s run time), making it the most copious source of b-mesons and -baryons in the world.

In LHC proton-proton interactions $b\bar{b}$ pairs are to a large degree produced at low angles with both quarks contained in the same hemisphere (see figure 3.6). Because of this the LHCb experiment is designed as a single armed spectrometer covering the angle from 10 mrad to 300 mrad in the “bending” plane (horizontal) and from 10 mrad to 250 mrad in the “non-bending” plane (vertical). Bending and non-bending refer to the direction of the field of the LHCb main dipole magnet.

As the cavern containing LHCb has been inherited from the LEP experiment DELPHI, certain design limitations presented themselves. Most notable of these is the fact that the interaction point (IP) of the experiment is not located at the nominal point (centrally in the cavern), but is rather offset by 11.25 m. This can clearly be seen from figure 3.7 where the shape of the cavern is indicated together with the experiment.

The coordinate system used for LHCb is anchored to the interaction point of the experiment, defining the origin. For completeness it is worth to mention that this represents the position $s = 23315.38$ m in the LHC coordinate system, where s defines the distance from IP1 along the beam line in the direction of beam 1. Furthermore the coordinate system is a right handed system with the z axis values increasing in the

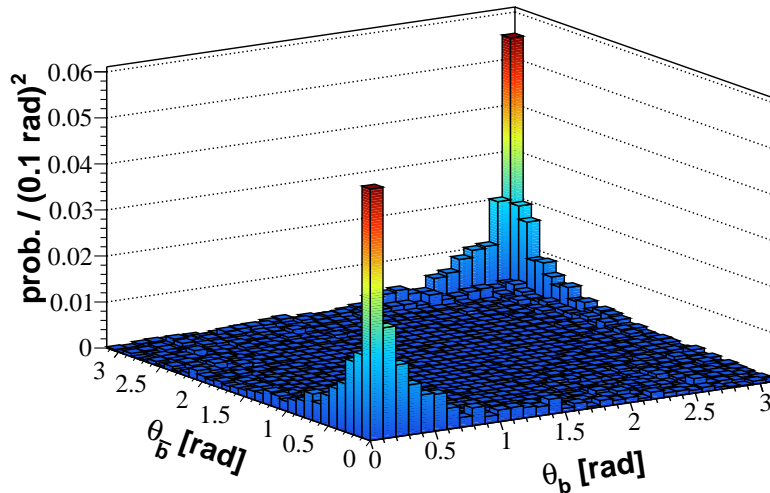


Figure 3.6: $b\bar{b}$ pair production angles at the LHC. The LHCb experiment covers an angle from 10 mrad to 250 (300) mrad. [18]

flight direction of beam 1 (i.e. clockwise in the LHC when seen from above), the y axis vertically pointing towards the sky and the x axis horizontally pointing away from the centre of the LHC ring [19]. The terms upstream and downstream will be used in this thesis to indicate coordinates at diminishing or increasing z -value, respectively.

Figure 3.7 shows the LHCb layout. The figure uses the LHCb coordinate system, thus one can see how the origin is offset with respect to the center of the cavern. The LHCb experiment is constructed out of several sub-detectors. The concept and function of these devices is explained in the following section.

Further information on the experiment can be attained from [15] and [20].

3.5 The LHCb Sub-Detectors

As mentioned, LHCb is built up of several sub-detectors, each specifically designed for a given task. Due to the single arm spectrometer design of the experiment, these sub-detectors are situated in a row along the z direction. Moving from the position of the IP towards higher z values these sub-detector (and other major components) are as follows:

- Vertex Locator (VELO)
- Ring Imaging Cherenkov Detector 1 (RICH1)
- Tracker Turicensis (TT)
- The Dipole Magnet
- Inner and Outer Tracker (IT/OT)
- Ring Imaging Cherenkov Detector 2 (RICH2)

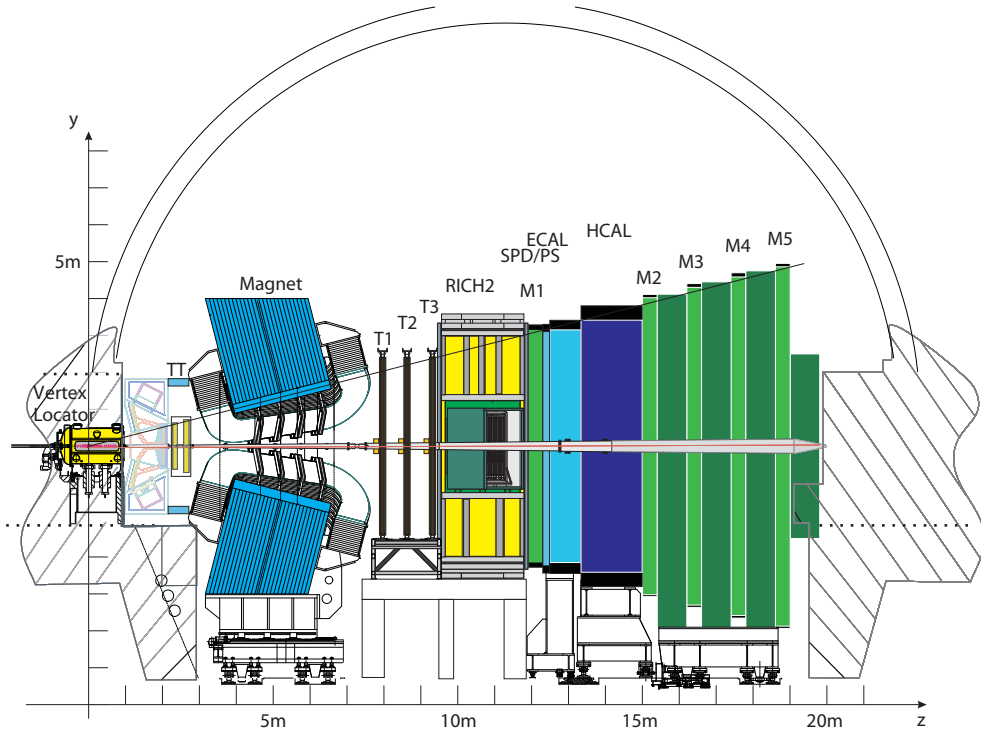


Figure 3.7: The LHCb layout as per technical design report. The detector is shown from the side. [15]

- Muon Station M1
- Scintillator Pad and Pre-Shower Detector (SPD/PS)
- Electromagnetic Calorimeter (ECAL)
- Hadronic Calorimeter (HCAL)
- Muon Station M2 to M5

In addition to these components the beam condition monitor and the compensator magnets will be introduced in the following sections.

3.5.1 The Vertex Locator

The IP is located inside the Vertex Locator (VELO) [21]. This device is a silicon based detector system designed to track particles as they leave the IP with high precision both in time and space. This is realized through the use of 21 VELO stations, arranged along the beam line direction. Each station contains two sensor modules in the shape of a paddle, one on the left and one on the right side of the beam center. Each paddle contains two semicircular silicon strip sensors able to register the traversing charged particles. One sensor registers the radial coordinate of the particle hit while the other

registers the angular, thus, combined with the z coordinate of the paddle, giving the complete cylindrical coordinates.

Unlike the other LHCb sub-detectors, the VELO is located inside the beam pipe, however the sensor modules are contained within a secondary vacuum. This vacuum is contained within two aluminum boxes, dubbed the RF boxes, one on each side of the beam line in the horizontal plane. As a safety measure these boxes can be retracted in the horizontal plane up to 30 mm away from the beam line. Only in the case of a stable beam (physics measurement) are they moved together. This movement system also allows variations in the vertical and horizontal position of the VELO during physics. The VELO can thus center on the interactions even when these occur offset to the nominal IP. The corrugated interface plane between the boxes is referred to as the RF-foil, and provides a hole with a radius of 5 mm for the beams to pass through. The actual active area of the sensors start at a radius of about 8 mm.

21 modules are contained in each box, arranged in a staggered fashion with respect to the other box. This enables the modules to slightly overlap in the horizontal direction, thus assuring full sensor coverage. The arrangement of sensors and RF-foil is shown in figure 3.8. In addition two modules called the Pile Up (PU) are contained in the VELO. These modules only have radial sensors and are used in connection with the trigger system.

Due to the proximity to the beam and the sensor technology utilized, the VELO is the component of LHCb most likely to receive damage in the case of increased radiation levels.

3.5.2 The Ring Imaging Cherenkov Detectors

Downstream of the VELO the first Ring Imaging Cherenkov (RICH1) detector is located [22]. This device, in combination with a second detector (RICH2) located further downstream, performs charged particle identification. In particular, the separation between kaons and pions is important for several physics analysis.

A ring imaging Cherenkov detector works by utilizing the fact that highly relativistic particles traversing a medium where the speed of said particles is higher than the speed of light in the material, results in the emission of photons. The angle, θ , of this light with respect to the line of travel of the particle is given by formula 3.7 and visualized in figure 3.9.

$$\cos(\theta) = \frac{1}{n\beta} \quad (3.7)$$

where n is the refractive index of the traversed material and β is the speed of the particle as a fraction of the speed of light in vacuum. Spherical mirrors are used to collect the light in the shape of a ring, independent of the point of emission along the particles track, and from the radius of the ring one can determine an emission angle. Figure 3.10 shows the RICH1 and RICH2 detectors and the light emission path from a track in RICH1.

In effect the emission angle can be translated into a particle velocity. Combining this with measurements of the momentum of the same particle gives a mass hypothesis,

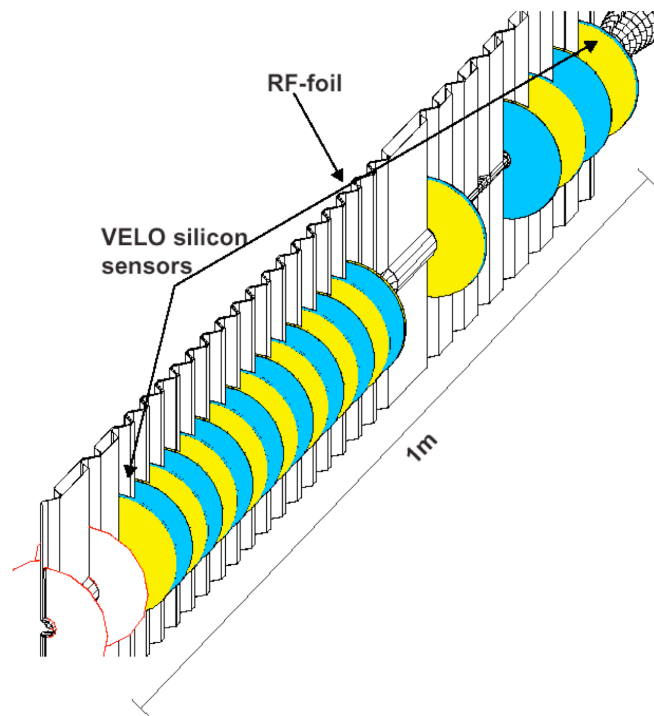


Figure 3.8: The VELO layout along the beam line. The semi-circular sensor modules are shown together with the corrugated RF-foil. The corrugation allows overlap between the left and right VELO sensors. [21]

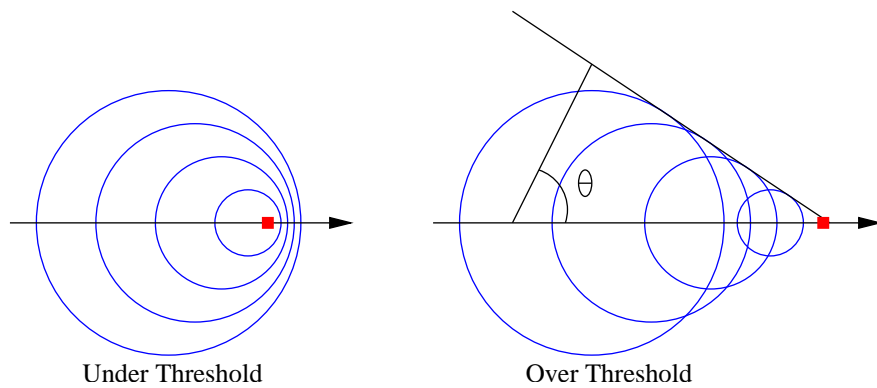


Figure 3.9: The Cherenkov angle. Below the threshold velocity, no cherenkov angle can be attained. At velocities equal to or above the threshold, a “shock front” forms with an angle equal to equation 3.7.

and thus a particle identity hypothesis. The RICH has a kaon identification efficiency of 95% with a misidentification probability of 5% [20] where a pion is mistaken for a kaon.

Three radiators with different refractive indices are used in order to cover a large momentum range. RICH1 covers from 1 to 60 GeV/ c , while RICH2 covers a range from 15 to beyond 100 GeV/ c .

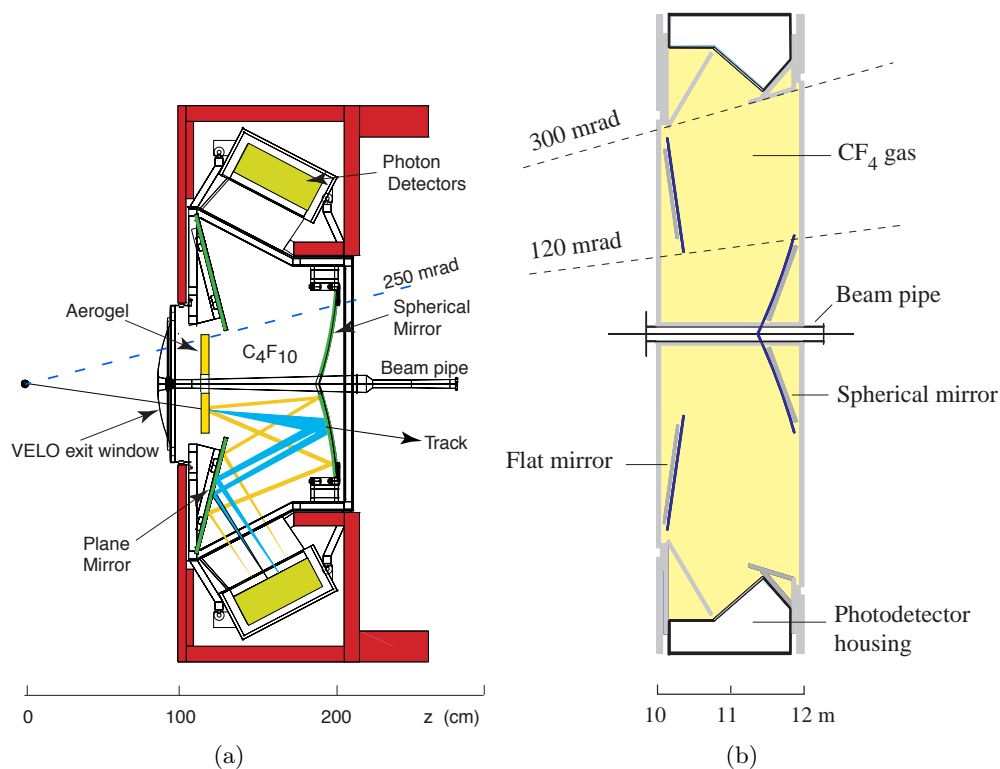


Figure 3.10: The RICH layout as seen from the side. Uni-angular light is emitted along the track. The light is reflected and focused to a ring at the photon detectors with the use of spherical mirrors. Figure 3.10(a) displays the RICH1 while figure 3.10(b) shows RICH2. [22]

3.5.3 Tracker Turicensis

Following the RICH1 the first set of tracking systems is located. This silicon strip based sensor system is called the Tracker Turicensis (TT) (formerly known as the Trigger Tracker) and performs charged particle tracking before the LHCb magnet. It consists of four detector layers where the two first and two last are separated into two stations. The detector layers are arranged in an X-U-V-X scheme, where the X-layers contain vertically arranged sensors while U and V have an angle of respectively -5° and $+5^\circ$ from the vertical. This allows for measurement of the vertical (y) coordinate of particle hits.

The silicon based technology used makes the device vulnerable in unexpected high radiation conditions. As both the VELO and TT are located before the magnet field.

these two detectors allow the reconstruction of largely unperturbed charged particle tracks.

3.5.4 The Dipole Magnet

In order to attain a good momentum measurement for the charged particles, a 4.5 Tm warm dipole is used to bend the tracks [23]. The magnet has a novel splayed design, following the sensitive solid angle of the experiment in order to attain the integrated field strength required. As the magnetic field is predominately vertical, the tracks are bent in the horizontal plane, thus this plane is referred to as the bending plane.

3.5.5 The Inner and Outer Tracker

The inner [24] and outer [25] tracker systems are located directly behind the magnet. This is a system comprised of three stations, each containing an inner (IT) and an outer tracker (OT) where each station has four sensor layers. The IT is located close to the beam line and, as the TT, utilizes silicon based sensors. Further out, where the particle flux is lower, the OT employs drift tubes instead.

For both the IT and OT the X-U-V-X layer scheme is used with angles of 0° , -5° , $+5^\circ$ and 0° with respect to the vertical.

3.5.6 The Muon System

After the aforementioned second Ring Imaging Cherenkov (RICH2) detector, the first muon system [26] detector is located. This consists of triple gas electron multiplier (GEM) sensors. Further muon system stations are located downstream of the calorimeters. These 4 sensor systems consist of multi wire proportional chambers (MWPC) and are separated by iron walls. As the name implies the system is designed to detect and track muons.

3.5.7 The Calorimeters

Between the first and second muons system the calorimeters are located [27]. There are two calorimeters in the experiment. The first is an electromagnetic calorimeter (ECAL) using scintillating tiles in combination with lead plates placed perpendicular to the beam. The energy of electromagnetically interacting particles are measured with this system. The HCAL consists of scintillating tiles and iron plates, however, with the plates put parallel to the beam line.

In addition, placed in front of the two calorimeters are two walls of scintillating sensors interspaced by a lead wall. The sensor wall in front of the lead is called the scintillating pad detector (SPD), while the one behind is the pre-shower detector (PS). Both detectors are divided into several scintillating pads connected to photomultiplier tubes.

3.6 The LHCb Trigger System

With a machine frequency of 40 MHz and an ultimate proton-proton event rate of 15 MHz, the data output stream would be too high to handle both at the level of readout as well as storage. An event output rate of 2 kHz was decided upon, and a multi-level trigger has been implemented in order to select events of interest to the physics program.

The LHCb trigger system [28] is divided into two main parts, the hardware based L0 trigger and the software based high level trigger (HLT). This scheme as well as the average event rates at the ultimate configuration are indicated in figure 3.11. For the 2009/2010 data sets the trigger has been used in various configurations. In this thesis the major features of the trigger setup used will be indicated for the data sets when appropriate.

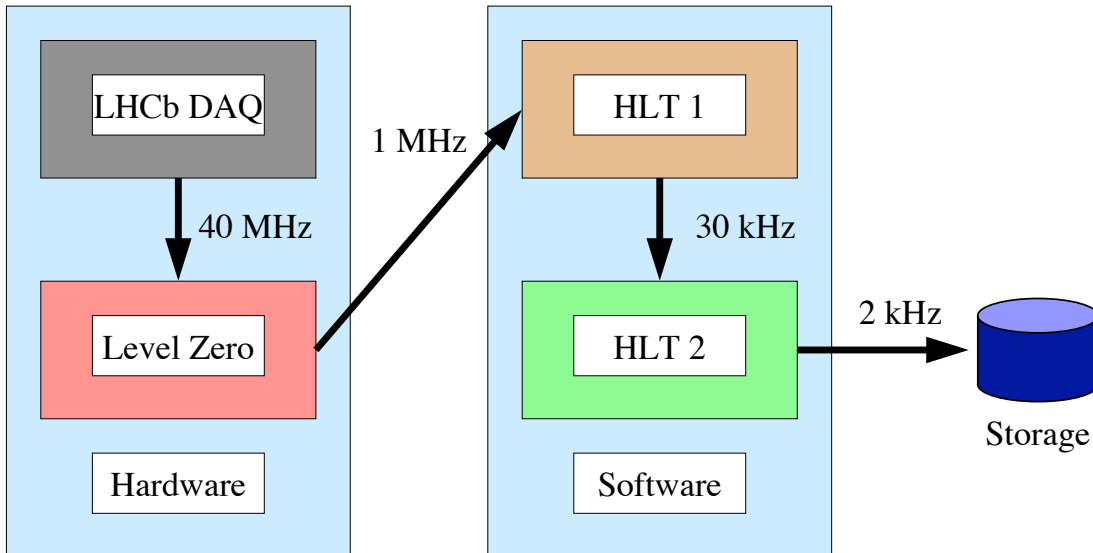


Figure 3.11: The LHCb trigger scheme. The trigger has a hardware and a software stage and reduces the event rate from 40 MHz to 2 kHz.

The L0 trigger is designed to select events showing typical b-decay signatures through simple kinematic and multiplicity cuts using a subset of detectors. The Pile-Up is responsible for rejecting bunch crossings containing more than one inelastic proton-proton interaction, while the calorimeters and muon system searches for decays with high transverse momentum and energy. Running at a the machine frequency of 40 MHz the L0 trigger aims to reduce the event rate to 1 MHz.

The HLT is a software based trigger based on the Gaudi framework [29] (See section 3.7). It runs on the online trigger computer farm and is responsible for reducing the event rate from 1 MHz to 2 kHz. The events are distributed to this farm where they run independently and in parallel to each other. By design the system is divided in two parts, the HLT1 and the HLT2.

Events having survived the L0 trigger are handed to HLT1 where, depending on the signature in L0, the L0 decision is confirmed. This is done by adding information from the VELO and/or tracking stations which was not available to the L0 trigger. Based on this new information the tracks are re-assessed, only keeping those who are deemed interesting. The HLT1 contains multiple trigger lines, each optimized to search for a specific signature. For example there exists a hadronic line, a muonic and di-muonic line, as well as lines for photons, electrons and neutral pions. The cuts and composition of lines in the trigger depend on the version involved. The HLT1 is designed to have an output rate of 30 kHz.

The HLT2 is performs a complete, albeit simplified, reconstruction of the 30 kHz of events. It is designed to resemble the offline reconstruction as far as possible. Like the HLT1, several trigger lines exist, aiming to perform partial (inclusive) or complete (exclusive) physics channel reconstructions.

As an example, the physics channel $B_s \rightarrow J/\psi \phi$ can be triggered through the inclusive channels $J/\psi \rightarrow \mu^+ \mu^-$ or $\phi \rightarrow K^+ K^-$, or exclusively containing the whole chain $B_s \rightarrow (J/\psi \rightarrow \mu^+ \mu^-)(\phi \rightarrow K^+ K^-)$. Depending on the selection in question, several intermediate steps are performed making sure that computing heavy algorithms are executed on the least amount of events.

The 2 kHz output rate of the HLT2 is saved to disk for full reconstruction and further processing.

3.7 The LHCb Software Suite

The LHCb software [30] is based on a framework called Gaudi [29]. This provides the overall software structure ranging from base classes and methods to specific configuration tools. The framework is written in C++ and configured through Python.

In the software suite there are several applications dealing with various aspects of the experiment simulations, data taking, analysis and visualization. The main applications and their purpose are listed in table 3.1.

Table 3.1: The major Gaudi applications and their uses. Further Gaudi applications exist, however are not of relevance for this thesis.

Name	Description
Gauss	Geant4 based particle and detector simulation
Boole	Conversion from simulated data to DAQ-like data
Brunel	Particle decay reconstruction
DaVinci	Particle physics analysis
Moore	Online trigger
Panoramix	Particle and detector visualization

For this thesis the application of main interest is Gauss, though most of the others are also used in one way or the other.

3.7.1 The Gauss Application

Gauss [31] is the LHCb simulation application, based on the Gaudi framework. It consists of two separate steps, namely event generation and detector simulation, and, like all LHCb software, works on an event by event basis.

In the event generation step one or more algorithms are used to create the particles used in the event with physical properties according to the generator involved. Depending on the use case the algorithm involved can vary from a simple “Particle Gun” producing single particles according to the user’s wish, to PYTHIA [32] simulating the physics processes of a proton-proton interaction.

The particles created in the event at the event generation step are handed over to the detector simulation. Using Geant4 [33] as a backend the particles are transported through a model of the LHCb detector, including material, magnetic fields and sensors. Particle decay, interaction with material and bending in magnetic fields are taken into account during the transport.

In particular, information concerning particles traversing sensitive elements of the detector is of interest, and this is thus saved for further processing and comparison with the real experimental output.

3.7.2 Event Types

Depending on the settings and algorithms used in the production of a simulated data sample an event type number is assigned. For this thesis the exact numbering scheme is not of interest, however a general nomenclature must be introduced.

The expression *Minimum Bias* refers to events that have been produced in such a way that they, to our best knowledge (and within reasonable calculation time), correspond to what is expected to be produced by the experiment itself. Various physics processes and branching fractions are taken into consideration, aiming to, as the name indicates, create a sample with as small a bias as possible with respect to the physical reality.

Conversely a *Signal Sample* is a data set where a given particle decay is always present. These samples are created in order to attain a reasonable statistics in the channels investigated. In the standard production these samples are created by repeating the proton-proton interaction until the requested mother particle is generated. This is allowed to decay multiple times until the correct decay chain appears. Additionally, as LHCb is single armed, the topography of the interaction is forced to have the signal decay in the direction of the experiment (i.e. the z -direction is flipped if it occurs in the wrong direction). Furthermore, the decay products must be within the angular acceptance of the experiment. Only when the correct decay and geometry has been attained, are the particles transported. The aforementioned cuts and simplifications have been used in order to reduce the computing time involved in sample production as only relevant decays are allowed to propagate.

For both sample types, multiple proton-proton interactions can occur inside a single event. In the case of signal samples, only one of the interactions need to fulfill the signal

criteria.

In this document samples containing particles which are not arriving from proton-proton interactions are also used. Specifically this involves machine induced background samples and generation of single particles with given kinematic parameters. These will be dealt with in the appropriate chapters. The event type nomenclature and numbering is described in [34].

Additionally the simulated data samples have gone through a long row of improvements and changes. In addition to program version changes, there are several major simulation samples. These are designated with the year of production and have fundamental changes in generators, detector description and data types. For this thesis the data types designated *DC06* and *MC09* are mainly used.

3.7.3 Simulated Sample Production

The production of simulated Monte Carlo (MC) samples is done through the use of several applications. As can be seen from figure 3.12 three applications are used in the production, with a fourth used for the analysis.

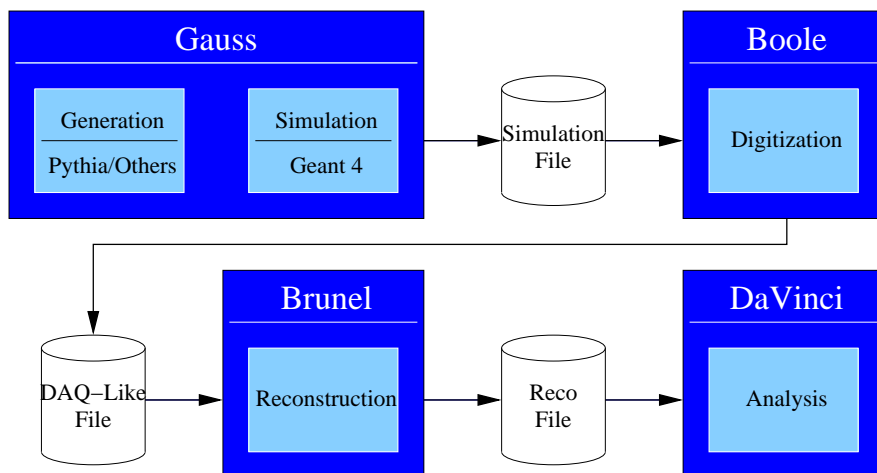


Figure 3.12: The LHCb MC sample simulation procedure. Gauss generates interactions and particles and transports them through the detector description. Boole translates the particle hits into a DAQ-like format. Brunel performs general reconstruction, while the individual analysis are performed in DaVinci.

As mentioned in section 3.7.1, the Gauss application generates the particles and events and transports these through the detector description, giving information about impact points in the various detectors.

The file produced by Gauss is used as input for the digitization application, Boole. In this step the various particle hits on the detector elements are transformed into the detector specific data type. This data type corresponds to the digital output format from the real detector. For example hit coordinates are translated into channel numbers

and ADC values. In addition, effects like crosstalk, noise and calibrations can be folded in at this stage.

Brunel, the reconstruction application, can read both detector data and simulated files as the output from the detector and from Boole should be equivalent. This application combines the detector outputs into tracks and particle candidates, as well as calculating various physical properties for these. The users in general interact with the output files of Brunel as most physics analysis require access to tracks and particles.

Finally DaVinci is used to analyze the reconstructed files. For the investigation of a given decay this involves combining particles and selecting the best constellations according to some criteria, though the specifics of the analysis is left to the user.

For comparison, figure 3.13 shows the corresponding procedure for real data samples. The detector output is read out by the LHCb electronics, at which point the first trigger level also is performed. The Moore application reads the surviving events, performing partial reconstruction and conducting the final level trigger. The triggered events are then reconstructed by Brunel and analyzed in DaVinci just as for the simulated samples.

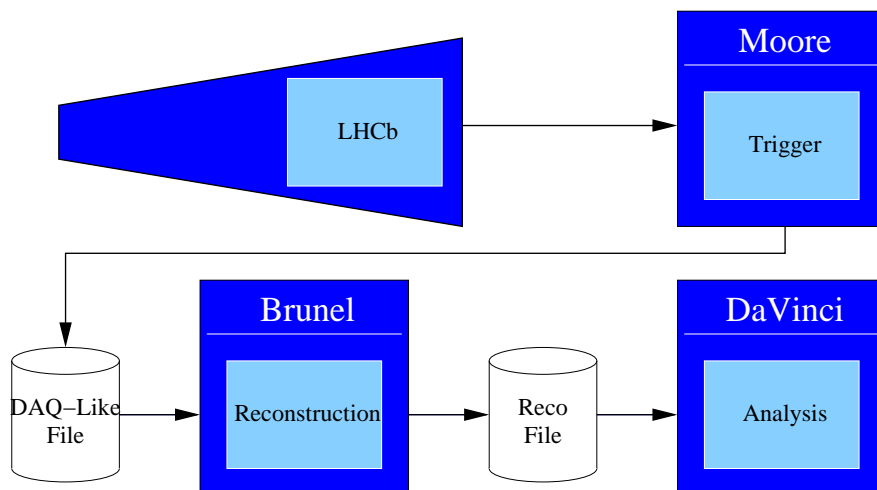


Figure 3.13: The LHCb Data Sample Procedure. The data produced by the LHCb experiment is read out by the LHCb electronics. At this point the first trigger level (L0) is also conducted. Surviving event are read by the Moore application, performing the final triggering (HLT). From this point on the data and follows the same path as the simulated samples, i.e. reconstruction in Brunel and analysis in DaVinci.

Chapter 4

Machine Induced Background and Related Concepts

In addition to the intended proton-proton interactions at the IP, a certain particle flux enters the experiment from other beam related sources. The rate and kinematics of these particles is governed by the LHC machine settings and conditions and is thus referred to as machine induced background (MIB). Further external sources like cosmic radiation are not covered by this definition.

Particles arriving from MIB sources can interfere with the experiment in various ways, ranging from interference with the trigger system and reconstruction to actually damaging sensitive components. As such, estimates of these sources have been conducted and the resulting effects on the experiment investigated.

This chapter covers the concepts and components relevant to the studies of MIB presented in this thesis. Section 4.1 introduces the radiation protection system known as the Beam Condition Monitor, while section 4.2 gives information on the warm compensator magnets close to the experiment. The beam aperture limitations in the region of the experiment are described in section 4.3. These are relevant for the simulations of various MIB sources. The forms of MIB considered relevant for LHCb as well as how they are created, is covered in section 4.4. Figure 4.1 shows the machine elements close to LHCb relevant to this thesis.

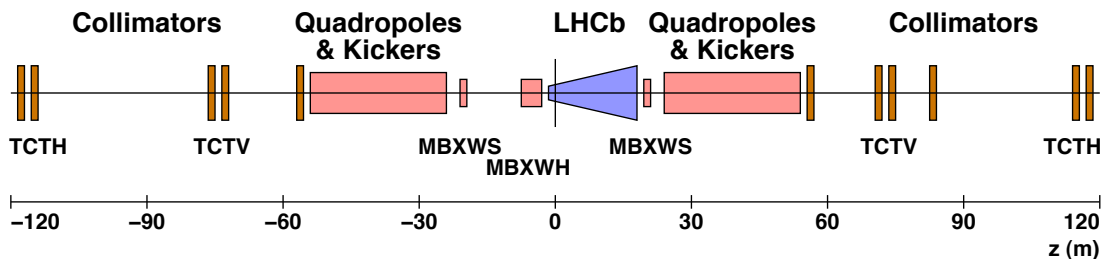


Figure 4.1: Sketch of the machine elements close to LHCb. For this thesis the compensator magnets (MBXW) and tertiary collimators (TCT) are of importance.

4.1 The Beam Condition Monitor

Though not involved in the physics measurements, the Beam Condition Monitor (BCM) [35] is a sensor contained within the LHCb experiment. This device was designed and built at TU Dortmund, and assigned with the task of monitoring the instantaneous radiation levels close to the LHCb IP. This is done in order to protect the sensitive detector elements located at small radii from the beam line, primarily the VELO. The BCM is interfaced with the Beam Interlock System (BIS) [11] enabling it to request a beam dump if this is deemed necessary.

The device consists of 16 chemical vapor deposition (CVD) diamond sensors. 8 are located upstream of the IP and 8 downstream, forming two BCM stations. A station consists of a mounting device, cables and the sensors as shown in figure 4.2. These sensors are mounted radially symmetric around the beam pipe at a distance of 7 mm from the pipe. As the LHCb is a single armed spectrometer, the regions up- and downstream of the IP are asymmetric. The placement of the sensors and the expected radiation conditions thus differ between the two stations.

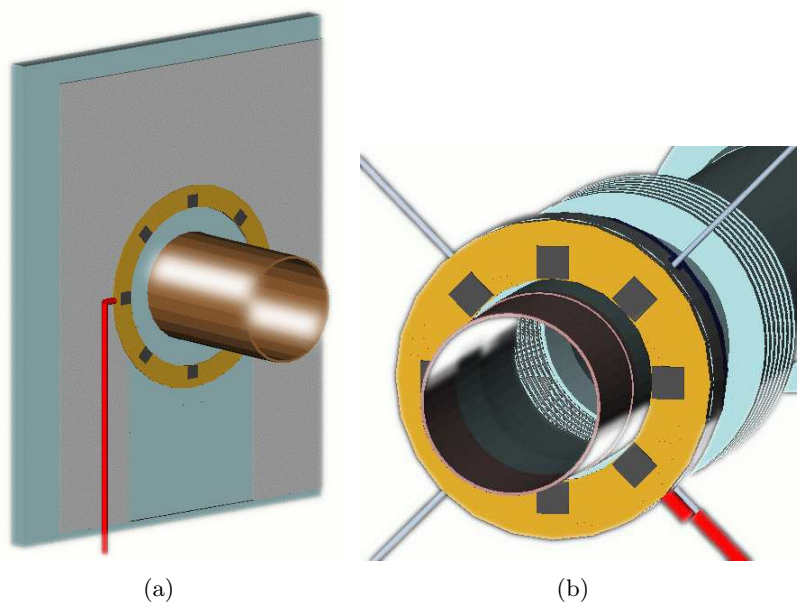


Figure 4.2: The BCM Layout. The BCM station as represented in the detector description. The upstream station, figure 4.2(a), is located at the upstream fixed pipe support. Figure 4.2(b) shows the downstream station, which is mounted on the beam pipe support inside the LHCb magnet.

The upstream station is located 2135 mm upstream of the IP, on the fixed beam pipe support by the upstream shield wall. The sensors are mounted at a radius of 54.5 mm to the center of the sensor. Downstream there is a BCM station at 2765 mm from the IP. This station is mounted on the beam pipe support inside the magnet and at a radius of 41.0 mm to the center of the sensors.

The BCM is a comparatively slow device with an integration time of 40 μ s. In other words its frequency of 25 kHz is low compared to the 40 MHz of the machine.

4.2 The MBXW Compensator Magnets

Though technically not a part of the LHCb experiment, but rather the LHC itself, the MBXW compensator magnets [36] are of importance to this thesis and must thus be introduced. These warm dipole magnets have been installed upstream and downstream of the experiment on order to compensate for the beam offset caused by the LHCb dipole magnet.

Two types of magnets exists, MBXWH and MBXWS. The MBXWH is located at -5 m from the IP and provides an opposing field to the LHCb magnet. Two MBXWS magnets are located at both sides of the IP at a distance of 21 m.

Figure 4.3 shows how the compensator magnets together with the LHCb dipole create a crossing angle at the interaction point. For an incoming beam an MBXWS bends the beam out in the horizontal plane. The MBXWH or LHCb dipole then bends the beam back in, providing a crossing angle at the IP. As the beam passes the LHCb magnet or MBXWH turns it back towards the beam line center and is finally straightened by an MBXWS. Resultingly the two beams cross at the IP with a comparatively large angle, which focuses the proton-proton interactions to a smaller z -range. The actual scheme used for the magnet setup depends on running conditions.

4.3 Apertures

There are two sets of apertures for LHCb that will be addressed in this document. Firstly there are the tertiary collimators located upstream and downstream of the experiment. These have been designed to protect the super conducting quadropoles located behind them. However, all other apertures in the vicinity and within the LHCb experiment lie in the shadow of these collimators. The second set of apertures considered are the the local apertures limitations within the experiment, disregarding the global limitations. These consist of the tightest radial restraints in the area of -22 m to +22 m from the IP.

4.3.1 Tertiary Collimators

The tertiary collimators (TCTs) consist of four separate collimators. On the upstream side, i.e. at negative z -values, the vertical collimator (TCTV.4L8.B1) is located at -73 m, while the horizontal (TCTH.4L8.B1) is at -117.5 m. The downstream vertical collimator (TCTV.1R8.B2) is 74 m from the IP followed by the horizontal (TCTH.4R8.B2) at 118.5 m.

As the names indicate the collimators clean the halo in either the vertical direction or the horizontal, thus the need for two at each side of the cavern. In both directions the vertical collimator is located closest to the experiment.

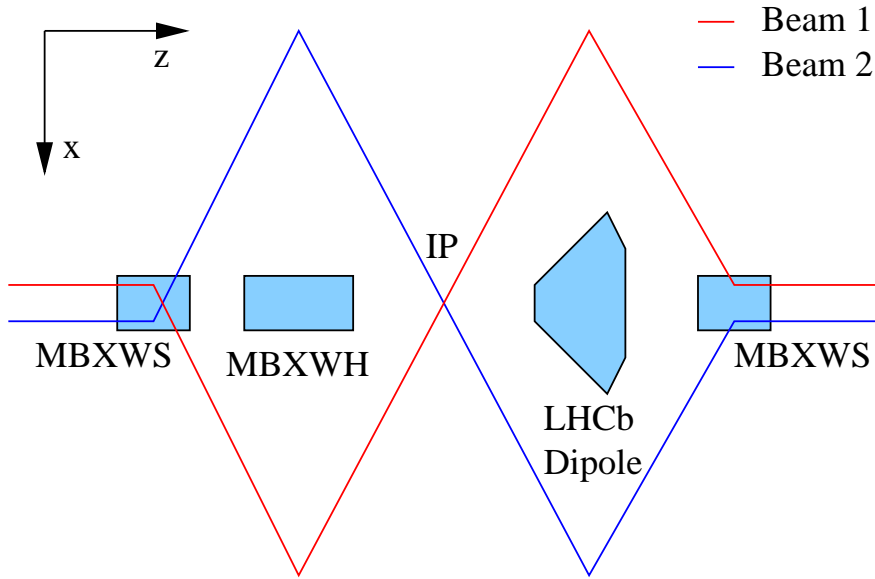


Figure 4.3: Sketch of the LHCb crossing angle in the horizontal plane. A crossing angle at the LHCb IP is created through the use of the MBXW compensator magnets in conjunction with the LHCb dipole. A half crossing angle of up to $285 \mu\text{rad}$ can be attained at the IP, corresponding to a beam separation of 3 mm at the MBXWH and LHCb Dipole. The sketch is not to scale and the various magnetic elements are symbolically indicated to show their position along the z-axis.

The collimators are supposed to only collimate the incoming beam, while leaving the exiting beam unaffected. For the horizontal collimators this is trivial as at the position of these devices there are separate pipes for beam 1 and 2. Closer to the experiment, at the location of the vertical collimators, however, the beams are in a shared pipe. The jaws of the collimator thus only occupy half the pipe as seen in figure 4.4, and are mobile in both vertical and horizontal directions. Ideally the jaws will collimate the whole width of the incoming beam while letting the outgoing pass unobstructed.

The opening of the collimator jaws depend on the machines running mode and will be indicated when deemed necessary.

4.3.2 Local Apertures

The size of the beam pipe within the area of ± 22 m of the experiment is fixed except for at the VELO chamber. As seen in section 3.5.1 this device can move and at its smallest, provide an aperture limit of 5 mm radius. When the VELO is open the smallest apertures are the pipe inside TT at 25 mm radius and inside the MBXW compensator magnets at 26 mm, as can be seen from figure 4.5.

While the upper plot in this figure shows the apertures in millimeters, the two lower plots indicate the size in width of the beam for the 450 GeV and 7 TeV scenario. As the beam is smaller close to the IP, the effective space available at this point increases.

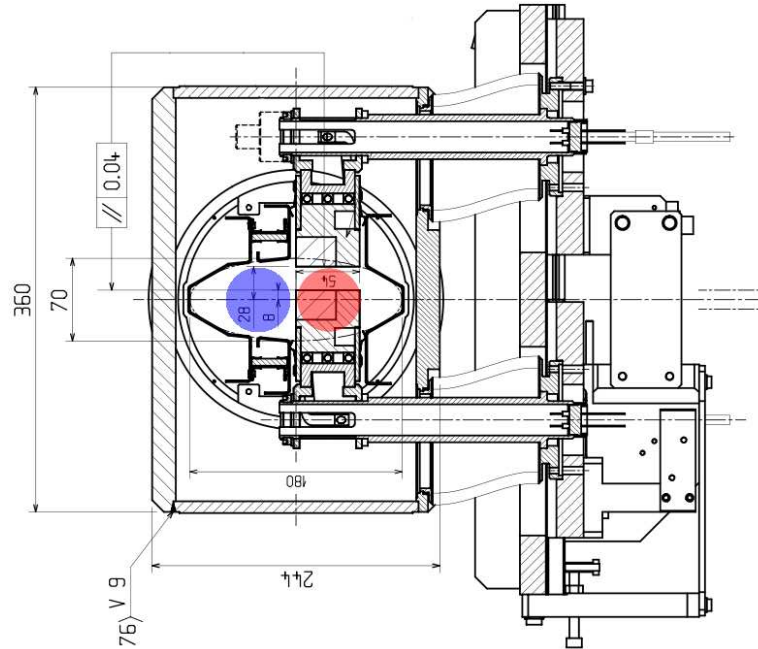


Figure 4.4: LHCb vertical TCT. The beams share a single pipe, but the collimator jaws only cover half the width. In this case the beam in the red area is collimated, while the blue is left alone. [8]

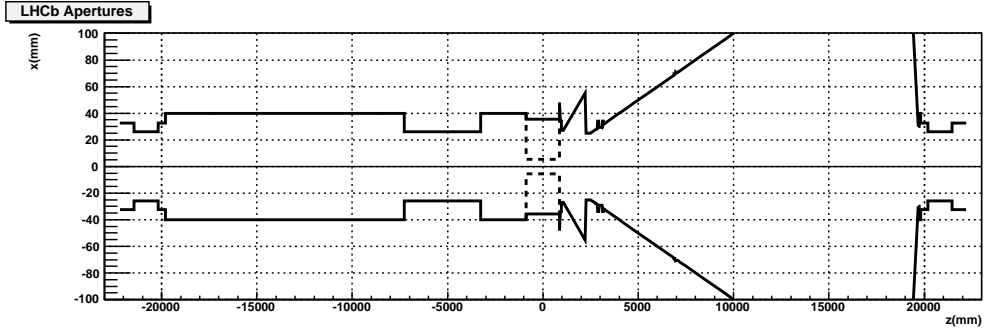
The 450 GeV and 7 TeV scenarios are shown with VELO open and closed respectively, as this would be the nominal situation.

4.4 Types of Machine Induced Background

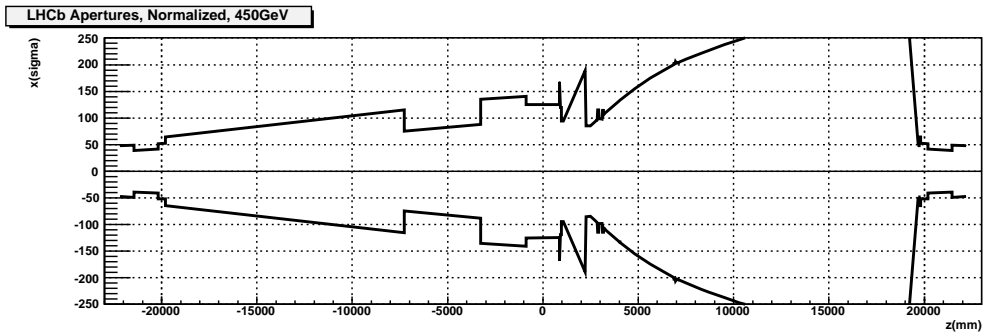
There are several types of processes causing MIB particles in the experiment. While each of them has a different cause we can define two main types, global and local.

The global sources at LHCb all have a common origin for the MIB particle shower, namely the IR8 tertiary collimators (see section 4.3.1). Various processes contribute to halo buildup (see section 2.2), which is dealt with by the beam cleaning systems at IR3 and IR7. Halo protons having survived these processes are known as tertiary halo and are eligible to impact with the TCTs potentially causing secondary particle showers to enter the LHCb cavern.

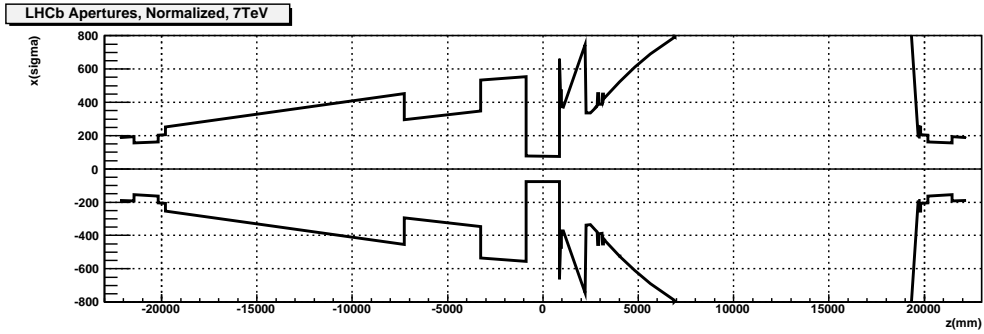
Local sources, as the name indicates, are mainly related to local effects over the



(a)



(b)



(c)

Figure 4.5: LHCb apertures. Figure 4.5(a) shows the LHCb apertures from -22 m to +22 m. The dotted line indicates the aperture when the VELO is closed. Figure 4.5(b) and 4.5(c) gives the apertures in standard deviations of the beam for 450 GeV and 7 TeV beam respectively. The 450 GeV scenario shows the VELO open, while the 7 TeV scenario is with VELO closed. All values are taken from the LHC optics web page [37]. Beam offset and crossing angles are not taken into account.

last few hundred meters of the IR8 long straight section (LSS). As this area lies in the shadow of the TCTs, the only source in this area is the interactions between the beam protons and gas residue.

Of the various conceivable sources of MIB, the following have been deemed relevant

to LHCb. The sources are marked global (G) and local (L) as appropriate, and ranked in declining expected importance to the experiment.

- Betatron cleaning inefficiency at IR7 (G)
- LHC-wide beam-gas elastic interactions (G)
- Local beam-gas interactions (L)
- Momentum cleaning inefficiency at IR3 (G)
- Elastic and diffractive interactions at ATLAS (G)

4.4.1 Betatron Cleaning Inefficiency

As described in section 2.5 the collimators at IR7 have been designed to clean off the transverse beam halo component. Though the primary and secondary collimators clean off the majority of the halo protons, the system has a non-disappearing inefficiency, meaning that a certain amount of halo protons either fail to interact with the collimator jaws or are elastically scattered. These protons accompany the beam and are eligible to be lost on the LHCb tertiary collimators as, for beam 1, this is the next limiting aperture in the direction of travel. The resulting particle shower, or quaternary halo, can enter the LHCb cavern and interfere with the experiment. Due to the fact that no arcs exist between the TCTs and the experiment, the shower is aimed at the experiment, and a wide range of particle types and energies might reach it. See figure 4.6 for a graphical representation of the collimator halo generation.

In this thesis this source is referred to as the *Betatron Source* due to its origin at the betatron cleaning system, and the fact that it scales with the related cleaning inefficiency.

4.4.2 LHC-wide Beam-Gas Elastic Interactions

When passing through the LHC vacuum chamber interactions between the beam protons and gas residue can occur. Relatively speaking the super conducting dipole magnets in the LHC arcs have the worst vacuum conditions [38] and thus it is in these sections where the majority of such beam-gas (BG) interactions occur. Inelastic interactions result in a particle shower at the location of the proton loss, while elastic and diffractive interactions results in halo protons which can be lost at any machine aperture. A fraction of these protons are lost at the IR8 TCTs resulting in a particle shower into the LHCb cavern.

In this thesis this source will be referred to as the *LHC BG Source*.

4.4.3 Local Beam-Gas Interactions

As mentioned in the previous section, inelastic interactions between the beam protons and the gas residue can directly result in a particle shower. If this occurs in the long straight section leading up to the LHCb experiment these particles are liable to enter the cavern. Losses outside this area are not taken into account as the shower particles' kinematic properties do not allow them to transverse an arc.

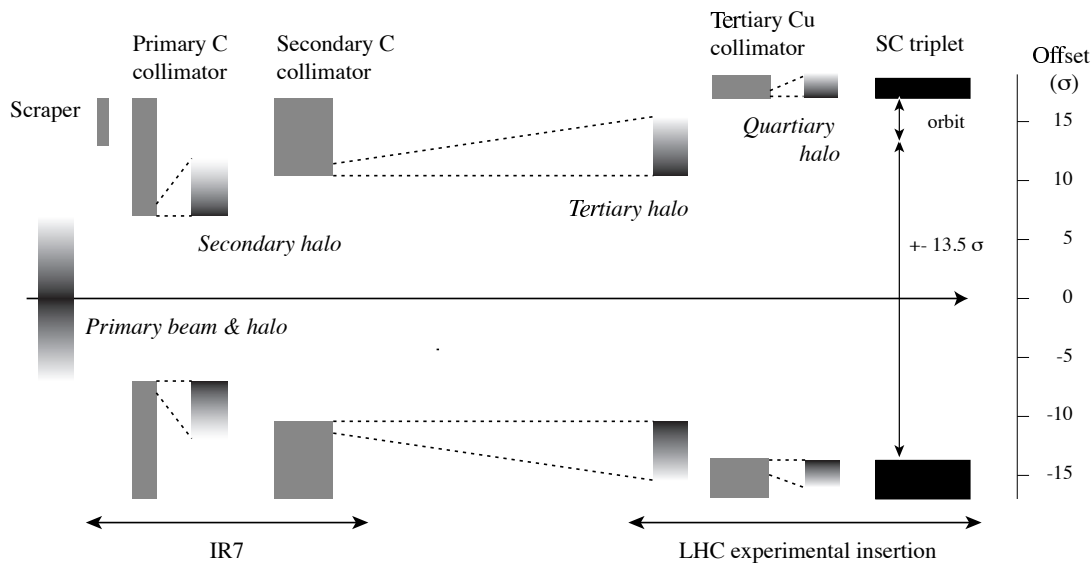


Figure 4.6: Sketch of the quartary halo generation. The collimation system of IR7 is depicted, however the system at IR3 is similar. The primary halo is cleaned through the primary, secondary and tertiary cleaning systems. The quartary halo is eligible to hit the super conducting triplet magnets and the experiments. The horizontal axis indicates the position along the beam-line while the vertical gives the distance of the various components from the beam-line center in standard deviations of the beam width. [6]

In this thesis this source will be referred to as the *LSS BG Source*.

4.4.4 Momentum Cleaning Inefficiency

As with the betatron cleaning section, inefficiencies in the momentum cleaning can result in proton losses on the IR8 TCTs. However, as this system is located at IR3, which is far away from LHCb, the rate is expected to be comparatively low. In addition IR3 is located closer to the experiment in the direction of beam 2 than beam 1, resulting in a higher rate for this beam. As LHCb is a single armed experiment in the direction of beam 1, the software expects particles to travel in this direction from the IP. Sensor hit timing is available to the software, thus Beam 2 particles can be effectively suppressed in the trigger and reconstruction. However, the increased sensor hit multiplicity can affect efficiencies and ghost rate (wrongly reconstructed tracks).

In this thesis this source will be referred to as the *Momentum Source*.

4.4.5 Elastic and Diffractive Interactions at ATLAS

Due to the fact that LHCb can tune the beam focus independently of the other experiments in order to optimize to one interaction per bunch crossing, the luminosity of LHCb is a factor 10 lower than ATLAS (IP1) at nominal design running conditions. As such, elastic and diffractive interaction at ATLAS can result in a noticeable amount

of proton losses on the IR8 TCTs for beam 2. However, this effect is only relevant at design luminosity and has to date not been estimated. It is only included here for completeness. It will not be referred to further in this thesis.

Chapter 5

Machine Induced Background Simulations

In order to attain knowledge on the proton loss rates, as well as the resulting particles shower impact on LHCb, estimates have been created and simulations have been performed.

Section 5.1 describes the procedure involved in attaining estimates of proton losses and the particle shower kinematics. Following this, in section 5.2, the implementation of an MIB generator for use in the Gauss application is shown. This tool is needed in order to simulate the MIB particles as they pass through the LHCb experiment. Finally the expected effects on the LHCb experiment from such particles is investigated in section 5.3.

5.1 Estimation Procedure

The first step of MIB analysis is attaining the rates and kinematics of the particles at the entrance of the LHCb cavern. The related estimation procedures vary depending on which source type is involved, though in general it consists of two steps: Loss rate estimation and shower transport.

5.1.1 Proton Loss Estimation

The proton loss estimation procedure consists of calculating the frequency and kinematics of the protons interacting inelastically in the LHC.

For the global losses the protons are given a perturbation consistent with a given MIB source and are transported through the LHC using a multi turn simulation containing the relevant optics and apertures of the LHC. At the point at which the proton is lost due to an inelastic interaction, its properties are saved for further processing. Figure 5.1 shows an example of a proton loss map along the LHC.

In this thesis the losses on the IR8 TCTs are of interest. The global sources used in this thesis have all been generated using the SixTrack simulation package [39]. SixTrack

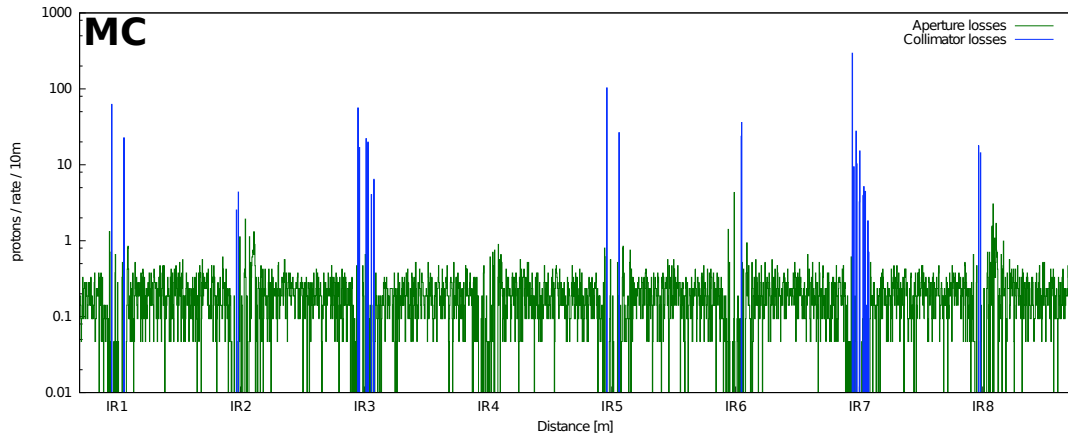


Figure 5.1: Proton loss map example, specifically losses due to elastic beam-gas interactions at 3.5 TeV for beam 1. In general the major losses occur at the collimators (blue), mainly at the cleaning sections of IR3 and IR7. The two blue lines at IR8 are the TCTs of the LHCb experiment. [38]

performs multiple turn simulations of beam protons through an aperture and magnetic field model of the LHC, recording proton loss position and kinematics. As the estimates are an LHC-wide effort, they have been generated and delivered by the LHC Collimation Group [40].

For the local LSS BG source, proton-gas interactions are simulated in the LSS according to the gas pressure profile and mixture using DPMJET [41]. A pressure profile is simply a list of gas pressures of various molecules along the beam line. The profile used for 450 GeV and 3.5 TeV is based on measurements performed by the LHC Vacuum Group and is given in H₂ or CH₄ equivalent, depending on whether the area is cold or warm, respectively. The difference in equivalents is related to the measure methods and majority gas species in the areas. For 7 TeV, a fully simulated profile has been used [42]. The specifics of this procedure is further explained in [43].

5.1.2 Particle Shower Transport

The particle shower transport consists of estimating the development of the particle shower and tracking the individual particles resulting from the primary proton interaction to the entrance of the LHCb cavern. In order to do so a model containing the apertures and magnetic fields of the last couple of hundred of meters of the tunnel leading up to the experiment has been implemented [44]. For the transport the FLUKA [45] application has been used.

The output from this procedure gives particle properties and fluxes at the entrance to the LHCb cavern. Two standard “interface planes” have been decided upon. For beam 1, the particles are scored at $z = -2.1$ m, while for beam 2 this plane is at $z = 19.9$ m. The resulting files are referred to as the MIB estimates throughout this thesis and are used as input for the LHCb specific software. Details concerning the

production of the estimate files can be found in [46].

5.1.3 Source Rescaling

Due to the diversity of possible running scenarios as well as expected and unexpected background conditions it is useful to be able to scale the MIB estimates accordingly.

The betatron and momentum source scale linearly with the beam current and the cleaning rate, while changes in beam energy and, to a lesser degree, beta function require new estimates to be performed. In general changes to optics and kinematic variables can change the background in nontrivial ways.

The beam-gas interactions, both in the LSS and LHC-wide depend on the gas profile, as higher densities increase the rate. However, by folding in the difference in the old and the new gas profile it is possible to rescale the sources as the information on the initial proton loss is still present in the MIB estimate files (See section 5.2.3). While the LSS BG source depends mainly on beam energy, current and gas profile, the LHC BG source, like the other global sources, also depends on the machine optics.

Table 5.1 shows the trivial re-scalability of the various MIB sources. Changes in other beam parameters normally require new estimates to be performed. When considering the impact of MIB in this document, the scaling used will be indicated where relevant.

Table 5.1: MIB source re-scalability. All sources can be scaled by the beam current. The beam-gas sources are affected by the vacuum conditions, while the collimator sources depend on the inefficiency of the related collimation system.

Source	Beam Cur.	Gas prof.	Col. ineff.
Betatron	X		X
LHC BG	X	X	
LSS BG	X	X	
Momentum	X		X

5.2 The Machine Induced Background Generator

In order to simulate MIB particle sources arriving at the LHCb cavern a special particle generation package called the Machine Induced Background Generator (LbMIB) has been developed. This package contains tools that can read files describing, amongst others, kinematics and flux of such external particles, and generate them in the LHCb simulation suite.

Two different tools have been created for LbMIB. Initially the tool “CollimatorSource” was written to generate background particles based on the early existing estimates. The requirements of the tool was as follows:

- Compatability with the existing LHCb simulation software
- Ability to Read MIB estimates and reproduce the therein contained particles in the LHCb simulation
- Control of rate, direction and point of production through options
- Reasonable computing resources consumption

A more complex estimate file format was defined at a later point, taking amongst others particle correlations into account. The second tool, dubbed the “TimeCorrSource”, was designed to generate particles using this estimate type. The additional demands for this tool were:

- Event based generation, re-producing the full MIB shower in the simulation
- Particle timing. Give particles their “true” timing information based on information from the estimate file

The following sections describe the MIB estimate file formats used and how the events and particles are re-generated in the LHCb simulations using the TimeCorrSource tool. The workings of the older CollimatorSource tool will be mentioned where relevant.

5.2.1 The MIB Estimate Input Format

The original MIB estimates were made available to the collaboration in the form of flat text files containing the elements displayed in table 5.2. Each line contains all elements and represents a single MIB particle. The CollimatorSource tool was created specifically to be able to import, parse and generate particles from already existing background estimate files.

Table 5.2: CollimatorSource File Format. Each particle is represented through a line containing all the variables.

Element	Description
PartPdgId	PDG particle ID number
PartW ₀	Particle “weight” (likelihood)
PartEk	Particle kinetic energy (GeV)
PartX	Particle x coordinate at interface plane (cm)
PartY	Particle y coordinate at interface plane (cm)
PartDx	Particle x direction cosine at interface plane
PartDy	Particle y direction cosine at interface plane

Most of these variables are self explanatory, however the particle weight needs to be given a bit of attention. This variable is a measure of the relative generation probability a given particle has with respect to the whole file. The sum of weights of all particles in

a file gives the total particle flux of the source represented by the file. If the source file has been scaled to represent for example one second at a certain machine configuration, then the sum of weights gives the flux in particles per second for those settings. This number is also used in order to randomly decide how many background particles are to be generated in a given simulation event in such a way that the overall particle flux will be correct in the simulation.

Furthermore the weight is used as a probability for the individual particles in the file. If one particle should be generated from the file, the probability that a given particle is generated is equal to P_p , where P_p is given from equation 5.1. The summation goes over all the N_p particles in the file.

$$P_p = \frac{\text{PartW}_0}{\sum_1^{N_p} (\text{PartW}_0)} \quad (5.1)$$

There are certain limitations to this particle input format. In particular no time of arrival information and no correlations between the various particles exist. This would indicate whether the individual particles arrive as a shower or independently one by one. Both these limitations can have an impact on the simulations of interference in trigger and reconstruction caused by MIB particles.

To correct this problem it was decided that a new source file format needed to be defined. The elements in this format are described in table 5.3. As one can see when comparing the two file formats, the second format has a few additional entries. The main change is the addition of the proton loss section. This gives information about the primary proton loss resulting in the given particle. Multiple particles arriving in the same shower would thus have the same LossID number indicating that they belong together. Secondly the variable PartDt indicates the particles time of arrival at the interface plane with respect to the time at which the center of the bunch would cross this point, i.e. the time offset.

In the new format the variable LossW replaces PartW as randomization parameter. The probability that a certain MIB event is selected from the file is equal to P_e , where P_e is described by equation 5.2. The full file contains N events.

$$P_e = \frac{\text{LossW}}{\sum_1^N (\text{LossW})} \quad (5.2)$$

If a given event is selected, then all particles belonging to this event are viable to be generated. In the new format the element PartW has two possible uses. If it has a value under unity it indicates the probability of the particle being generated. If it is an integer of unity or higher, it indicates how many times the same particle should be created. Though not intended by the definition of the parameter, non-integers above unity are allowed. The integer part indicates the minimum amount of particles to generate in a given event, while fractions are randomized. I.e. the value 2.4 indicates two particles and a 40% probability of a third.

Another feature of the new file format is the addition of variables to facilitate rescaling of the source. For example beam-gas sources would need to be rescaled in the

Table 5.3: The new source file format. Each particle is represented through a line containing all the variables.

Element	Description
LossID	Proton loss identifier
LossT0	Time offset of proton loss w.r.t. the bunch center (ns)
LossZ	Proton loss z coordinate (mm)
LossA	Type of atom involved in proton loss
LossW	Proton loss “weight” (likelihood)
PartPdgId	PDG particle ID number
PartX	Particle x coordinate at interface plane (mm)
PartY	Particle y coordinate at interface plane (mm)
PartZ	Particle z coordinate origin at creation (mm)
PartDx	Particle x direction cosine at interface plane
PartDy	Particle y direction cosine at interface plane
PartEk	Particle kinetic energy (GeV)
PartDt	LHC clock offset for particle arrival at interface plane (ns)
PartW	Particle “weight” (likelihood)

case of changes in the gas profile. This rescaling depends on the location of the proton loss (LossZ) and the atom involved in the interaction (LossA). As these variables are elements of the file format, such rescaling can be directly applied.

The existence of a new format does not make the old results obsolete. Translation between the two is possible. Events are created containing a single particle from the old format, and all missing event information is given dummy values. The weights are set such that the generation probability of the event is equal to what it was for the original particle.

5.2.2 The TimeCorrSource Tool

The TimeCorrSource tool was created specifically to be able to import, parse and generate events and particles from the background estimate files. These files usually contain somewhere between 10^4 and 10^7 particles, but no strict limits exist. Due to the potentially large size of the files it is impossible to contain them completely in memory. However the computational overhead involved in sorting, searching, parsing and selecting particles from a text file is large. In order to improve this, the data is translated into a binary format. This assures rapid particle information access and avoids repeated text-parsing of the variables, while at the same time limiting the memory usage.

In TimeCorrSource the binary format used is ROOT [47]. Each file contains one tree for the particles and one for the proton losses. Proton losses are also referred to as MIB events in the simulations. In the context of the MIB estimates, the ROOT tree is simply a flat structure containing all particle or event related variables. Each entry in the tree represents one particle or event, respectively. The user can thus

consider the particles independently or as a part of a MIB event, depending on his or her requirements.

The event tree contains information as to which particles belong to a given event. In addition to assure maintainability of the code by using a standardized format, this enables the user to analyze the MIB files themselves by simply using ROOT. A script has been written which is able to convert both the old and the new particle file format into ROOT trees.

The ROOT format contains the previously discussed particle information as well as a few other elements facilitating rapid random particle selection. Because of the non-uniform weight and thus probability of the various events, the randomization procedure is more complicated than just selecting a random entry. For event n the weight of all events from position 1 to n is summarized and stored as a additional data element, s_n , in the ROOT file. This variable is calculated as shown in equation 5.3.

$$s_n = \sum_1^n (\text{LossW}) \quad (5.3)$$

When an event is generated, a uniformly distributed random number, r , in the range $[0, \sum_1^N (\text{LossW})]$ is chosen. The event sought is the event i where the condition $s_{i-1} < r \leq s_i$ is true. This event is located using a search algorithm.

Though it is possible to search for the random event directly in the file, this requires multiple comparatively slow file access commands to be performed. In order to improve on this the TimeCorrSource tool performs a pre-selection using an envelope method. The sum of weights variable s is saved in memory for every J th event. An interpolation search is then performed on this event subset in order to find out which of the envelopes contain the requested event. Specifically the envelope j where $s_{J \times (j-1)} < r \leq s_{J \times j}$ is located.

A second search can then be performed directly on the file where the candidates are limited to the J events contained within the envelope j . For performance reasons the envelope size should be chosen as small as possible (it could even be one), while keeping the memory usage at a reasonable level.

When the event has been located the related particles are viable to be generated. As explained in the previous section, a below unity PartW parameters determines the probability of generation, while integer values result in an exact number of particles.

When a particle has been selected it is generated with the appropriate kinematic properties and handed over to the LHCb simulation package. Though the MIB files are given at a certain interface plane defined by a distance from the IP on the z -axis, the plane of generation can be chosen at a different point. In this case the particles are projected linearly from the interface plane to the generation plane, ignoring any material and/or magnetic fields.

The particle variable PartDt defines the time offset of the particle with respect to the bunch centroid as it passes the interface plane. The timing used in Gauss defines $t = 0$ at the point where the bunch passes $z = 0$. Using the beam energy one can calculate the time at which the bunch passed the generation plane. This is shown in

equation 5.4, where the time t_{0_p} at which the bunch protons passed the interface plane is given as a function of the direction $d \in \{-1, 1\}$ of the beam, the distance z_0 to the interface plane, as well as the kinetic energy E_{k_p} and mass m_p of the protons. An ideal reference proton p is used for the purpose of the calculations. For beam 1 the direction is positive and the interface plane at a negative z -position, thus the time at which the protons pass the interface plane is negative, as expected.

$$t_{0_p} = d \times z_0 \times \frac{1}{c} \times \sqrt{1 + \frac{1}{\left(\frac{E_{k_p}}{m_p} + 1\right)^2} - 1} \quad (5.4)$$

If the particle q has a time offset, it traverses the interface plane at the point in time defined by equation 5.5. As the MIB particle typically lags behind the proton bunch, the value of PartDt is positive.

$$t_{0_q} = \text{PartDt} + t_{0_p} \quad (5.5)$$

If the generation plane g is not the same as the interface plane, the kinetic properties of the particle is also taken into account in order to project it correctly as shown in equation 5.6. The time at which the particle is generated at the generation plane is t_g . The variable dz is the cosine of the angle between the direction of travel and the z -axis while Δz is distance between the interface plane and the generation plane. dz is needed as we consider a plane perpendicular to z with a particle that moves at an angle to the z -axis. Particles traveling at a steep angle require longer time than those parallel to the z -axis.

$$t_g = t_{0_q} + \Delta z \times \frac{1}{c \times dz} \times \sqrt{1 + \frac{1}{\left(\frac{E_{k_q}}{m_q} + 1\right)^2} - 1} \quad (5.6)$$

Additionally, a user definable option allows a global time offset to the particles. This can for example be used to simulate the particles from a previous bunch crossing in the current event. Figure 5.2 visualizes the various timing steps mentioned in these calculations.

Both the timing and correlation information are required for various studies, in particular those related to trigger and reconstruction where number of tracks and their timing can influence the results to a great deal.

In order to simplify the setup of this generator, header information is added to the ROOT file containing the standard parameters for the given source. This information includes beam direction, interface plane, scaling and source description.

This tool can be used to simulate the machine induced background alone or in conjunction with other generators, for example the normal beam-beam event generation.

5.2.3 Gas Profile Rescaling Tool

As mentioned, the gas profile in the beam line can change as a result of changes in running conditions and it must be possible to rescale the relevant sources accordingly.

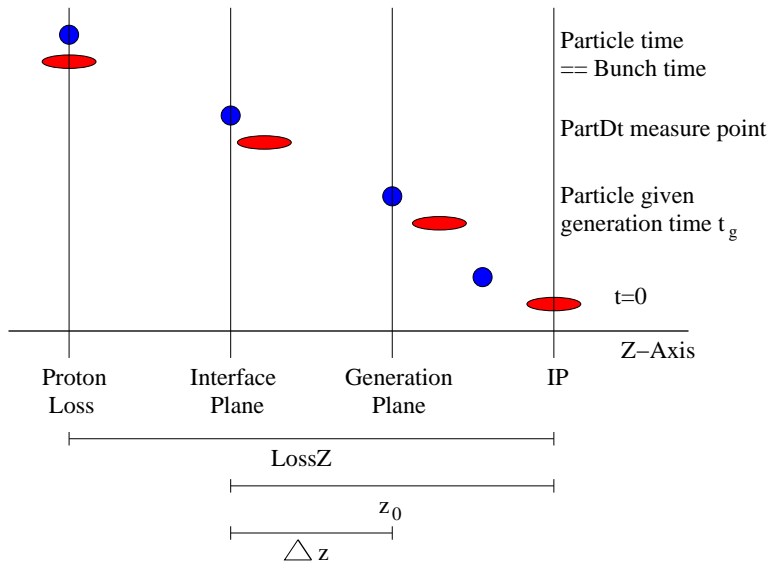


Figure 5.2: MIB particle timing. Red oval represents the proton bunch, while the blue circle is a MIB particle. LHCb timing has $t = 0$ as the bunch passes $z = 0$. The MIB particles are given with a time offset to the bunch at the interface plane. The particles must be generated at the generation plane with a timing appropriate according to the LHCb timing in order to have the correct impact on tracking and reconstruction.

Though an overall constant increase can occur, a more likely scenario entails local changes to the pressure and / or gas species mixture. The source can thus not be trivially scaled by a linear factor but rather by a list of entries, each giving the change of pressure of a certain gas species in a certain section of the beam line. Gas profile files are used to represent the vacuum conditions. These files list the pressure of various gas species at intervals along the beam line.

The rescaling of a MIB beam-gas source can be performed using a tool written for this specific purpose. The source file, along with the gas profile used when it was created, are passed to the tool together with a new profile to which the source should be scaled. For each atomic species of the gas the new profile is divided by the old, resulting in a scaling factor profile.

Each MIB event in the source file contains information on the origin of the proton loss, giving both location ($LossZ$) and atomic species ($LossA$) involved in the interaction. The event changes its probability of generation ($LossW$) according to the pressure change factor for the relevant gas species and location. The rescaled event is saved in a output source file, and has a distribution representative of the new gas profile. The reliability of this tool depends on adequate statistics for each atomic species at each position.

5.2.4 Current Status of LbMIB

The LbMIB package is currently a standard component of the Gauss application, having the stability and reproducibility needed for a particle generator. As all estimate files are currently produced using the new file format, mainly the TimeCorrSource tool is used in LHCb simulations.

One major issue for simulation data production is the computing time required. The event and particle selection procedure of the LbMIB algorithms is rather slow, as an event and particle search must be conducted. For a binary search algorithm the expected time dependence on the number of events in the files is logarithmic. The size of the estimate files are limited by the fact that they have to be distributed to every LHCb related repository. Tests using the currently available estimate files of reasonable size show that MIB generation can take up to 10 times longer than physics events. However, the simulation step of Gauss is far slower than the generation and depends primarily on the particle multiplicity. Due to the, on average, low multiplicity of the MIB events, the full simulation time for such events is about half of that of a physics event.

These numbers are rough, but show that MIB generation time is expected to be of the same order as a physics event, thus not causing problems during production. As such, the LbMIB will be included in the generation of the official simulation production of 2011.

5.3 Effect of Machine Induced Background

For the machine induced background three main scenarios have been investigated. These are injection at 450 GeV, intermediate energy run at 3.5 TeV and nominal design at 7 TeV. Initially the effort were focused on the 7 TeV scenario as all the MIB estimates existing was created at this energy level, however due to the decision to have an extended physics run at 3.5 TeV the efforts have shifted to this energy level. For 450 GeV only a limited set of MIB sources are available, however they have been useful for investigations into the first data produced at the LHC startup in 2009. The sources currently available are listed in table 5.4.

For the 7 TeV scenario loss rates at the tertiary collimator for momentum cleaning inefficiency and LHC-wide proton-gas interactions are available. However, the kinematics of the losses are only available for betatron cleaning. For the time being the same distribution is thus used for all three source. This assumes that all global sources only vary in rate, and not in characteristics. This is a simplification which has not yet proven to be right or wrong as no grounds for comparison exist. In practical terms a rescaled version of the betatron cleaning source is used to represent the momentum and LHC BG sources.

For the losses on TCTV several samples have been generated due to the particular design of the collimator (see section 4.3.1). Both beams are contained in one pipe, but collimation only occurs on the incoming beam.

The beams are pointed to the IP of the experiment, thus at the TCTs they are

supposed to have a certain horizontal offset, or geometric orbit. As the TCTV is not horizontally uniform (as seen in figure 4.4) a variation of this orbit can change the background conditions. Such a variation occurs when for example the beam crossing angle is changed. The nominal geometric orbit is referred to as *full*, while *half* and *quarter* means that the horizontal offset of the beam is half or quarter of the nominal, respectively (i.e. closer to the beam line center). Furthermore, *total* orbit means a full geometric orbit, with an additional beam orbit. The beam orbit is a fluctuation of the beam around the geometric (reference) orbit. Throughout this document the *full* version will be used unless otherwise indicated.

Furthermore, the TCT losses use either a fully vertical or fully horizontal halo distribution. Resultingly, the data represents the extremes as the halo would normally be distributed in both directions.

Table 5.4: Currently available MIB sources.

Energy	Source	Beam	TCT	Halo	Orbit	Nickname
450 GeV	LSS BG	1	N/A	N/A	N/A	B1BGLSS
	LSS BG	2	N/A	N/A	N/A	B2BGLSS
3.5 TeV	LSS BG	1	N/A	N/A	N/A	B1BGLSS
	Betatron	1	TCTH	Hor	N/A	B1TCTHH
7 TeV	LSS BG	1	N/A	N/A	N/A	B1BGLSS
	Betatron	1	TCTV	Vert	Quarter	B1TCTVVQ
	Betatron	1	TCTV	Vert	Half	B1TCTVVH
	Betatron	1	TCTV	Vert	Full	B1TCTVVF
	Betatron	1	TCTV	Vert	Total	B1TCTVVT
	Betatron	1	TCTH	Vert	N/A	B1TCTHV
	Betatron	1	TCTH	Hor	N/A	B1TCTHH
	Betatron	2	TCTV	Vert	Quarter	B2TCTVVQ
	Betatron	2	TCTV	Vert	Half	B2TCTVVH
	Betatron	2	TCTV	Vert	Full	B2TCTVVF
	Betatron	2	TCTV	Vert	Total	B2TCTVVT
	Betatron	2	TCTH	Hor	N/A	B2TCTHH

5.3.1 Properties of the MIB Estimates

There are several properties of the MIB estimates that can be of interest to the various detectors and physics programs. In this section a few features will be highlighted, in particular those who will have an impact on further analysis shown in this thesis.

Spatial Distribution

The spatial distribution of MIB particles is expected to vary depending on whether the source is global or local. For the global sources, the initial proton loss occurs at the

location of the tertiary collimator jaws. Resultingly, the particle shower is initiated at a certain radial distance from the beam line center. Conversely, the local beam gas is most likely to occur at the position of highest proton flux, namely at the beam center. Furthermore, the interaction can occur at any point inside the beam line.

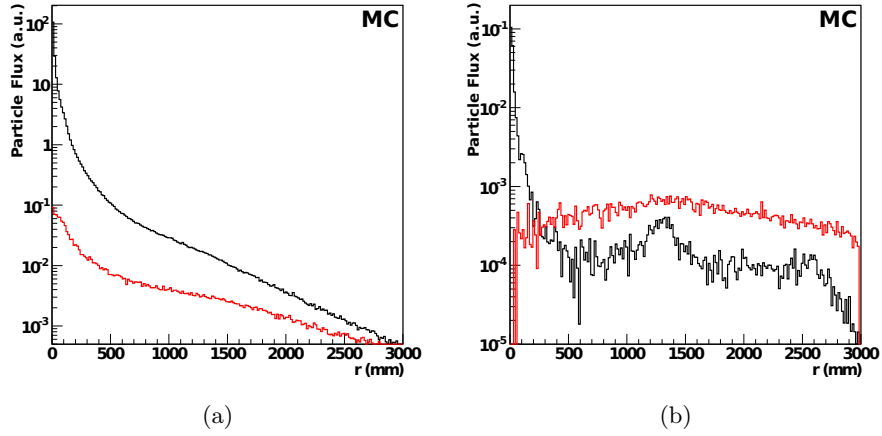


Figure 5.3: MIB radial distribution at the interface plane. Figure 5.3(a) depicts the charged hadron (black) and muon (red) radial density for the LSS BG source at 3.5 TeV, beam 1. Figure 5.3(b) is the equivalent for the betatron source. Due to tunnel shielding the charged hadron distribution is more peaked than the muonic. The vertical axis is in arbitrary units.

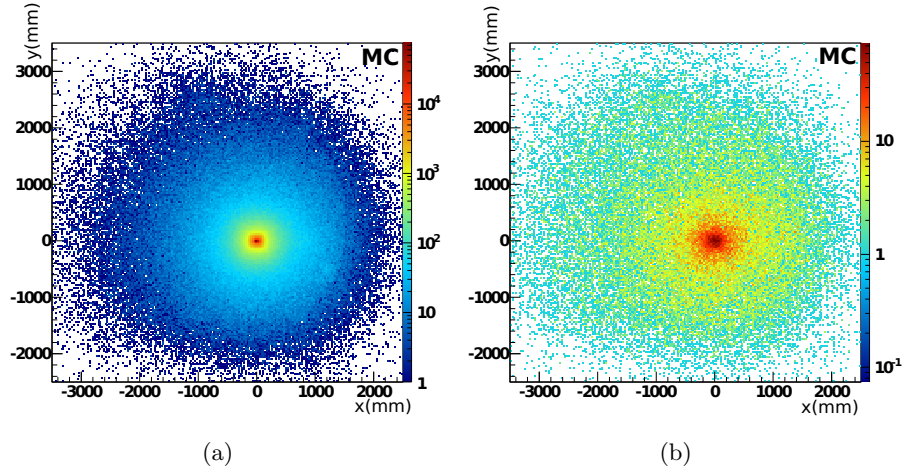


Figure 5.4: MIB transverse distribution at the interface plane for the 3.5 TeV LSS BG source. Figure 5.4(a) shows charged hadrons while 5.4(b) shows muons. The outer shape of the distributions is indicative of the LHC tunnel (-3 m to +2 m in the horizontal plane and -2 m to +3 m in the vertical). The vertical axis is in arbitrary units.

From the radial particle density distribution at the interface plane of figure 5.3 one

can draw two conclusions. Firstly, the local source is much more centrally pointed than the global and secondly the muonic background is in general flatter than the hadronic. The main reason for this is the existence of shielding in the tunnel, consisting of concrete and iron walls. The majority of the hadronic background is blocked, except at low radii where no shielding is present. The high penetration power of the muons means that they are affected to a lesser degree. These same effects can be seen in the xy distribution of figure 5.4.

The distinctive kinematic differences of the source types requires them to be treated independently when investigating their effect on the experiment. The splitting in muonic and hadronic background is of a practical nature, as these are typically recorded by different detector systems and thus interact with the machine in different ways.

Particle Multiplicity

The effect of MIB on trigger and particle reconstruction is affected by the particle multiplicity in the MIB event. As the new estimate file format contains the particle correlations and thus gives information on the complete particle shower, the simulations can generate it as such. Figure 5.5 shows the particle multiplicity for beam-gas in the long straight section and proton losses on the tertiary collimator due to betatron cleaning inefficiency for 3.5 TeV, beam 1.

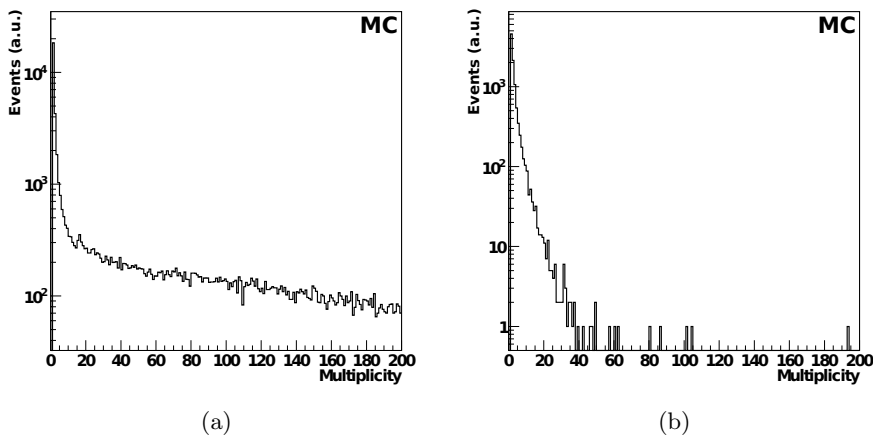


Figure 5.5: MIB particle multiplicity per event. Figure 5.5(a) depicts the particle multiplicity of the MIB events contained in the LSS BG sample at 3.5 TeV. Figure 5.5(b) is the equivalent for the betatron source. The vertical axis is in arbitrary units.

As can be seen from these plots, even though the majority of events have a low multiplicity, there exist a fraction of events with large to very large multiplicity. The size of the MIB shower is relevant when considering the impact it has on the trigger system as it takes multiplicity into account.

Particle Time of Arrival

As the MIB particles are generated at a distance from the interaction point, they have a tendency to slightly lag behind the proton bunch. Figure 5.6 shows the time offset of the MIB particles at the interface plane for beam-gas in the LSS and TCT impacts due to betatron inefficiency for beam 1 at 3.5 TeV.

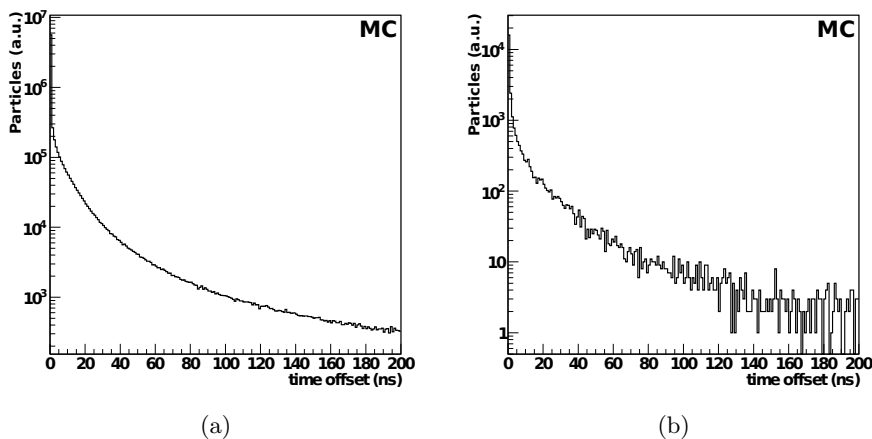


Figure 5.6: MIB particle time offset. Figure 5.6(a) depicts the time offset of the particles contained in the 3.5 TeV LSS BG source file. Figure 5.6(b) is the equivalent for the betatron source. One can see that MIB particles can be delayed several bunch crossings. LHC machine frequency is 40 MHz thus bunches can be interspaced by 25 ns. The vertical axis is in arbitrary units.

Though the distribution peaks at low time offset, meaning that the particles follows the bunch tightly, there is a long tail of “late” particles that arrive several bunch crossings of 25 ns later. For a highly filled machine this is important as particles from a preceding event will spill over in the next. Though currently not needed, future simulations will include MIB from previous bunches in order to get a complete picture of the background situation. Figure 5.7 shows the time of arrival of particles at the Inner Tracker in the case of MIB from both beams and proton-proton events in each 25 ns frame.

Rates of Global Losses

To calculate the proton loss rates, a beam lifetime, τ , is set for each of the various sources. This lifetime assumes beam population decay due only to the given source. In order to ascertain the proton loss rate related to the lifetimes one can assume an exponential decay of the proton population $N(t) = N_0 e^{-\frac{t}{\tau}}$. The maximal decay rate is given at time zero through the equation 5.7. This value is used to represent the proton loss rate in the MIB studies.

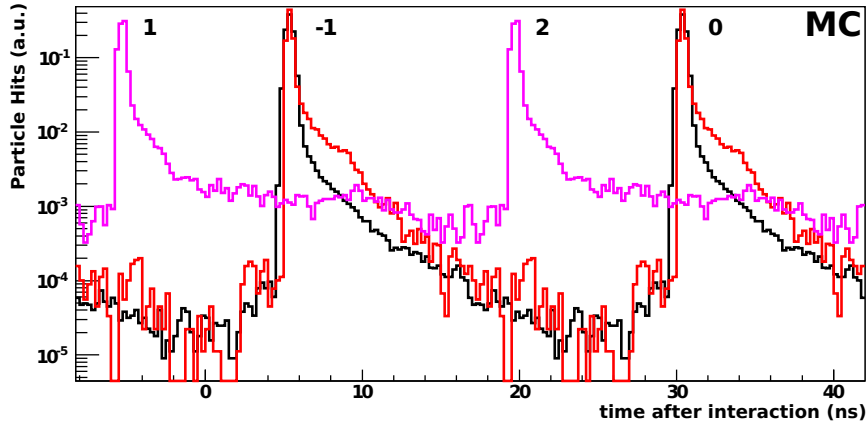


Figure 5.7: Multi-frame particle timing at IT. The figure shows the time of arrival at IT for particles arriving from proton-proton interactions at the IP and MIB from both beams. The peaks are numbered in relation to the proton-proton interaction occurring at $t = 0$. Beam 1 MIB (red) is on-time with proton-proton interactions (black), while beam 2 MIB (magenta) has a completely different time structure. The indices of the peaks indicate the related bunch numbers, where bunch number zero of both beams crossed the IP at time zero. Negative numbers indicate previous bunches while positive arrive after. The vertical axis is in arbitrary units.

$$\frac{dN}{dt} \Big|_{(t=0)} = \frac{N_0}{\tau} \quad (5.7)$$

Table 5.5 lists the lifetimes for the relevant sources at 7 TeV. In the case of the cleaning lifetimes, these represents the expected value, while the beam-gas source is worst case as defined in the vacuum specifications. A low value of τ results in a high proton loss rate, and thus potentially high MIB rate.

Table 5.5: Beam life-times. For betatron and momentum cleaning the value represents an expected lifetime, while for beam-gas it is the lowest (worst) value still within the design specifications.

Source	Life-Time
Betatron Cleaning	30 h
Momentum Cleaning	195 h
LHC Beam-Gas	100 h

As seen in section 5.1 estimates are performed for the various scenarios giving a proton loss rate at the various apertures. The fraction of protons lost ending up on the IR8 collimators can be seen in table 5.6. For the 450 GeV scenario these sources have not been estimated because the TCTs were in a relaxed state (far out), and thus

attained a very limited rate. For the 3.5 TeV scenario only hits on the TCTH exists as the estimates given by the collimation group at this energy level show a negligible rate on the TCTV. The actual loss rate is attained by scaling with the relevant life time and beam population. For the betatron cleaning inefficiency the losses have been calculated for a purely vertical or horizontal halo.

Table 5.6: Fraction of the overall proton losses impacting on the IR8 TCTs from various MIB sources. For betatron cleaning VH and HH indicates completely vertical or horizontal halo, respectively.

Energy	Scenario	Beam 1	Beam 2
7 TeV	Betatron; TCTV (VH)	9.2×10^{-4}	6.4×10^{-6}
7 TeV	Betatron; TCTV (HH)	2.6×10^{-6}	Not Estimated
7 TeV	Betatron; TCTH (VH)	3.6×10^{-5}	Not Estimated
7 TeV	Betatron; TCTH (HH)	1.8×10^{-4}	3.1×10^{-5}
7 TeV	Momentum; TCTV	1.1×10^{-4}	2.2×10^{-4}
7 TeV	Momentum; TCTH	8.2×10^{-5}	5.4×10^{-3}
7 TeV	Elastic Beam-Gas; TCTV	5.7×10^{-3}	9.5×10^{-3}
7 TeV	Elastic Beam-Gas; TCTH	7.8×10^{-3}	8.7×10^{-3}
3.5 TeV	Betatron; TCTH (HH)	4.8×10^{-4}	Not Estimated

Protons lost on the TCTs can cause a secondary particle shower towards the experiment. Some of these showers are completely absorbed before reaching the cavern, while others traverse the experiment. Table 5.7 shows the rate of particles at LHCb per lost proton on the TCTs for various sources. Particle shower transport has only been performed for the betatron cleaning inefficiency source. As such the values shown in the table are related to this source. All information concerning MIB shower rates on the LHCb experiment assume that the properties of the shower is similar for all global sources. As only the betatron cleaning estimate is available, this is an assumption that is yet to be proven right or wrong. However, for determining the order or magnitude of MIB, it should suffice.

Table 5.7: MIB particles per lost proton on the TCTs due to Betatron cleaning inefficiency. VH and HH indicate whether purely vertical or horizontal halo has been used. Only charged hadrons and muons are listed.

Beam	Energy	Source	Ch. Had.	Muon
B1	7 TeV	TCTV (VH)	0.06	0.08
B1	7 TeV	TCTH (VH)	0.12	0.16
B1	7 TeV	TCTH (HH)	0.13	0.14
B1	3.5 TeV	TCTH (HH)	0.02	0.07
B2	7 TeV	TCTV (VH)	0.44	0.25
B2	7 TeV	TCTH (HH)	0.02	0.06

Combining the information in table 5.5, 5.6 and 5.7 gives an expected MIB particle flux at the entrance of the experiment. Table 5.8 shows the expected rates for the sources estimated for the 7 TeV full machine scenario. In relation to this, a word of caution is needed. Rates are given assuming either purely vertical or horizontal halo.

Table 5.8: MIB flux from global losses for the 7 TeV scenario. The rates of charged hadrons (CH) and muons are given for both beams due to proton losses on the vertical (V) or horizontal (H) collimators. Either a purely vertical (V) or horizontal (H) halo is used. Combinations not shown have not been made available due to low rates. Three types of sources are shown namely betatron cleaning (Beta. Cl.), momentum cleaning (Mom. Cl.) and elastic beam-gas interactions (El. BG).

Beam	Halo	TCT	Type	Beta. Cl.	Mom. Cl.	El. BG	Sum
B1	V	V	CH.	1.65×10^5	3.04×10^3	3.07×10^5	4.75×10^5
B1	V	V	Muon	2.20×10^5	4.05×10^3	4.09×10^5	6.33×10^5
B1	V	H	CH.	1.29×10^4	4.53×10^3	8.40×10^5	8.57×10^5
B1	V	H	Muon	1.72×10^4	6.04×10^3	1.12×10^6	1.14×10^6
B1	H	H	CH.	7.00×10^4	4.90×10^3	9.10×10^5	9.85×10^5
B1	H	H	Muon	7.53×10^4	5.28×10^3	9.80×10^5	1.06×10^6
B2	V	V	CH.	8.42×10^3	4.45×10^4	3.75×10^6	3.80×10^6
B2	V	V	Muon	4.78×10^3	2.53×10^4	2.13×10^6	2.16×10^6
B2	H	H	CH.	1.85×10^3	4.97×10^4	1.56×10^5	2.08×10^5
B2	H	H	Muon	5.56×10^3	1.49×10^5	4.68×10^5	6.23×10^5

Comparing these results to the average proton-proton interaction rate at the IP of about 31.6 MHz it is clear that the expected MIB flux of a few MHz should not cause radiation issues, however, it might still interfere with trigger and reconstruction.

For the 3.5 TeV scenario there are large variations in run scenarios, regarding number of bunches, bunch population and cleaning inefficiencies. Assuming 30 hours betatron cleaning beam lifetime the charged hadron rate is 10.2 Hz per 1.15×10^{11} protons bunch, while the muon rate is 35.8 Hz.

Rates of Local Losses

The local losses, i.e. beam-gas in the LSS, originate mainly from the vicinity of the beam centroid due to the fact that the proton flux and thus the interaction rate is at its highest there. Rather than originating at the TCTs the MIB showers from local beam-gas interactions can develop from any point in the long straight section as seen from figure 5.8. As a result of these two characteristics the shower properties are somewhat different from the TCT losses.

As can be seen from table 5.9 the average MIB particle multiplicity per lost proton is higher than in the global sources (table 5.7). This is mainly due to the fact that the local source showers can develop from a position closer to the experiment, effectively bypassing the shielding. Due to the fact that the estimates for the three energy level were given at different times, the length of the LSS over which the estimates were

performed vary. As a result the flux per lost proton is not directly comparable between the energy levels. Table 5.10 shows the shower particle flux for a beam of 20×10^9 protons.

Table 5.9: MIB particles per lost proton for LSS BG which arrive at the interface plane.

Energy	Ch. Had.	Muon
7 TeV	2.82	0.33
3.5 TeV	8.59	0.62
450 GeV	2.50	0.18

Table 5.10: MIB particles flux in particles per second at the interface plane for LSS BG. A beam of 20×10^9 protons is assumed in all cases.

Energy	Ch. Had.	Muon
7 TeV	31.5	3.3
3.5 TeV	12.5	0.9
450 GeV	3.4	0.2

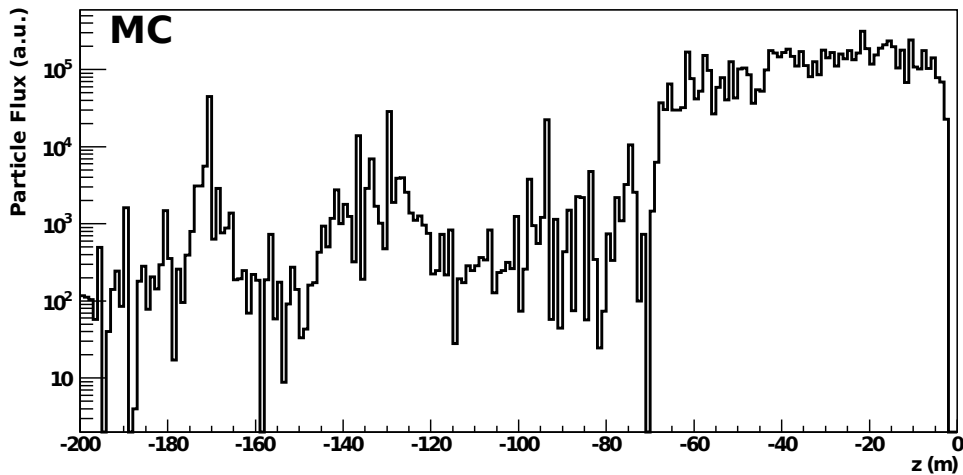


Figure 5.8: Beam-gas in LSS origin example. The plot shows the particle flux into the cavern caused by beam-gas interactions at various distances from the cavern. The low rate at position further away than -73 m is due to the TCTV located at this point. The sample used is LSS BG at 3.5 TeV for beam 1. The vertical axis is in arbitrary units.

5.3.2 Simulated Samples

In order to ascertain the effect of MIB on the experiment simulated data samples must be produced. This is done through the usage of the Gauss simulation application and the Boole digitization application. See section 3.7 for more information on the LHCb software.

All sample types are processed using the normal analysis chain. The applications are set up according to the relevant simulation conditions and versions available at the time. For the MIB analysis three types of simulated samples are of interest; MB samples, MIB samples and beam-gas in VELO samples.

MB Event Samples

The MB events are created using Pythia as the generator. Each event contains one or more proton-proton non-elastic interactions where no requirement is set on the nature and kinematics of the products. Such events should represent the physics of the beam-beam interactions at the IP of the experiment. The settings used in generating the events vary according to the related scenario.

MIB Samples

Two types of samples are created for the MIB analysis, pure and mixed. For the pure MIB samples Gauss is set up to use LbMIB as particle generator, taking the relevant background estimate files as input. This creates events consistent with the estimates and the resulting particles are transported through the experiment description giving hit information to the various sensor elements. For analysis purposes each sample only contains a single MIB source.

In the mixed sample, LbMIB is used in the same way as the pure samples, but in addition Pythia adds an MB event on top. Resultingly, each event has both MIB and MB. Particle transport is conducted in the same way in both cases. The first type of sample is used to investigate the direct effect of MIB on the experiment, while the second gives information on MIB and MB overlap.

Beam-Gas in VELO Samples

Events containing beam-gas in VELO are generated using Hijing [48] as it is particularly suited for the simulation of proton-atom interactions. For each energy level, two types of samples exist, proton-hydrogen and proton-oxygen. As the name indicates these simulate the interaction between beam protons and the relevant gas atom. The files give these interactions in the space of $-1 \text{ m} < z < 1 \text{ m}$ and are referred to as VELO BG. As with the MIB samples, these simulations exist independently for beam 1 and beam 2, as their impact on the detector differ.

5.3.3 Recorded Data Samples

The LHCb physics data samples are recorded at various conditions and settings. These are variations in machine settings, trigger setup, software versions, and so on. The appropriate settings are also applied to the simulated data when comparing the two in order to avoid unintended bias differences in versions.

For MIB analysis the data sample is split in subsamples depending on the bunch crossing type. One sample contains only events where two bunches cross each other, called beam-beam (BB), while the other two contain only events where only one of the bunches are filled. This is called beam-empty (BE) and empty-beam (EB) depending on whether beam 1 or beam 2 has a filled bunch, respectively. The BE/EB data samples should be free of beam-beam interactions and thus ease MIB analysis.

The BB data however should be describable through a combination of beam-beam interactions, beam-gas interaction within the experiment and machine induced background arriving from outside the cavern. This can be simulated through MB, VELO BG and MIB events, respectively. In order to attain data distributions equivalent to pure beam-beam interactions, the BE/EB data can be subtracted from the BB data with a scaling factor equivalent to the relationship between the bunch population of the bunches used in the BB sample versus the ones used in BE/EB. The result is called a *beam-gas subtracted* distribution (though all forms of MIB are subtracted). Such distributions should be comparable with the MB simulated events. It is assumed that the characteristics of colliding and non-colliding bunches is equivalent in all respects except the population (which is taken into account in the subtraction).

5.3.4 VELO Multiplicity

As described in section 5.3.1 the MIB estimates, though peaking at low multiplicities, contain a tail of high multiplicity events. This section investigates this MIB features, comparing it with MB events in order to gain an understanding of the multiplicity in the data.

For a quantitative comparison the VELO cluster multiplicity is used. As a particle traverses a VELO sensor, several adjacent channels can register a signal. VELO clusters are created through the combination of this electronic signal in order to create an object representing the particle hit. A traversing particle thus leaves a train of clusters in the VELO. Ideally these are reconstructed into an appropriate particle track candidate.

VELO Multiplicity at 450 GeV

During the initial runs at 450 GeV in 2009 events with high multiplicity were seen. Such events are not apparent in MB simulations, thus giving incentive to investigate the MIB sources.

As can be seen from figure 5.9 a typical high multiplicity event contains a large amount of tracks, and additionally these tracks seem to be pointing to a location upstream of the experiment. This is a further indicator to the origin of the event. The

particles of an MIB event have an origin outside the experiment, thus one can expect the resulting tracks to be pointed accordingly.

LHCb Event Display

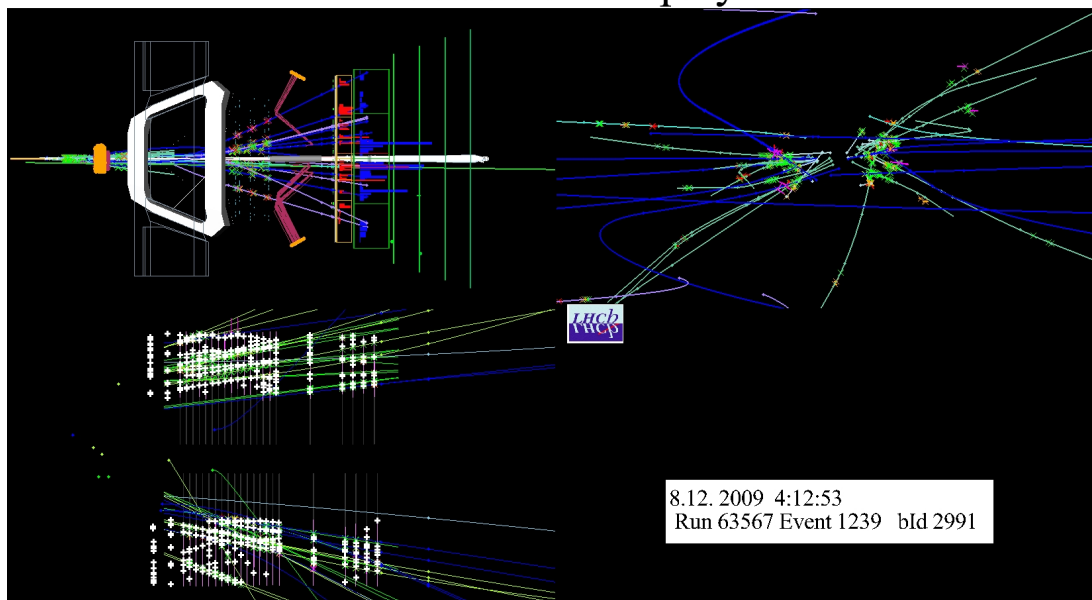


Figure 5.9: Recorded high multiplicity event at 450 GeV. Upper left corner show the reconstructed tracks in the experiment as seen from above. The lower left corner zoom in on the tracks in VELO and the related clusters. The tracks point to outside the experiment, a characteristics of an MIB event. In the upper right corner the tracks are seen in the xy plane. Event are taken from run 63567.

Not unexpectedly, as can be seen in figure 5.10, high multiplicity events are present in the MIB sample. In this case the 450 GeV LSS BG sample for beam 1 is used. In both cases events with over 800 clusters have been considered. The MIB events themselves do not have a higher multiplicity than proton-proton interactions. However, the distance to the experiment allows the particle shower to fully develop, resulting in a increased multiplicity in the sensors.

The cluster multiplicity for MIB and MB samples is shown in figure 5.11(a). As can be seen the MB sample has a multiplicity peak at 100 and a cutoff at about 350 clusters per event, while MIB contains a tail which reaches for higher values.

Figure 5.11(b) shows the VELO multiplicity for BE and beam-gas subtracted BB events. From comparison of the two plots one can see that the multiplicity of the BE events closely resemble that of the MIB. The multiplicity of MIB thus seems to be well described in the simulations. The beam-gas subtracted BB events should represent close to a pure proton-proton interaction sample. As in the MB events, this distribution peaks at an intermediate multiplicity and falls sharply towards a cutoff. In the data this peak is at 150 with a cutoff at 400, which is slightly increased compared to MB. However, the general shape is similar to the simulated sample.

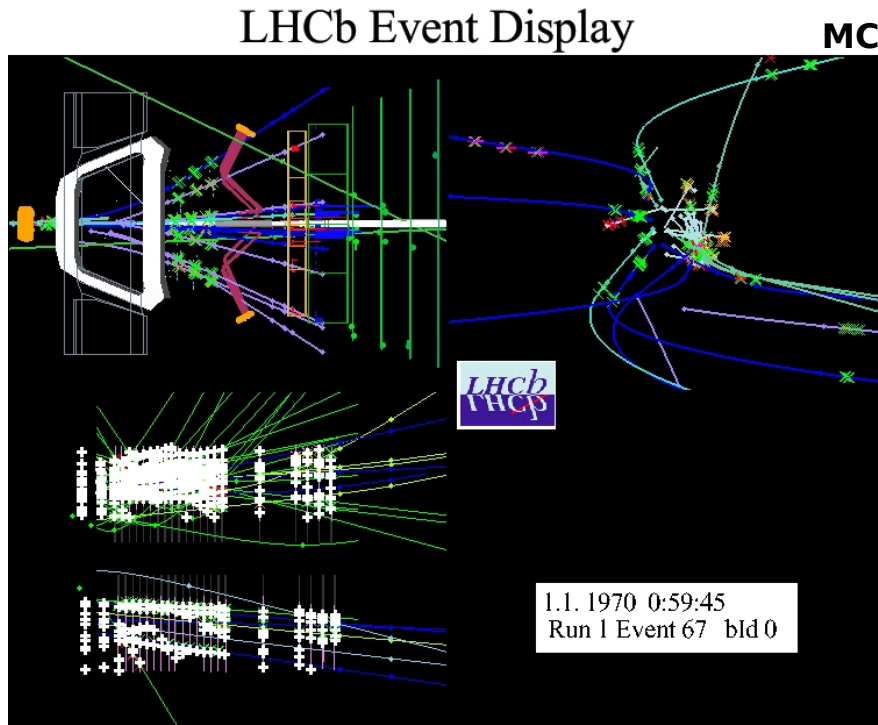


Figure 5.10: Simulated MIB high multiplicity event at 450 GeV. Upper left corner show the reconstructed tracks in the experiment as seen from above. The lower left corner zoom in on the tracks in VELO and the related clusters. The tracks point to outside the experiment. In the upper right corner the tracks are seen in the xy plane.

From these observations one can conclude that the MIB simulated multiplicity closely describes the real BE/EB distribution. Furthermore, the large multiplicity event observed in the 450 GeV data in 2009 could be explained through the existence of such MIB events in the sample.

VELO Multiplicity at 3.5 TeV

Having seen events with high VELO multiplicities in the 450 GeV data and its relation to MIB, this effect should also be investigated for 3.5 TeV. However, as can be seen from figure 5.12(a) the difference in multiplicity for MIB and MB events is not as apparent as at 450 GeV. Both distributions have a close to exponential falloff towards higher multiplicities.

Figure 5.12(b) shows the cluster multiplicity for BE and BB events. Two points present themselves in these plots. Firstly, the data confirms that the BB events and thus the proton-proton interactions can give high multiplicities at 3.5 TeV. Secondly, though high multiplicity events do occur in the BE data, the tail seen in the simulated MIB sample is not as prominent.

In conclusion, at 3.5 TeV the multiplicity difference between proton-proton inter-

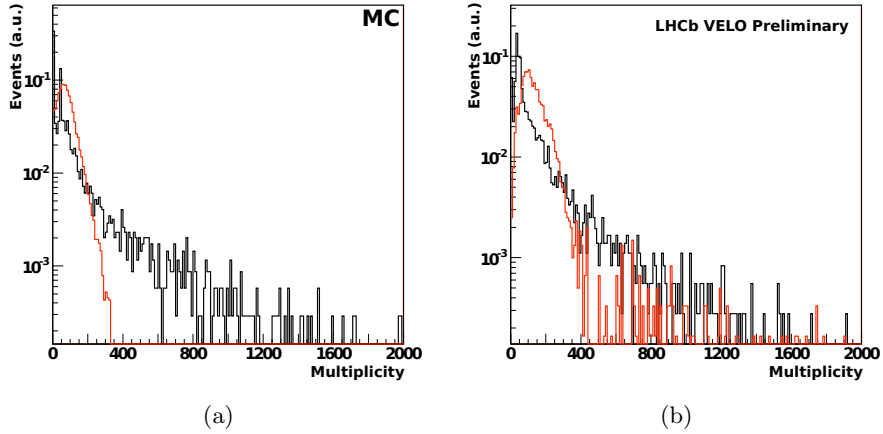


Figure 5.11: Multiplicity of VELO clusters at 450 GeV. Figure 5.11(a) shows the result of MB (red) and MIB (black) simulations while figure 5.11(b) shows recorded beam-gas subtracted BB (red) events and BE (black) for comparison. The vertical axis is in arbitrary units.

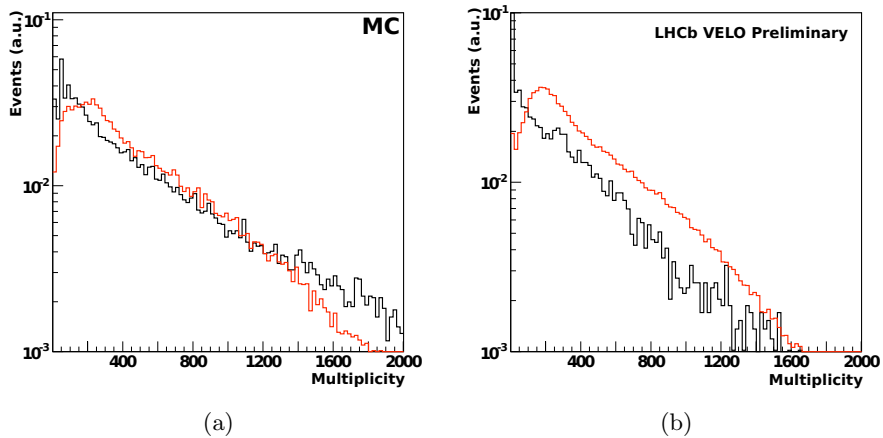


Figure 5.12: Multiplicity of VELO clusters at 3.5 TeV. Figure 5.12(a) shows the result of MB (red) and MIB (black) simulations while figure 5.12(b) shows recorded BB (red) and BE (black) events for comparison. The vertical axis is in arbitrary units.

actions and MIB is minimal, and resultingly can not be used as a criterion for discriminating between the two, as was possible at 450 GeV.

5.3.5 MIB Selection

In order to gain an understanding of MIB, separating it from other particle sources is essential. This involves creating a selection able to choose MIB events while discard-

ing proton-proton interaction and VELO BG, thus increasing the MIB fraction of the sample. By investigating the characteristics of the simulated samples, an approach to distinguish the various components in data can be developed.

As the MIB events arrive from comparatively far away from the experiment, it can be assumed that the particle tracks will have a flat slope with respect to the direction of the beam line. Furthermore, as the particles are not arriving from the interaction point, they should not point to this location.

Two variables readily present themselves, namely track slope (s) and radial distance to the nominal IP (r_0). The track slope is defined as the fraction of movement in the radial plane per unit in the direction of the beam line as shown in equation 5.8. r_0 gives the radial distance of the track to the ideal IP (Coordinates (0,0,0)) at the vertical plane of $z = 0$.

$$s = \sqrt{\left(\frac{dx}{dz}\right)^2 + \left(\frac{dy}{dz}\right)^2} \quad (5.8)$$

As one wants to perform these measurements on tracks non-perturbed by the magnetic fields, VELO tracks are used. Such tracks are created from VELO clusters, without using any information from other detectors in order to simplify the procedure.

Figure 5.13 shows the distribution of these variables for MIB, MB and VELO BG events at 450 GeV and 3.5 TeV.

Selection Optimization

The aforementioned variables are related to the tracks and not to the event as a whole. In order to filter the events, an event cut must be applied. One possibility is requiring at least one track with MIB characteristics, i.e. a track with a flat slope traversing the VELO at a certain radial distance from the IP.

In order to ascertain the effect of the cut, efficiency plots are generated. These show the fraction of events surviving the cut at various cut values. The two samples to distinguish are plotted on the axis of the plot. Resultingly, a point in the graph represents a given cut value and the axis values give the efficiencies of the related sources.

For a first analysis and understanding of MIB, the primary objective is to attain a pure MIB sample. The easiest way to accomplish this is through the use of the BE data as it does not have beam-beam interactions and thus can be described by MIB and VELO BG alone. To separate between the two, the efficiency plots are used where the two sources are plotted against each other.

Investigations have been performed on both 450 GeV and 3.5 TeV samples, however, with emphasis on 3.5 TeV. Currently the majority of data has been recorded at this energy level. This section will focus on 3.5 TeV. The corresponding result for 450 GeV are given at the end of the section. In order to accommodate the comparison with data, the L0 trigger has been applied to the simulated sample, using the same settings as were present during data taking.

The aim of this proceeding is to create a MIB enriched sample without a strong reduction of the statistics of the simulated samples. If, in the future, these selections will

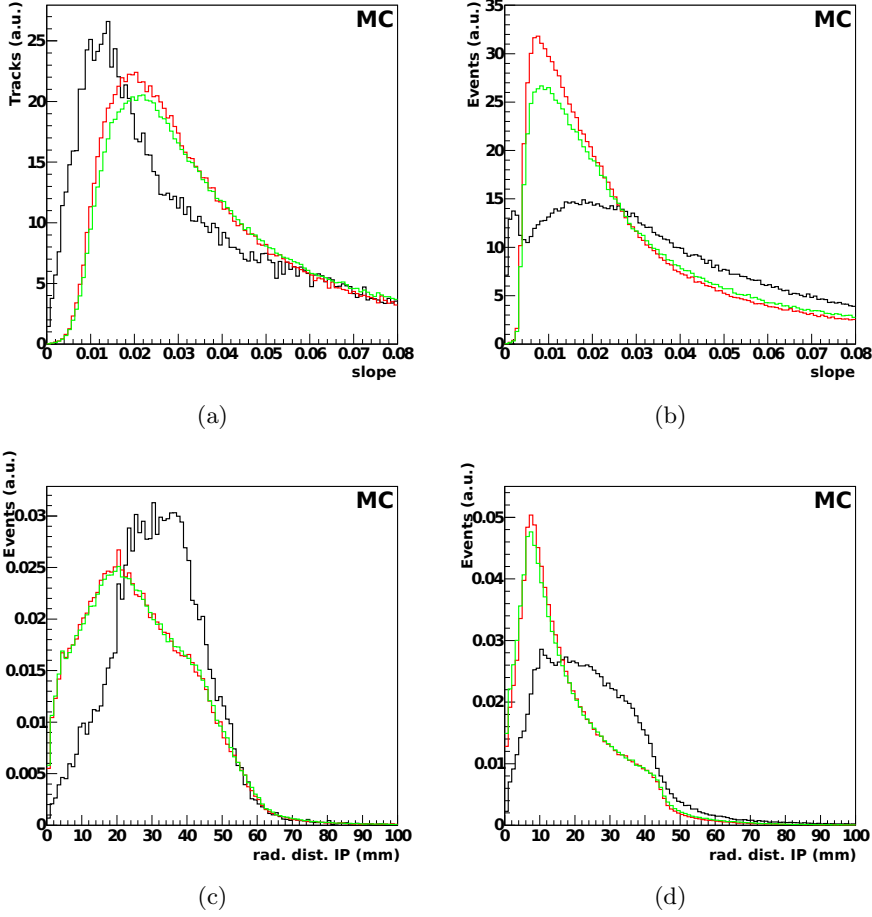


Figure 5.13: MIB selection variables. Track slope (upper row) and radial distance to IP (lower row) are show for 450 GeV (left column) and 3.5 TeV (right column) simulated samples. Black lines represent beam-gas in LSS, while red and green are beam-gas interactions in VELO due to hydrogen and oxygen respectively. The vertical axis is in arbitrary units.

be used in a trigger or stripping (off-line selection) of the data, they will be optimized to attain the maximal MIB efficiency at a given output rate.

Figure 5.14(a) shows that cutting on the slope of the tracks result in little loss of MIB, while the beam-gas in VELO is strongly reduced. For the slope, a cut value of 0.004 has been chosen as a compromise between MIB efficiency and VELO BG reduction. Figure 5.14(b) and 5.14(c) show the efficiency of the radial distance to IP cut with and without the slope cut on the same tracks. For the first figure, no particularly good cut presents itself. However in the second, considering the tracks with a low slope, an efficiency drop is seen at a distance of about 10 mm. Thus this value is chosen for the cut.

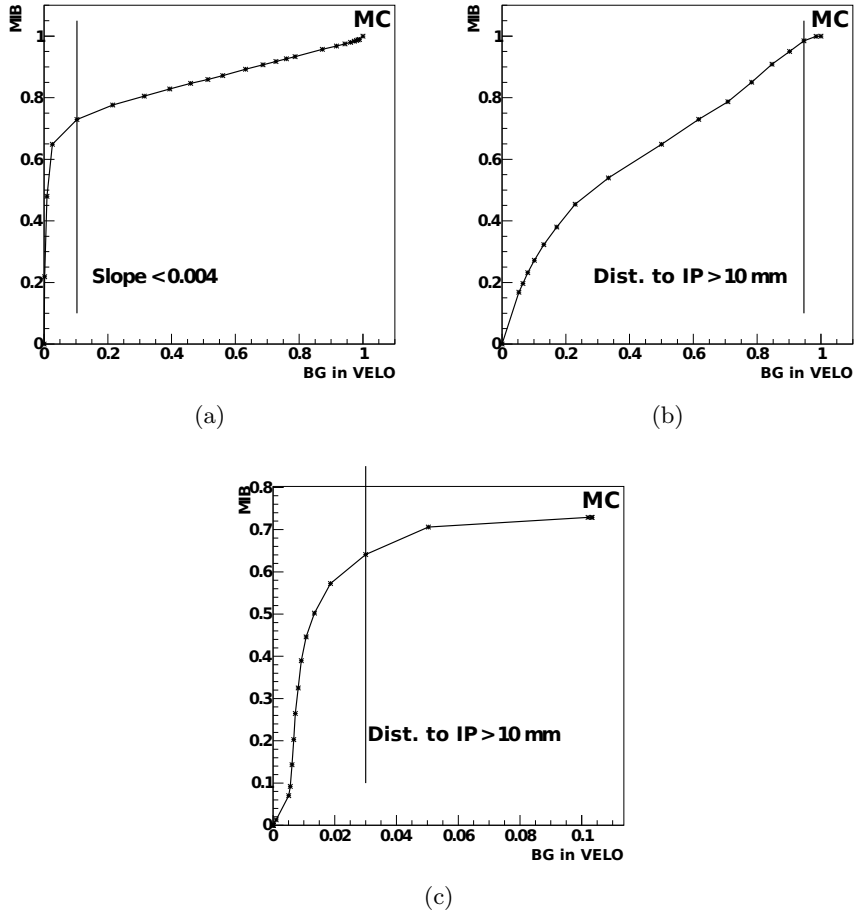


Figure 5.14: MIB selection efficiency depending on different cut variables at 3.5 TeV. Figure 5.14(a) and 5.14(b) show the efficiency of MIB versus beam-gas in VELO for variations of the slope and radial distance cut, respectively. Figure 5.14(c) shows the efficiency variations of the radial distance cut with a fixed slope.

Table 5.11: Cut Efficiencies at 3.5 TeV on various simulated samples for selection of MIB events from beam 1.

Source	s	r_0	s and r_0
MB	0.2%	75.0%	0.1%
B1BGLSS	72.9%	98.4%	64.1%
B1BGVELO,H	10.3%	94.6%	3.0%
B1BGVELO,O	11.6%	97.2%	3.4%

The efficiencies resulting from these cuts are listed in table 5.11. The MIB source retains a large fraction of events while the other sources are reduced significantly. Using

these cuts and folding in the efficiencies, it is possible to get a hold on the rate of MIB in the data sample as will be shown in section 5.3.7.

For 450 GeV the same procedure is followed, resulting in a slope cut of 0.01 and a radial distance to the IP of 20 mm. The corresponding efficiencies are listed in table 5.12.

Table 5.12: Cut Efficiencies at 450 GeV on various simulated samples for selection of MIB events from beam 1.

Source	s	r_0	s and r_0
MB	0.3%	41.3%	0.1%
B1BGLSS	71.0%	97.4%	64.1%
B1BGVELO,H	15.3%	87.0%	4.2%
B1BGVELO,O	18.7%	92.8%	5.9%

5.3.6 MIB Effect on Trigger

The LHCb trigger system as described in section 3.6 has been optimized using simulations of proton-proton interaction events. This approach does not take MIB into account and thus the impact of such particles should be investigated.

As the recorded data has, by definition, passed the trigger, comparison with the MIB simulations can only be made if the effect of the trigger on these events is known. To this end the trigger has been applied to the various simulated samples, recording rates and efficiencies.

As previously described, the trigger consists of three levels; L0, HLT1 and HLT2. There are multiple configurations of the trigger lines depending on the energy level and filling scheme of the LHC, as well as trigger version of the time of recording. The various trigger settings are defined through a unique trigger configuration key (TCK).

For the 450 GeV and 3.5 TeV samples only the L0 trigger will be investigated. During 2009 and early 2010 data only L0 was active. At the later samples of 2010, HLT1 was used, but HLT2 still ran in pass-through mode meaning it did not discard any events.

This section will investigate four scenarios: 450 GeV L0 trigger, 3.5 TeV early 2010 L0 trigger, 3.5 TeV late 2010 L0 trigger and 7 TeV nominal L0 trigger. For the two initial samples, the TCK is chosen to match a certain data sample in order to accommodate comparison. The late 2010 trigger, as well as the 7 TeV trigger act as indicators to the future expectations.

MIB can affect the trigger in two ways; increased rates through selection of MIB events and interference between proton-proton interactions and MIB in the same event, changing selection probability. In early samples the bunch-bunch interaction probability was so low that the overlap between proton-proton events and MIB was minimal. However, as the beam current increases this effect gets more prominent. Furthermore, the trigger settings are tightened as the current increases, resulting in a lower selection

efficiency on pure MIB events. The type of investigation performed is thus indicated in the relevant section.

Trigger on MIB at 450 GeV

For the 450 GeV data taking a *minimum bias trigger* was used. This setting only uses a simple version of the L0 trigger, containing three lines: The calorimeter line (CALO), muon line (MUON) and pile up line (PU). A trigger is given if any of the lines accept the event. The minimum bias trigger is not to be confused with the minimum bias samples. The first is a trigger line searching for any proton-proton interactions at the IP, while the second is a sample of simulated beam-beam interactions.

The TCK used in these investigations is 0x1309, and at this TCK the CALO line requires at least two hits in the SPD and a transverse energy deposition of more than 240 MeV in the HCAL (see section 3.5.7 for information on the calorimeter). The MUON line sets a requirement on the transverse momentum of a muon track to be above 480 MeV/c. Lastly the PU line requires a multiplicity of at least seven in the pile-up sensors inside the VELO chamber.

Due to the low interaction probability for the 450 GeV bunches the amount of events containing both a proton-proton interaction and MIB particles is expected to be at the per mille level. As such the MB and MIB events can be treated completely independent of each other. Table 5.13 shows the trigger efficiency (probability) for the three lines and the L0 as a whole for various simulated samples.

Table 5.13: 450 GeV L0 trigger efficiencies total and per line for various simulated samples.

Source	CALO	MUON	PU	Total
MB	62.9%	0.5%	3.2%	63.0%
B1LSSBG	35.4%	0.8%	4.9%	36.3%
B1VELOBG,H	83.5%	0.5%	2.4%	83.6%
B1VELOBG,O	93.9%	0.9%	5.8%	93.9%
B2LSSBG	0.0%	0.0%	0.9%	0.9%
B2VELOBG,H	0.0%	0.0%	0.6%	0.6%
B2VELOBG,O	0.0%	0.0%	2.4%	2.4%

From the table one can see that these trigger settings result in a large probability of triggering on beam gas events both from the LSS and inside the VELO. Because of the out-of-time nature of beam 2, the beam-gas from that side only triggers on the pile up line, and at a very low probability.

Trigger on MIB at 3.5 TeV

The 3.5 TeV data taking has used many different L0 trigger configurations. In this thesis two of these will be considered, namely TCK 0x1810 and TCK 0x002A. These

represent early and late settings of 2010, and thus an increasing tightness of cuts. Unlike for the 450 GeV triggers the 3.5 TeV triggers run several lines containing selection algorithms specific for a given particle species. The main collections of lines are muonic, hadronic, electron, photon, π_0 and beam-gas. Muonic triggers entail both single and di-muon trigger, π_0 contains both global and local trigger lines, and beam-gas trigger for beam 1 and 2 are included in the beam-gas collection. The beam-gas triggers are created to select beam-gas in the VELO and not in the LSS.

While both configurations contain these lines, the tightness of the selection increased over the 2010 data taking period, and thus the reduction rate of TCK 0x002A is considerably higher than in 0x1810. Furthermore, the early trigger contained the minimum bias triggers shown in the 450 GeV section, though this was quickly reduced through pre-scaling as the data rates went up.

In the early 3.5 TeV data taking the rate was still low, thus overlap between MIB and proton-proton events is negligible. This rate went up as the mean number of proton-proton interactions per bunch crossing increased. For this reason, trigger rate on MIB at 3.5 TeV will be shown for both MIB alone and MIB combined with an MB event.

Table 5.14 and 5.15 show the trigger efficiencies attained using the aforementioned TCKs. The values for BVELOBG are show for completeness.

Table 5.14: 3.5 TeV early L0 trigger efficiencies per trigger category for various simulated samples. The categories are minimum bias, muonic, electron, photon, hadron, neural pion and beam-gas triggers. The values are for TCK 0x1810.

Sample	m. b.	μ	Elec.	γ	Had.	π_0	BG	Total
MB	78.2%	4.0%	25.9%	0.3%	36.2%	1.8%	61.1%	80.0%
B1LSSBG	50.7%	4.5%	4.3%	0.0%	8.0%	0.0%	32.9%	59.7%
B1TCTHH	6.0%	4.1%	0.0%	0.0%	0.3%	0.0%	0.3%	7.6%
B1VELOBG,H	87.5%	2.2%	18.2%	0.0%	23.5%	0.1%	60.3%	93.3%
B1VELOBG,O	96.0%	3.9%	31.7%	0.0%	40.4%	0.3%	81.3%	98.2%
B1LSSBG & MB	89.8%	9.6%	19.4%	0.1%	29.0%	0.9%	63.3%	92.2%
B1TCTHH & MB	89.1%	12.0%	24.2%	0.1%	35.2%	1.3%	63.2%	90.6%

The early L0 trigger line was quite open. As can be seen from the 80% selection efficiency on MB event, only a certain activity in the detector was needed to fire the trigger. The background sources are also triggered with a high probability, except the B1TCTHH source. This source mainly triggers on the muonic and minimum bias lines. The related particle shower is generated at about 118 m from the IP, and needs to pass all the shielding located between the TCTH and the experiment. As a result the hadronic component of the shower is reduced and strongly peaked at low radii as was shown in figure 5.3(b). Furthermore, a simulation related issue must also be considered. The MIB estimate file for this source does currently not contain any electrons or photons, thus the related trigger lines will have a reduced rate. In general the B1TCTHH source should be re-evaluated when an estimate containing these particles

Table 5.15: 3.5 TeV late L0 trigger efficiencies per trigger category for various simulated samples. The categories are muonic, electron, photon, hadron, neutral pion triggers. The values are for TCK 0x002A.

Sample	μ	Elec.	γ	Had.	π_0	Total
MB	1.2%	0.3%	0.2%	1.5%	1.3%	3.1%
B1LSSBG	3.0%	0.0%	0.0%	0.1%	0.0%	3.1%
B1TCTHH	4.1%	0.0%	0.0%	0.0%	0.3%	4.1%
B1VELOBG,H	0.6%	0.0%	0.0%	0.1%	0.1%	0.8%
B1VELOBG,O	1.0%	0.0%	0.0%	0.2%	0.2%	1.4%
B1LSSBG & MB	5.4%	0.2%	0.1%	0.5%	0.7%	6.2%
B1TCTHH & MB	7.4%	0.2%	0.1%	0.8%	1.0%	8.5%

is made available.

The events with overlapping MIB and MB events have, as expected, a higher trigger probability. This effect arrives mainly from the muonic triggers, giving an increase of a factor 2 to 3. Some trigger lines have a probability reduction when compared to the pure MB sample. The relevant lines have a multiplicity limit, and thus events with higher particle population can get a trigger efficiency reduction.

The settings of the late L0 trigger is comparatively tight, giving an MB efficiency of about 3%. The MIB samples are of the same order, however, these are mainly triggered on the muon lines, while the MB sample has a more balanced triggering scheme. The MIB and MB overlapping events display a selection probability equal to or higher than the sum of the individual probabilities. This is due to the fact that the MIB and MB events might not individually be able to overcome the trigger thresholds, but the combination of the two may. In particular this is true for triggers requiring a certain energy deposition and / or number of particles.

As the 0x002A trigger setting is representative of what is expected to be used in 2011 runs, it is important to understand the implications of these results. The MIB events trigger with a probability equivalent to MB, and the mixed event with about the double. Resultingly the MIB rate must be kept under control as the L0 trigger can not be trusted to remove such events. Currently predicted MIB rates are however expected to be small compared to MB, thus MIB should not cause problems in the trigger unless adverse conditions occur.

Trigger on MIB at 7 TeV

Before data taking was initiated in 2009, a set of trigger settings for the nominal 7 TeV machine mode was created. This trigger assumes a bunch crossing rate of 31.6 MHz, and about 16 MHz visible events in LHCb. For this, a reduction to an output rate of 1 MHz is stipulated, thus representing a reduction factor of 93.75%. As the rate of 1 MHz represents the ultimate configuration, only small fluctuations from this value can be tolerated. For the trigger studies one defines a variation from the expected output rate

by more than 10% as a problem and thus a cause to retune the trigger.

The 7 TeV trigger, like the late 3.5 TeV, contains several trigger lines which can be contained in particle species categories. As this scenario depicts a situation in where about 50% of all bunch crossings result in at least one proton-proton interaction, the events containing both such events and MIB are of main interest.

Table 5.16 shows the trigger probability for the various L0 lines for MB alone as well as with various MIB sources. For a standard MB event the trigger probability is expected to be 6.6%. In the case where, for example, a MB event occurs at the same time as a B1TCTVVF MIB event, this increases to 7.7%. In short, this means that if there is MIB in each MB event, the trigger rate would go up by 17%. However, it is possible to have both multiple MIB showers in a single event and, as is expected, MIB in only a subset of the MB events. As was seen for 3.5 TeV, the major rate increase contributor is the muon lines. I.e. these are the least robust lines when faced with increased background.

Table 5.16: 7 TeV L0 trigger efficiencies per Line for various simulated samples.

Sample	L0	μ	Di- μ	Elec.	γ	Had.	π_0 l.	π_0 g.
MB	6.6%	2.2%	0.3%	1.0%	0.4%	4.0%	0.5%	0.4%
B1TCTHH & MB	9.3%	3.7%	0.5%	1.3%	0.5%	5.0%	0.7%	0.6%
B1TCTHV & MB	8.1%	3.3%	0.3%	1.2%	0.4%	4.1%	0.6%	0.5%
B1TCTVVQ & MB	8.5%	3.4%	0.4%	1.2%	0.4%	4.3%	0.5%	0.7%
B1TCTVVH & MB	7.8%	2.9%	0.4%	1.1%	0.5%	4.2%	0.7%	0.6%
B1TCTVVF & MB	7.7%	2.9%	0.4%	1.1%	0.4%	4.1%	0.6%	0.6%
B1TCTVVT & MB	7.8%	3.0%	0.4%	1.1%	0.4%	4.2%	0.6%	0.6%

5.3.7 MIB Rate Measurements

Assuming that the simulation samples give a satisfactory description of the physical data, they can be used to determine the rate of each source. In order to test this assumption, the distribution of the variables introduced in section 5.3.5 must be checked on the data. For the 450 GeV data the runs 63686, 63801 and 63813 are used, while for 3.5 TeV runs 69666 to 69672 are used. The background conditions depend on machine settings, so for the rates attained from simulation, conditions similar to these runs have been used.

BE data should not contain any proton-proton interactions, as only one of the beams contains a filled bunch. Resultingly, its distribution should be equivalent to that of a linear combination of MIB and VELO BG. The distributions from figure 5.13, are combined in such a way that the square of the difference between the combination and the BE data distribution is minimized. Figure 5.15 and 5.16 show this approach for slope and impact parameter, respectively.

Using this approach the resulting fractions are as listed in table 5.17. In an ideal situation, the track slope and radial distance to IP results should be equivalent, however,

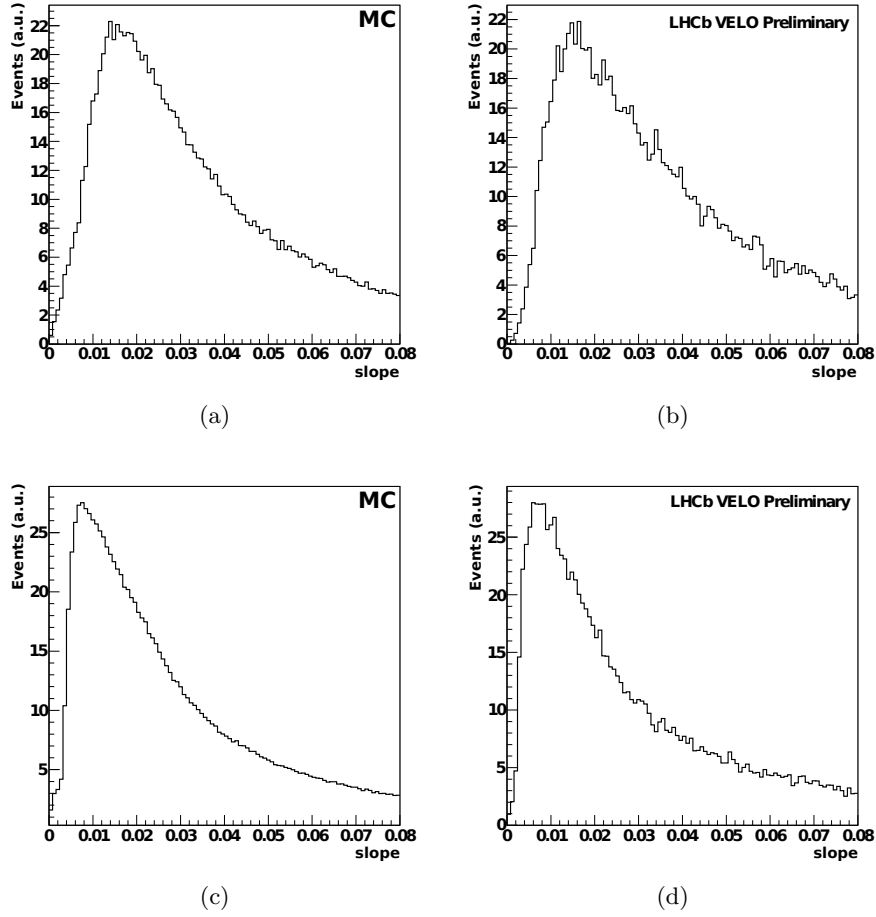


Figure 5.15: Track slope mix. Figure 5.15(a) and 5.15(c) show a mixture of beam-gas in LSS and VELO optimized to resemble the data in figure 5.15(b) and 5.15(d) as close as possible. The upper column contains plots for 450 GeV, while the lower column is 3.5 TeV. The vertical axis is in arbitrary units.

this is a rough measurement and should only be taken as an indication of the magnitude. In order to get a more precise measurement a cut based approach is used.

Table 5.17: Beam-gas fractions obtained by minimizing the difference between a mixture of beam-gas in LSS and VELO, and the measured data.

Distribution	MIB	VELO BG
s , 450 GeV	36%	64%
r_0 , 450 GeV	49%	51%
s , 3.5 TeV	22%	78%
r_0 , 3.5 TeV	36%	64%

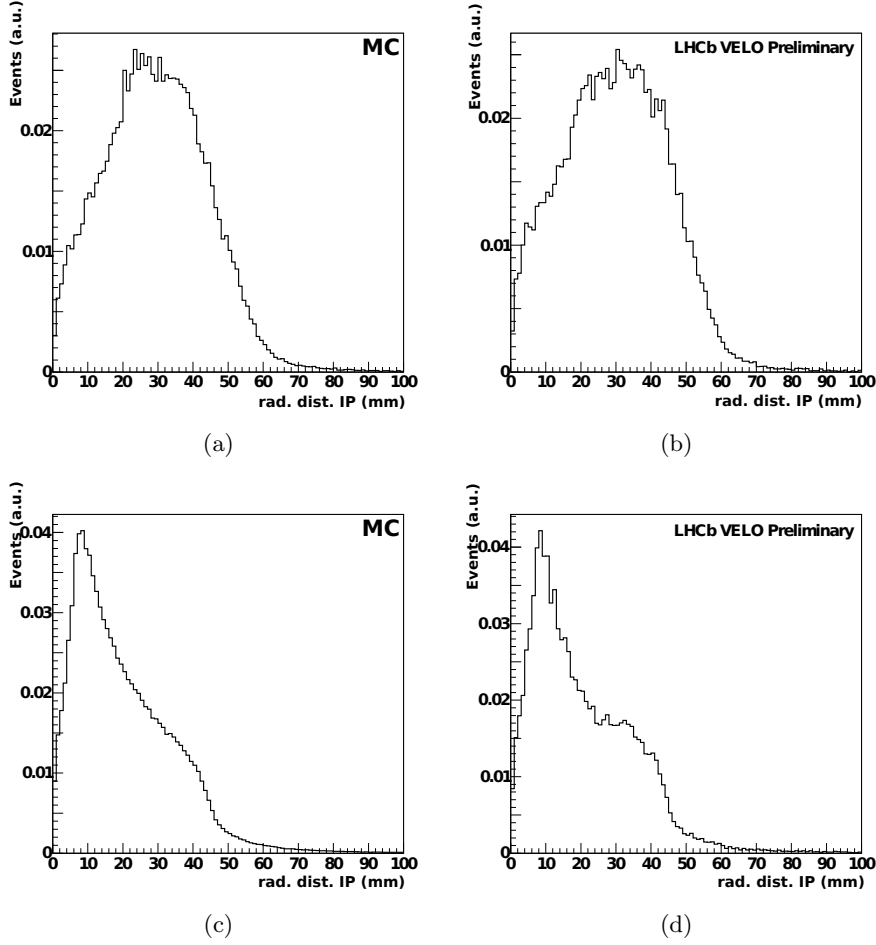


Figure 5.16: Radial distance to IP mix. Figure 5.16(a) and 5.16(c) show a mixture of beam-gas in LSS and VELO optimized to resemble the data in figure 5.16(b) and 5.16(d) as close as possible. The upper column contains plots for 450 GeV, while the lower column is 3.5 TeV. The vertical axis is in arbitrary units.

The cuts used to select MIB are described in the previous section and the resulting efficiencies on the simulated samples are shown in table 5.11 and 5.12.

Applying the cuts on a 450 GeV BE sample, the resulting efficiency is 25.7%. Comparing this with the simulated efficiencies (and assuming they are correct), the MIB fraction at 450 GeV is 36%. Utilizing the same procedure on the 3.5 TeV BE sample, the efficiency is 19.6%, resulting in a MIB fraction of 27%. These numbers are also listed in table 5.18 and correspond well to the ballpark estimates of table 5.17.

In order to calculate back to a MIB proton loss rate, several efficiencies have to be folded in as seen in equation 5.9. The BE frequency in data (f_{BE}) is multiplied with the ration of MIB in the sample (R_{MIB}) as calculated above. This is divided by the efficiencies of trigger on MIB events ($\epsilon_{trigger}$) as well as the visibility ($\epsilon_{visible}$).

Table 5.18: Beam-gas fractions obtained using a cut based approach.

Distribution	MIB	VELO BG
450 GeV	36%	64%
3.5 TeV	20%	80%

The visibility is the fraction of proton losses that result in at least one particle at the interface plane. The result is the frequency of proton losses at the given particle current for BE bunches. This can be compared to the estimates as will be shown in the following sections.

$$f_{\text{protonloss}} = \frac{f_{\text{BE}} \times R_{\text{MIB}}}{\epsilon_{\text{trigger}} \times \epsilon_{\text{visible}}} \quad (5.9)$$

450 GeV MIB rate

During the 450 GeV runs, two bunches contributed to the BE events, each with a population of 2×10^{10} protons. The measured BE trigger rate was on average 1.8 Hz. The fraction of MIB events in a triggered sample is expected to be 36%, as shown above, and the trigger probability is also 36% as can be seen in section 5.3.6. The estimate files themselves indicate that for beam-gas in the LSS about 30% of the proton losses result in at least one particle at the interface plane.

Combining these factors result in an expected proton loss rate of 6 interactions per second at a proton population of 4×10^{10} . The expected rate from the estimates is 2.6 interactions per second. This number comes from the DPMJET and FLUKA MIB estimation stages of the related sample.

3.5 TeV MIB rate

At 3.5 TeV the rate is 2.0Hz, with a single BE bunch populated with 10^{10} protons. The expected MIB fraction is 27% as well as a trigger efficiency of 48% (using TCK 0x1810). In the estimate files about 20% of the proton losses are seen to give at least one particle at the interface plane.

Resultingly the proton loss rate in the LSS is calculated to be 5.6 interactions per second per bunch of 10^{10} protons. From the estimates we expect 0.7 interactions. This number is about one order of magnitude off, meaning that either the LSS BG interaction rate is underestimated or the MIB fraction of the data is overestimated. In both cases further studies outside the scope of this thesis should be pursued in the future.

5.4 Status of the MIB Simulation Work

The framework for simulating various MIB sources and determining their effect on the experiment is in place and works according to expectations. This includes the whole chain of simulations from initial proton loss, transport of particle shower to the

experiment, as well as generation and simulation of these particles within the LHCb software suite.

As the conditions of the LHC are affected by the running conditions, new estimates are, and will be, produced using the software presented. The 2013 machine upgrade involves a change in the collimator scheme of the LHC, thus estimates and simulations must be produced for these conditions in order to attain an understanding of the expected conditions.

The MIB simulations have been compared to the data recorded from non-interacting bunches during early runs. The kinematic properties of the simulated particles show similarities with the recorded data, thus giving assurance the estimation on MIB arriving at LHCb is fundamentally correct.

A selection procedure based on the kinematic properties of particles traversing the VELO currently allows a efficient selection of MIB particles. This procedure will be improved upon, aiming to allow the identification of various MIB sources in the data sample, as well as measuring their rates.

As machine conditions as well as trigger configuration evolves, further studies of MIB effect on the trigger might be called for. However, current results show that in the case of nominal background levels, MIB particle interference is minimal.

The estimates performed and the software developed is available to the whole collaboration and enables the various sub-detector groups to investigate the effect of MIB on their devices as well as estimating the radiation levels caused by such background particles. Investigations of the interference with track reconstruction and particle identification are also examples of fields where the MIB estimates and tools can be an asset.

Chapter 6

Simulations Performed for the Beam Condition Monitor

The Beam Condition Monitor (BCM) is a sensor system designed to protect the LHCb and in particular the VELO against adverse beam conditions. This system has been developed and built at TU Dortmund. In connection with this development various simulations have been performed in order to ascertain the optimal position and design as well as investigating beam dump thresholds and the effect of various beam failure scenarios. Furthermore in order to facilitate such simulations and to comply with LHCb policies the BCM detector description and algorithms have been included in the standard LHCb software suite.

While the general LHCb software suite was described in section 3.7, the BCM specific software is introduced in section 6.1. Simulations for the positioning and configuration of the BCM are contained in section 6.2. Beam dump thresholds and sensitivity ranges are investigated in section 6.3 and 6.4.

6.1 Algorithms and Components Developed for the BCM

Several components and algorithms have been developed in order to accommodate the execution of the simulations relevant to the BCM. Specifically these components are:

- Extension of the LHCb Detector Description
- The BCM Specific Simulation Algorithms (DeBcm, BcmMoni, BcmDigi)
- The Multiple Magnetic Field Service (MultipleMagneticFieldSvc)

6.1.1 Extension of the LHCb Detector Description

The LHCb detector description database (DDDB) contains xml-files describing the shape and material of all components of the experiment. A full description of the experiment is attained through information on the position and orientation of these components within the cavern. The result is a full 3D model of LHCb, including material properties to enable physics simulations.

The standard LHCb detector description consists of the components which could have an impact on the physics event simulations. This includes all sub-detectors and components located in the range $z \in [-1, 20]$ m. The downstream BCM station is located within this area, thus in order for the simulated particles to experience the same material distribution as is present in reality, it was created and added to the description. Resultingly it is present in all particle simulations including the standard physics samples.

The areas outside the aforementioned range are of interest for several studies, in particular the investigation of the machine induced background rates and various beam failure scenarios. As such the areas ranging from $z \in [-22, -1]$ m and $z \in [20, 22]$ m have been added and are currently available in the official detector description. This area is not used in the physics sample production, however, as it is outside the area of interest for such simulations. The components added are beam lines and vacuum chambers as well as beam pipe supports and shielding walls. In addition to this “dead” material there are a few active components in this region requiring additional algorithms. These are the upstream BCM station and the three compensator magnets. The algorithms required for the upstream BCM, also apply to the downstream version. Figure 6.1 shows the full detector description.

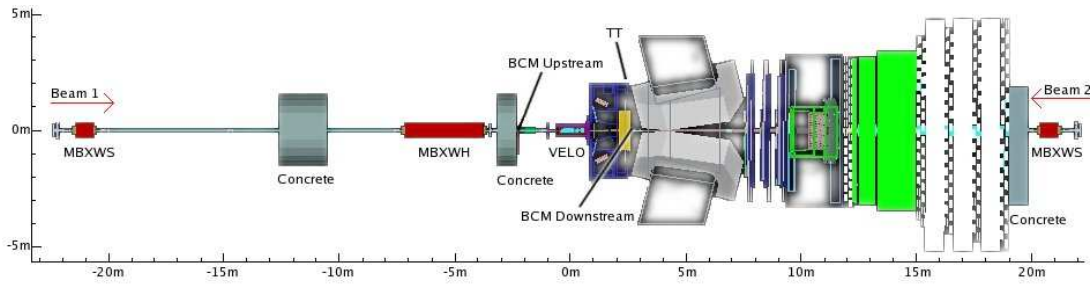


Figure 6.1: The LHCb detector up to the MBXWS magnets. All components in the regions $z \in [-22, -1]$ m and $z \in [20, 22]$ m have been implemented, as well as the downstream BCM located at the entrance of the main magnet. The detector is seen from the side.

6.1.2 The BCM Specific Simulation Algorithms

In order to record and monitor data related to traversing particles during the simulation a few algorithms and classes must be implemented.

Firstly in order to be able to define the BCM as a sensitive element and thus record particle hits a “DetectorElement” class must be defined for the BCM. The DeBcm package takes care of this, providing BCM specific information including station and sensor number of the relevant particle hit.

Secondly a digitization algorithm, BcmDigitization, has been created in order to transform the raw particle hits into a quasi-electronics output format. In general these

algorithms should give an output similar to what is expected from the hardware. However, the LHCb simulation software runs on a per-event basis, while the BCM has a much slower update rate. As such the digitized output only gives the energy deposit in the various sensors, which in turn can be summed up for the BCM time slot when analyzing the results. The digitization stage is needed for the BCM in order to propagate the simulation results to the file format used for analysis, and is generated at the Boole simulation step.

Additionally the package BcmMoni has been developed to provide monitoring of the BCM during simulation, facilitating further analysis of the simulation results. This algorithm saves information on the sensor hit and the associated particle. The results are saved in a ROOT tuple for quick analysis.

All the aforementioned components conform to the Gaudi and LHCb guidelines thus making them compatible and easily maintainable.

6.1.3 The Multiple Magnetic Field Service

As mentioned, the added upstream and downstream areas of the detector description contain three compensator magnets. The standard LHCb magnetic field service however only supports single magnetic fields as normally only one field is needed for the simulations. To remedy this problem the Multiple Magnetic Field Service has been implemented.

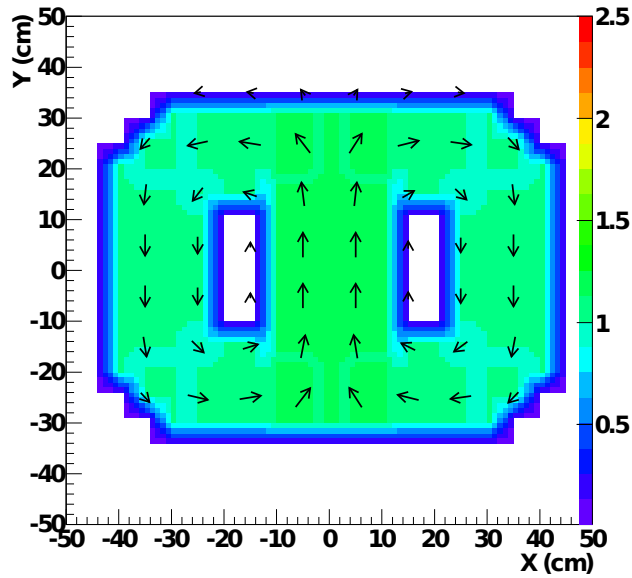
This service works as a wrapper, taking multiple normal magnetic field services as arguments. When requested to deliver the magnetic field vector at a given point in space a vector addition is performed using the field from all member services. In LHCb jargon a service is an object providing standard functions for the whole software system. Examples of such services are access to input and output files, particle property information access and of course magnetic field parameterization.

In addition magnetic fields for the compensator magnets have been created. Two generations of fields were created. The initial field (figure 6.2) was a simple hand made field assuring the design field strength in the central area of the beam line and giving an approximate description of the field lines, B_x and B_y , in the xy plane. The field has no variations in the z direction and also no B_z field strength.

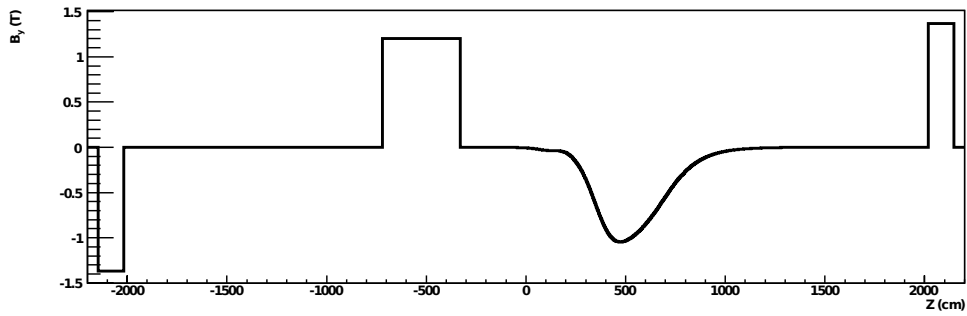
The second generation (figure 6.3) is based on measurements of the B_y components of the field in the central beam line area over the whole length of the magnets [49]. This is combined with two-dimensional simulations of the B_x and B_y components in the xy plane. Resultingly the vertical magnetic field in the central region is at the measured value, while the field lines in the xy plane are realistic. No B_z component exist, which is an acceptable simplification as this component is only relevant at the ends of the magnets.

6.1.4 Sensitivity Scan Tool

The sensitivity scan tool is a variation of the particle gun can produce particles with a randomly selected origin (x, y, z) and angle of travel with respect to the beam line

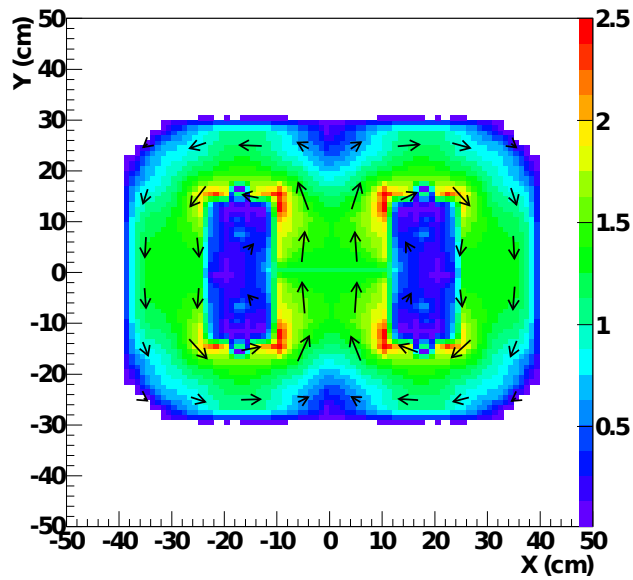


(a)

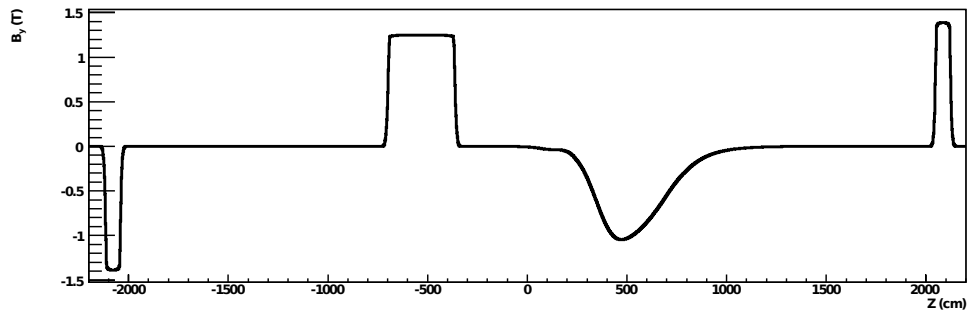


(b)

Figure 6.2: Initial compensator magnetic fields. The B_x and B_y distributions are hand-made. The values are constant over the whole length of the magnet. Figure 6.2(a) shows the field strength and direction in the xy plane. The beam pipe is centered at $x = 0$, $y = 0$. Figure 6.2(b) gives the vertical field strength along the central beam-line.



(a)



(b)

Figure 6.3: Current compensator magnetic fields. The B_x and B_y distributions are simulated. The values change over the length of the magnet according to measurement of the central B_y value. Figure 6.3(a) shows the field strength and direction in the xy plane. The beam pipe is centered at $x = 0$, $y = 0$. Figure 6.3(b) gives the vertical field strength along the beam-line.

(θ_x, θ_y) . The variation range of these parameters as well as particle type and energy can be specified by the user. In order to understand what parameter space is available to the beam protons without resulting in material interactions and energy depositions in sensitive detectors, this tool has been employed. In this document the usage of this tool is referred to as a *sensitivity scan*. In particular this tool has been developed to check the sensitivity range of the BCM as will be shown in section 6.4.

The sensitivity scans are performed by instructing the sensitivity scan tool to generate protons of either 450 GeV or 7 TeV from a fixed z position of ± 22180 mm from the IP. These particles are allowed to vary in the horizontal position and angle (x, θ_x) , while vertical position and angle (y, θ_y) are kept constant. The mentioned z position has been chosen as it is just in front of the compensator dipoles (MBXWS).

The reason for the scan being performed in the horizontal plane is due to two reasons. Firstly the LHCb magnetic fields mainly act in this plane, altering the trajectory of the beam particles and secondaries. Secondly the VELO halves are mobile in the horizontal direction and as such investigations of the VELO in the open position would have to be performed in this plane.

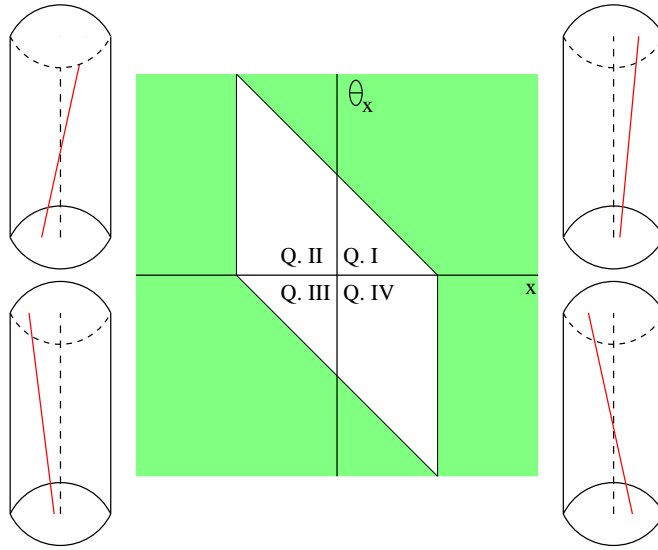


Figure 6.4: Beam scraping plot and beam path sketch. Protons are generated at position x with angle θ_x . The color indicates the signal strength in a given detector per proton. Quadrant I and III represent protons generated with angle and position offset in the same direction. Conversely quadrant II and IV have opposite direction and position, making the proton pass over the beam line center.

A sketch of a resulting plot is shown in figure 6.4. The axes give the horizontal angle and position at which the proton was generated. The color gives the average expected detector signal from single protons, i.e. each bin in the plot is scaled to one initial proton. The white areas thus represent the parameter range at which the proton is expected to stay within the beam pipe and not cause any particle showers upstream

of the detector position. In this document this area is referred to as the “blind” area of the detector. Conversely, the area showing signal is called the “sensitive” area. As will be shown later in this document, these plots can be scaled with a chosen beam distribution in order to attain a signal strength estimate for specific scenarios.

In order to reduce simulation time, the scans are performed with particle angle forced to have the same sign as the position as in these areas the two parameters both contribute to potential scraping. This removes the parameter space where a beam offset in one direction is compensated by an angle in the other. Resultingly only quadrant I and III from figure 6.4 are scanned while II and IV are ignored. Two parameter ranges are thus used:

- $x \in [x_{\min}, 0]$ with $\theta_x \in [\theta_{x_{\min}}, 0]$
- $x \in [0, x_{\max}]$ with $\theta_x \in [0, \theta_{x_{\max}}]$

Additionally, the plots are given with the absolute value of the angle resulting in both positive and negative scan being displayed in the same hemisphere. Or in other words the θ_x axis of quadrant III is inverted.

Due to an imperfection in the description of the vacuum in the beam pipe close to the IP, some unwanted interactions occur inside this area. This can be seen as a random noise signal in the blind area of the detectors. An example of this can be seen when comparing figure 6.7(a) and 6.7(c) where the random signal is visible in the downstream BCM, but not in the upstream. This effect is taken into account (by excluding the blind area) in the text of this document but kept in the plots for completeness.

6.1.5 Beam Shape Tool

The beam shape tool generates a “real” beam using relevant beam parameters, in order to analyze a specific scenario. The beam parameters used are the correlation function, α_i , the optical function β_i , and the transverse emittance, ϵ_i , where $i \in \{x, y\}$. These can be found on the LHC optics web page [37] and are given at multiple positions around the LHC ring. The values at IP8 are given in table 6.1. In order to investigate various failure scenarios, the beam centroid position, i_0 , and angle, θ_{i_0} are varied according to the chosen parameters.

Table 6.1: Beam parameters used in the simulations for the 450 GeV scenario as well as 7 TeV.

Scenario	Beam Energy [GeV]	α_x	α_y	$\beta_{x,y}$ [m]	$\epsilon_{x,y}$ [m]
Injection	450	4.18×10^{-7}	1.18×10^{-7}	10	7.82×10^{-9}
Physics	7000	2.24×10^{-7}	1.86×10^{-7}	10	5.03×10^{-10}

The beam is simulated as follows. A position i , where $i \in \{x, y\}$, is randomly chosen from a gaussian distribution around the centroid position i_0 with a standard deviation of

$$\sigma_i = \sqrt{\epsilon_i \times \beta_i} \quad (6.1)$$

Using the resulting position the cosine of the particle angle (dP_i) is chosen. This is given as a gauss distribution with central value of

$$dP_{i_0} = -\frac{\alpha_i}{\beta_i} \times (i - i_0) + \cos(\theta_{i_0}) \quad (6.2)$$

and standard deviation of

$$\sigma_{dP_i} = \sqrt{\frac{\epsilon_i}{\beta_i}} \quad (6.3)$$

The momentum of the protons are then set to the design value (i.e. no beam energy fluctuations) and the transverse components of the momentum are given as

$$P_i = P \times dP_i \quad (6.4)$$

This results in an idealized beam shape approximation tunable with the optics parameters.

6.2 Simulations for Determining the Optimal BCM Position and Configuration

As the BCM was added to LHCb late in the construction process, the space available for this device was rather limited. As such a suitable position had to be found. In connection with this, simulations were performed in order to determine the expected particle flux and coverage range of the device. The downstream BCM is located within the sensitive solid angle of the experiment and as such the radiation length of the device also had to be taken into consideration in order to minimize interference with physics measurements.

6.2.1 Position and Design of the Downstream BCM

The main criteria for the positioning of the BCM is closeness to the interaction point, and thus the VELO, and radial distance from the beam line center. For the downstream BCM there were two positions available. The first one was located on the beryllium pipe between the RICH1 and the TT, while the second was behind the TT, at the entrance of the magnet.

Though the position between the RICH1 and the TT was better with respect to both radius and distance to IP, the usage of this position was problematic for three important reasons.

Firstly, this area of the LHCb solid angle had been optimized to have material with as few radiation lengths as possible in order to not interfere too much with the particle physics processes. In order to place the BCM at this position the material budget would need to be minimized to the extreme.

Secondly because of the mentioned material optimization the pipe at this point is made of beryllium. This is a very fragile and expensive material which could easily be

damaged when working on or around it. Mounting a BCM station directly on the pipe would thus constitute a certain danger to the experiment and LHC as a whole.

Finally, as the BCM would have to be mounted between the RICH1 and the TT, the space available would only be a few cm and would only be accessible when the TT was in the open position.

Because of these issues it was decided to place the BCM on a mobile beam support flange at the entrance of the magnet. This component is made of massive aluminum meaning that the addition of a BCM station would only contribute a small fraction to the total material budget in the area.

The position of the flange dictates the z -position of the device, resulting in a distance to IP of 2765 mm. The central radius of the sensors was chosen to be 41 mm in order to keep a certain distance from the beryllium pipe.

6.2.2 Position and Design of the Upstream BCM

Unlike the downstream BCM the positioning of the upstream was a simpler task. The pipe upstream of the VELO has a fixed radius and is covered with a bake-out heating foil at all times. As such the best position available is at the fixed pipe support located at the concrete shield wall upstream of the experiment. This provides a solid mounting point for the device.

Due to the size of the vacuum chamber and the heating foil the sensors of the upstream BCM had to be mounted at a central radius of 54.5 mm. Using the fixed pipe support as mounting means that the z -position of the device is at -2131 mm w.r.t. the IP.

6.3 Simulations for Determining the Beam-Dump Thresholds

In order to determine at which signal level it would be prudent to order the beam to be dumped, the expected nominal signal level has been investigated through the use of simulations.

Nominal running conditions imply that both beams contain 2808 bunches, each having a population of 1.15×10^{11} protons at an energy of 7 TeV. The expected proton-proton interaction rate in the LHCb at these settings is about 15 MHz. With the BCM update rate of 25 kHz, one expects about 600 interactions per update. These settings are used as they represent the harshest radiation conditions expected to exist in a steady state run. Instantaneous radiation at injection can however be higher.

Proton-proton interactions at the IP are simulated in the form of MB events where Pythia is used as the particle generator.

Table 6.2 shows the expected energy deposition and signal value per sensor in the two BCM stations. The signal values are derived from an assumed linear dependence between the energy deposition and the signal. The translation factor of 0.35 nA/MeV is taken from [50].

Table 6.2: Average BCM signal per sensor at nominal conditions. The value is given per 40 μs time slot. The value for a VELO sensor paddle is added for comparison.

Sensor	Energy Deposition (MeV)	Signal (nA)
BCMU	57.7	20.2
BCMD	15.0	5.2
VELO	1100	N/A

These results provide benchmark values to which the BCM beam dump algorithms are tuned. Two beam dump algorithms are used for the BCM, RS0 and RS32 responsible for quick and slow dump, respectively [51].

The RS0 algorithm works as follows:

1. Check if signal level exceeds threshold individually for each sensor
2. Check if condition 1 is met in two succeeding 40 μs time frames
3. If condition 2 is met in at least three adjacent sensors, a beam dump is requested

The RS32 algorithm works as follows:

1. Calculate a running sum over the last 32 40 μs time frames individually for each sensor
2. The sensors with the lowest and the two highest signals are discarded. The rest are summed up
3. Request a beam dump if the sum from condition 2 exceeds the dump threshold.

In order to set a dump level for these algorithms in such a way that the risk of false positives is negligible while at the same time the system provides adequate protection these algorithms have been tested on the nominal data. Figure 6.5 shows the probability of a false positive during nominal run conditions for RS0.

Though a false positive is unlikely even if the threshold is set to twice the nominal signal (200%), it was decided that the level should be 500 times the nominal for RS0 and 100 times the nominal for RS32. The reason for this is that the BCM should not dump the beam unless a danger to the LHCb detector is present. The RS0 threshold has later been modified to 1000 and 1500 times nominal for upstream and downstream, respectively due to increased rates at injection. During tuning and other procedures the signal level could exceed the nominal level, though as long as this stays within reasonable levels it is more prudent to inform the LHC of the adverse conditions rather than dumping the beam outright.

6.4 Simulations for Estimating the Covering Range of the BCM

As the BCM has been created in order to protect the sensitive elements of the LHCb experiment against high radiation levels, it is of interest to investigate the correlations

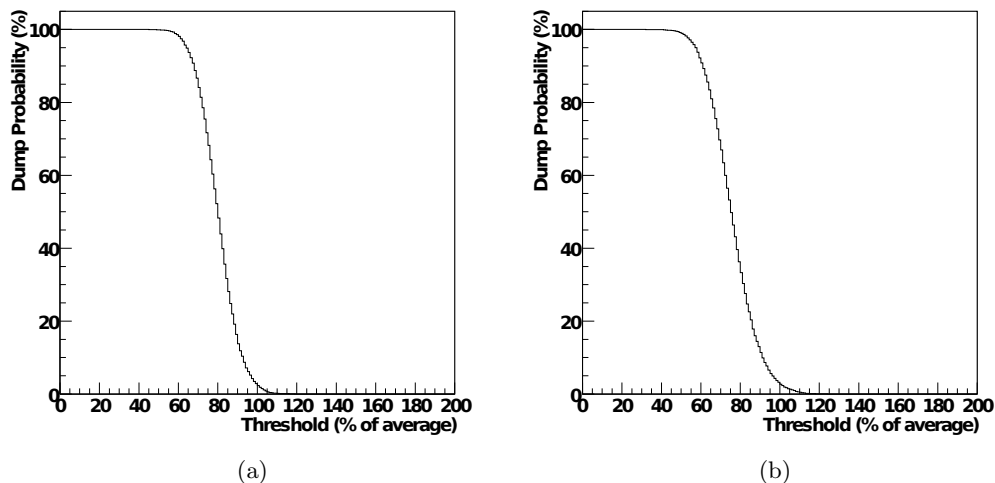


Figure 6.5: Beam dump false positive probability for RS0 algorithm. Figure 6.5(a) and 6.5(b) shows the probability of a beam dump request from the RS0 algorithm for the upstream and downstream BCM station, respectively. The horizontal axis gives the set beam dump threshold level as a percentage of the average beam-beam interaction signal.

between these elements and the BCM. There are two fields of interest to be taken into account when considering this subject. Firstly the correlations between the BCM and the sensitive elements should be investigated during nominal conditions in order to ascertain the relation between the two. Secondly, as adverse beams occur in the form of particles traversing the experiment with wrong angles and position with respect to the expected beam centroid, simulations have been performed where a range of angular and positional particle offsets have been scanned.

6.4.1 Signal correlations between the BCM and sensitive elements at nominal conditions

When it comes to damage from adverse beam conditions the VELO is of the utmost concern. To check the correlation between the VELO and the BCMs the particle gun was used to generate protons in such a way that they would strike an aperture of the experiment and thus cause a detectable particle shower. This represents scenarios where the beam is accompanied by a halo or the beam itself is in an adverse position, causing scraping on the experiment material.

As can be seen from figure 6.6, there is a clear correlation between the BCM and the VELO, however, this test was performed in such a way that it does not take into account the possibility of a particle distribution invisible to one detector or the other. As such also the coverage range of these detectors must be mapped out.

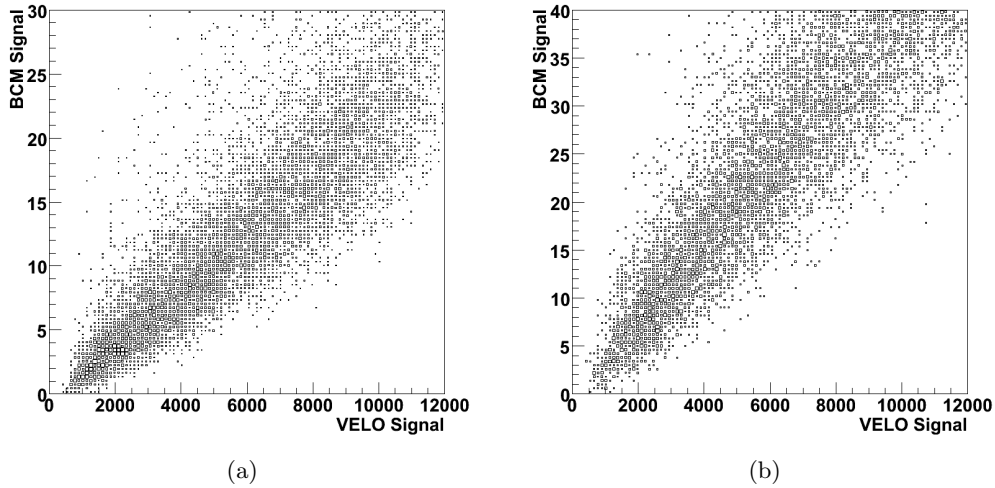


Figure 6.6: Correlations between BCM and VELO. Figure 6.6(a) shows the correlations between the VELO and the downstream BCM for protons from beam 1 interacting with an aperture edge. Figure 6.6(b) shows the same for beam 2 on the upstream BCM station. In order to attain a range of signal values, between 100 and 1000 protons have been used per measurement point.

6.4.2 Estimates of the coverage range of the BCM

In order to ascertain whether the BCM is able to protect a given sensor, the coverage range must be determined. By generating particles at various radii and angles one can check if the sensitive area of the BCM overlaps that of the protected sensor.

450 GeV Local Beam Scraping, VELO Open

During injection the particle energy is limited to 450 GeV. There are two scenarios of interest for this energy level. The first is the injection of a pilot bunch, that is a single “small” bunch with about 5×10^9 protons. In the case of non-ideal machine setup like wrong magnetic field strengths, such a bunch can be lost immediately and completely. Secondly, circulating beams with 450 GeV could attain a non-ideal orbit and thus start scraping on the machine apertures.

In both of these cases the VELO will be in the open position and as such the relevant apertures for this scenario become the pipe section in the TT with a radius of 25 mm and the pipes in the MBXWS and MBXWH magnets with a radius of 26 mm. Because of the low beam energy, the simulated magnetic fields are scaled down accordingly, i.e. they are at 450/7000 of nominal strength. These simulations were performed before data taking commenced. During the actual 2009 450 GeV runs, field strengths of up to 100% were used. Though the validity of the simulations are limited by this, the closeness of the BCM to the VELO and the reduced field strength in the related region keep the results of the scan relevant.

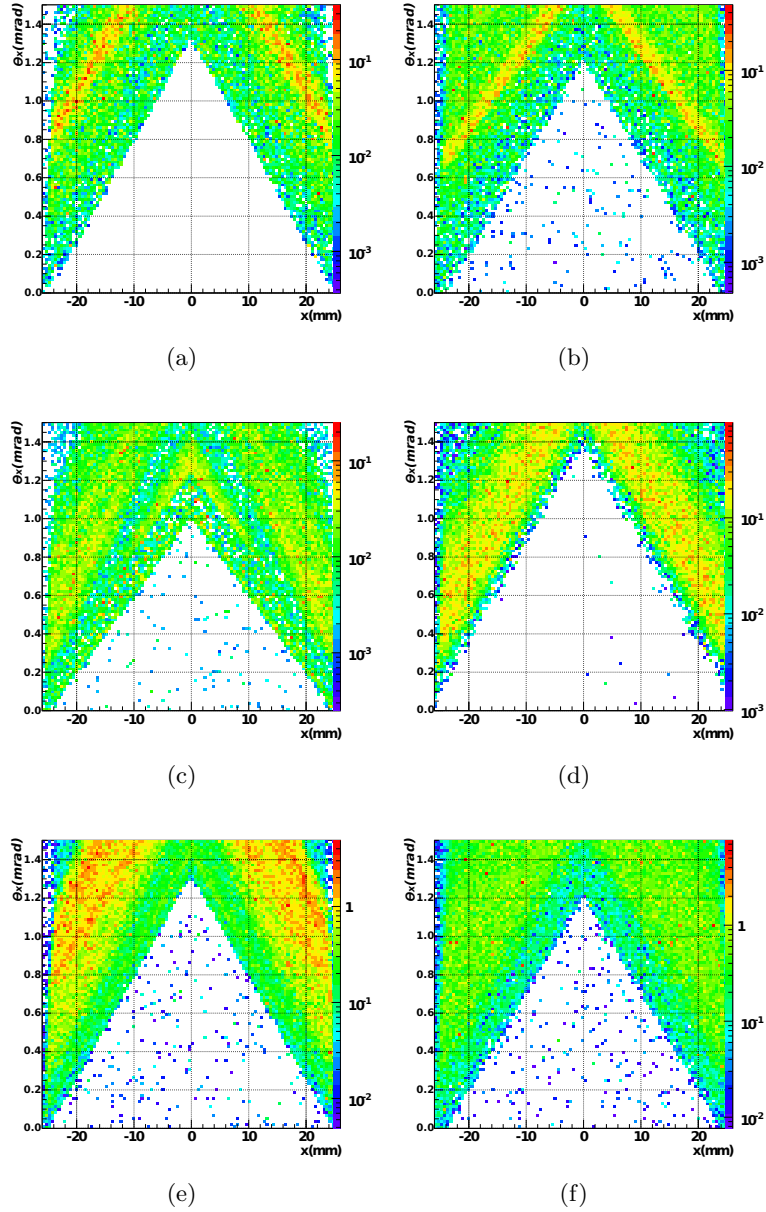


Figure 6.7: Scraping sensitivity in the BCM sensors and VELO paddles from single 450 GeV protons generated at ± 22180 mm from the IP. The horizontal and vertical axis gives the production location and angle of the proton, respectively. The scan is conducted on the LHCb horizontal axis only ($\theta_y = 0$ rad, $y \in [-5, 5]$ mm). The value in each bin is scaled to represent the energy deposition per proton (in MeV) in the relevant detector. The left column is for beam 1, while the right is for beam 2. The three rows give the scan for BCM Up, BCM Down and VELO.

A parameter scan has been performed in order to determine the sensitivity range of the various detectors using 450 GeV protons. The protons are generated at ± 22180 mm from the IP with x varying from -26 mm to +26 mm and θ_x from 0.0 mrad to 1.5 mrad. θ_y is fixed at 0.0 mrad while y is allowed a uniform variation in the range [-5,5] mm to account for possible vertical offset of the beam.

The results are shown in the diagrams in figure 6.7. The size and position of the blind areas are important when interpreting these diagrams. For the purpose of protecting the VELO it is essential that in no parameter range does the VELO attain a signal increase without a corresponding signal increase in the BCM.

In the case of beam 2 the VELO (figure 6.7(f)) and the upstream BCM (figure 6.7(b)) have the same sensitivity range, while for beam 1 the downstream BCM (figure 6.7(c)) is sensitive at a lower parameter range than the VELO (figure 6.7(e)). Thus the BCM is expected to be able to protect the VELO in this scenario.

Table 6.3: 450 GeV beam scraping energy deposition. “E/p+” indicates the average energy deposition (MeV) in the BCM sensors and VELO paddles from single 450 GeV protons generated at ± 22180 mm from the IP incident on the sensitive parameter range of the detector. The variable “% of Nom.” gives the energy deposition per proton as a percentage of the benchmark values (table 6.2).

	BCM Upstream		BCM Downstream		VELO	
	E/p+	% of Nom.	E/p+	% of Nom.	E/p+	% of Nom.
Beam 1	0.0251	0.04%	0.0157	0.1%	0.575	0.05%
Beam 2	0.104	0.2%	0.0306	0.2%	0.423	0.04%

Table 6.3 gives some estimates of the signal values in the different detectors. In the sensitive region, outside the blind area, the energy deposition per proton is measured. This is compared to the expected energy deposition from nominal beam-beam interaction events in order to give an indication of how many particles per 40 μ s would be needed to impend on the sensitive area in order to result in a signal strength comparable with the nominal signal. By combining these numbers with the position of the edge of the sensitive area and a chosen beam distribution one can attain a ballpark estimate of the expected signal levels. An example of this will be shown in the next section.

Beam 1

The figures 6.7(a), 6.7(c) and 6.7(e) show the signal from beam 1 recorded in the upstream BCM, downstream BCM and VELO respectively. With respect to the beam direction the downstream BCM is located behind the aperture restriction in the TT region. This means that it should be sensitive to scraping at this aperture, unlike the VELO and upstream BCM. When considering the relevant plots one can see that the sensitive area of the upstream BCM corresponds to that of the VELO while the downstream BCM is sensitive in tighter parameter range. Thus this BCM station would be able to detect scraping before the VELO experiences significant signal increase. This can be shown quantitatively through considering specific failure scenarios.

Pilot Bunch The set of figures 6.8 gives information about expected signal levels in the case of wrong settings in a dipole corrector magnet (MCBX.1L8) when injecting a pilot bunch for beam 1 [52]. The magnet in question is located at about -30 m from the IP and the scenario involves the magnet having reverse polarity and high power representing a worst case scenario.

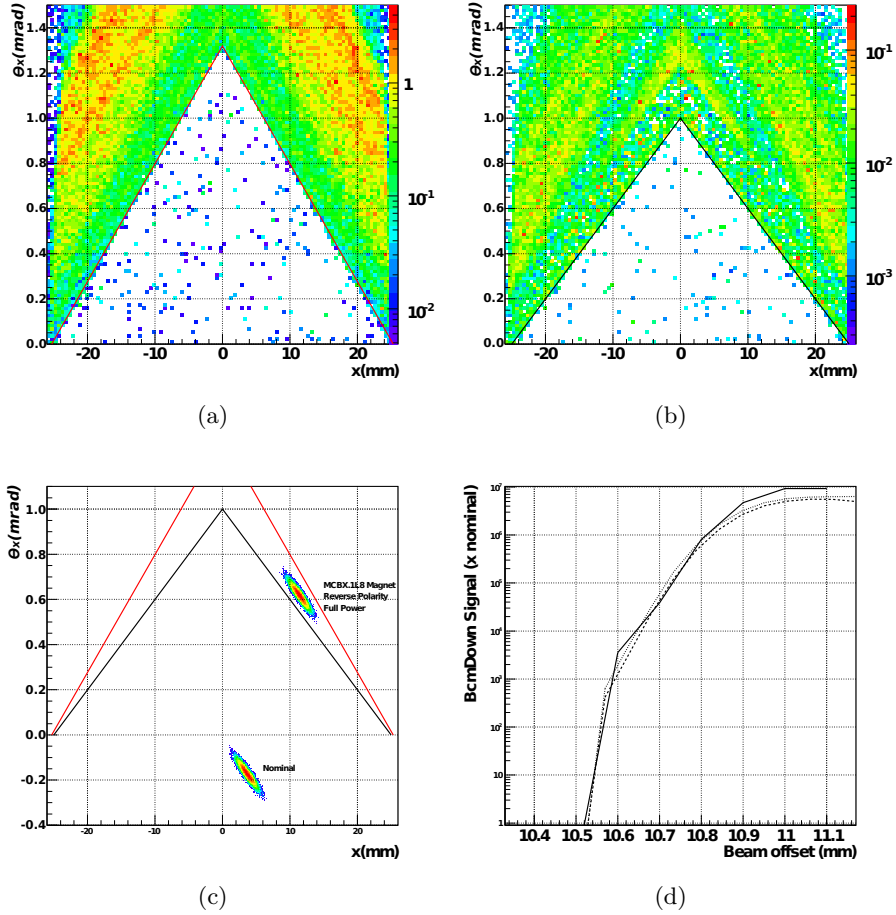


Figure 6.8: Pilot bunch sensitivity. Figure 6.8(a) and 6.8(b) show the 450 GeV beam scan (x vs. θ_x) for the VELO and downstream BCM respectively. The line indicates the edge of the sensitive area. Figure 6.8(c) shows nominal and offset pilot bunches with the sensitivity lines. Figure 6.8(d) shows the signal in the downstream BCM as multiples of the nominal signal versus a beam offset. The solid line represents a full set of simulations for each point. The long dotted line is created through scaling of the sensitivity scan, while for the short dotted line assumes a constant sensitivity.

Figure 6.8(a) and 6.8(b) show the sensitivity scans for the VELO and downstream BCM respectively, where the lower edge of the sensitivity region have been marked with a line. In figure 6.8(c) one can see these same threshold lines together with two

pilot bunches. One pilot bunch represents the nominal case, while the other shows a scenario where the MCBX.1L8 magnet is given reverse polarity and maximum power. One can see that a large signal in the downstream BCM and virtually no signal in the VELO is expected. In this example the nominal bunch would give virtually zero signal in the BCM, while the offset bunch signal would be large.

In order to attain at what magnet setting a beam dump will be triggered, the beam parameters x_0 and θ_{x_0} are varied in a way consistent with changing the field in the MCBX.1L8 magnet. This can be done using three different methods:

- Performing a full simulation of the relevant scenario for a series of beam parameters.
- Scaling the sensitivity scan with a fitting beam distribution (i.e. a bin by bin multiplication of figure 6.8(b) and 6.8(c)).
- Using the values in table 6.3 and assuming that each beam proton crossing the sensitivity range line results in 0.016 MeV energy deposition per downstream BCM sensor.

Figure 6.8(d) compares these three approaches. The full simulations by definition give the most precise result as the exact scenario is generated. However as one can see from the plots the scaling of the sensitivity scan gives a similar result, and even the per proton fixed energy deposition multiplication is consistent with the other results. These graphs are created to indicate the parameter range at which signal is attained in the relevant sensor, and does not represent a precision measurement. Only the downstream BCM station is indicated, as for this failure scenario the VELO signal is always negligible.

Using these results we can assume that any failure scenario where the y_0 and θ_{y_0} beam parameters are kept close to zero, the sensitivity scans can be scaled with a relevant beam distribution in order to get estimates of signal levels in the various detector components.

For the rest of this document the sensitivity scan scaling approach will be used, as it returns a more precise estimate than the simple multiplication without the computational overhead required by the full simulation approach. The precision of the result is however limited by the statistics of the relevant parameter scan plot.

Circulating Beam The pilot bunch is a single shot event, and thus can end up far within the sensitive area. In the case of circulating beams, however, one expects the beam to deteriorate slowly compared to the update rate of the BCM. As such, it is of interest to determine the lowest parameter range in which a beam dump would be requested. Assuming the nominal beam with 1.1×10^{11} protons per bunch, 2808 bunches, revolving at a frequency of 11245 Hz, about 1.4×10^{14} protons per beam pass through LHCb per 40 μ s integration period. Using the scaling of the sensitivity scan one can quickly determine at what parameter range (x_0, θ_{x_0}) one expects a beam dump to be triggered.

Assuming all other beam parameters are fixed at the standard 450 GeV run values and that a beam dump will be requested when the signal exceeds 100 times the nominal

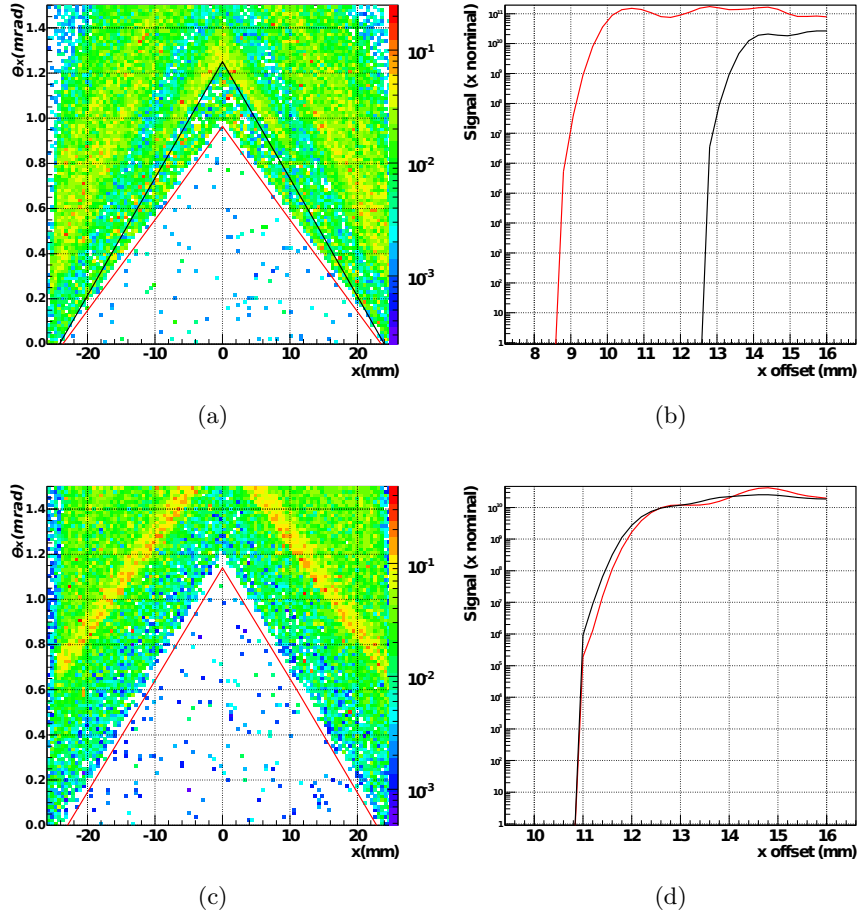


Figure 6.9: Beam dump range for 450 GeV beam energy. The top figures represents beam 1, while lower are for beam 2. In figure 6.9(a) and 6.9(c) the red line indicates the central x_0 and θ_{x_0} parameter of a full 450 GeV beam expected to cause a beam dump in the downstream and upstream BCM respectively. The black line indicates at what point the VELO will receive a signal 100 times higher than the nominal beam-beam interaction event signal. For beam 2, these lines overlap. Figure 6.9(b) and 6.9(d) show a profile of the signal in the BCM (red) and VELO (black) as multiples of the nominal signal. The plot represents a scan in x_0 offset at a beam angle (θ_{x_0}) of 0.6 mrad.

signal (original RS32 [51]), the dump threshold will be equal to the red line in figure 6.9(a). That is, any beam with a centroid x_0 and θ_{x_0} above this line is expected to cause a beam dump. Figure 6.9(b) shows an example of signal increase in the BCM and VELO when the beam is moved towards the aperture restriction. In this example θ_{x_0} is set to 0.6 mrad and x_0 is varied. One can see that the BCM signal rises steeply when the beam gets close to the related sensitive region. If the beam conditions decay relatively slowly a beam dump can then be ordered before any increased signal is detected in the VELO.

Beam 2

For beam 2 (figure 6.7(b), 6.7(d) and 6.7(f)) the aperture situation is opposite to that of beam 1. One can see that the downstream BCM has a worse sensitivity range than the upstream BCM and the VELO. This means that there is a certain parameter space where the downstream BCM will not be able to protect the VELO. The upstream BCM however covers the same parameter space as the VELO and thus will be able to register any increased signal levels.

Assuming a full 450 GeV beam equivalent to the one investigated for beam 1, a dump range scan has been conducted. The result is plotted in figure 6.9(c). As the sensitivity range of the upstream BCM and the VELO is equal, their signal strengths from a given beam show similar behavior. Figure 6.9(d) gives an example of this. It depicts the signal in the two devices as multiples of the nominal value when performing a beam offset scan with constant beam angle. The lines in question overlap to a large degree.

One can conclude from this that in the case of adverse beam the upstream BCM will be able to take action. However, the VELO is expected to have a signal level behavior similar to the BCM thus exposing it to the increased radiation in the period leading up to the beam dump.

6.4.3 7 TeV Local Beam Scraping, VELO Closed

At design operation the beam protons will reach a maximum energy of 7 TeV. When stable beam-beam collisions have been established, the VELO is moved in towards the IP, thus forming the limiting aperture limit within LHCb. This scenario describes the sensitivity to beams scraping on the RF-Foil with the VELO in the central closed position.

As in the previous simulations, the protons are generated 22180 mm from the IP. However, because of the aperture limitation introduced by the VELO the parameter ranges have been reduced; $x \in [-7, 7]$ mm, $y \in [-1, 1]$ mm, $\theta_x = [0.0, 0.4]$ mrad and $\theta_y = 0.0$ mrad.

Table 6.4: 7 TeV beam scraping energy deposition. “E/p+” indicates the average energy deposition (MeV) in the BCM sensors and VELO paddles from single 7 TeV protons generated at ± 22180 mm from the IP incident on the sensitive parameter range of the detector. The variable “% of Nom.” gives the energy deposition per proton as a percentage of the benchmark values (table 6.2).

	BCM Upstream		BCM Downstream		VELO	
	E/p+	% of Nom	E/p+	% of Nom	E/p+	% of Nom
Beam 1	N/A	N/A	0.026	0.2%	0.62	0.06%
Beam 2	0.020	0.03%	N/A	N/A	1.39	0.1%

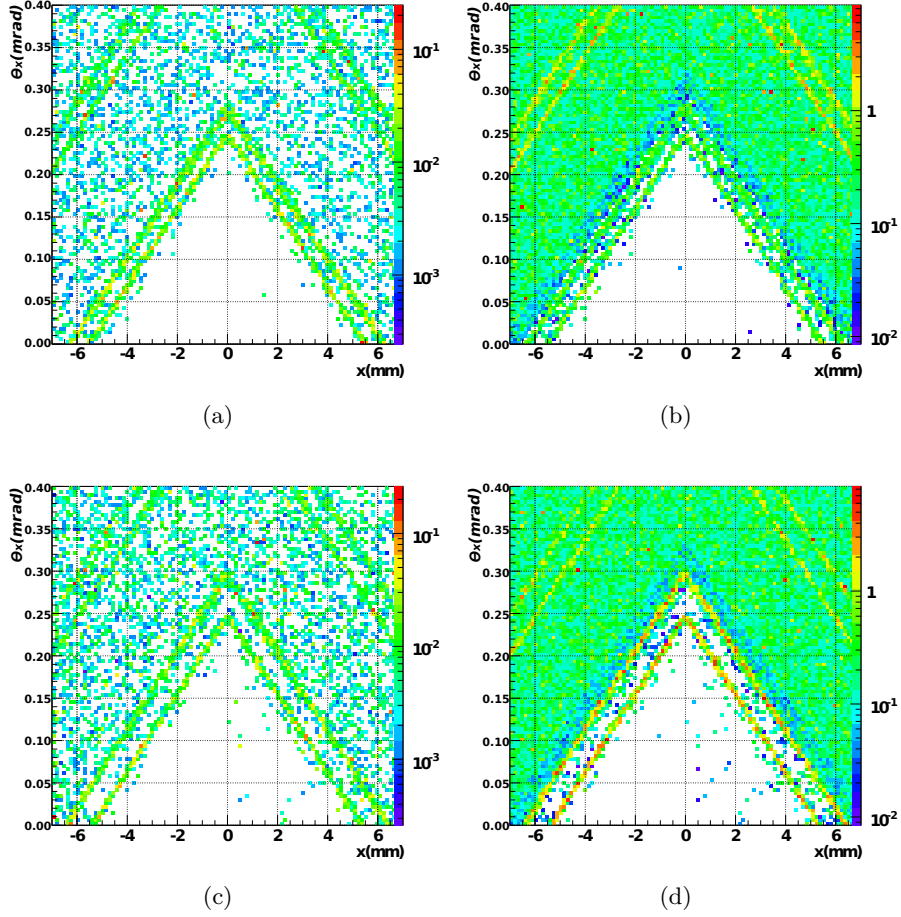


Figure 6.10: Scraping sensitivity in the BCM sensors and VELO paddles from single 7 TeV protons generated at ± 22180 mm from the IP. The horizontal and vertical axis gives the production location and angle of the proton, respectively. The scan is conducted on the LHCb horizontal axis only ($\theta_y = 0$ rad, $y \in [-1, 1]$ mm). The value in each bin is scaled to represent the energy deposition per proton (in MeV) in the relevant detector.

Beam 1

Figure 6.10(a) and 6.10(b) show the sensitivity region of the relevant detectors for beam 1. The upstream BCM is completely insensitive to scraping in the RF-Foil as this aperture is located downstream of the sensors. The downstream BCM, however, has a sensitivity range equivalent to that of the VELO.

As mentioned for the 450 GeV scenario, a full machine has 2808 bunches with 1.1×10^{11} protons per bunch, revolving at a frequency of 11245 Hz, thus per 40 μ s period about 1.4×10^{14} protons per beam pass through LHCb. Using the appropriate beam parameters the beam dump range has been investigated.

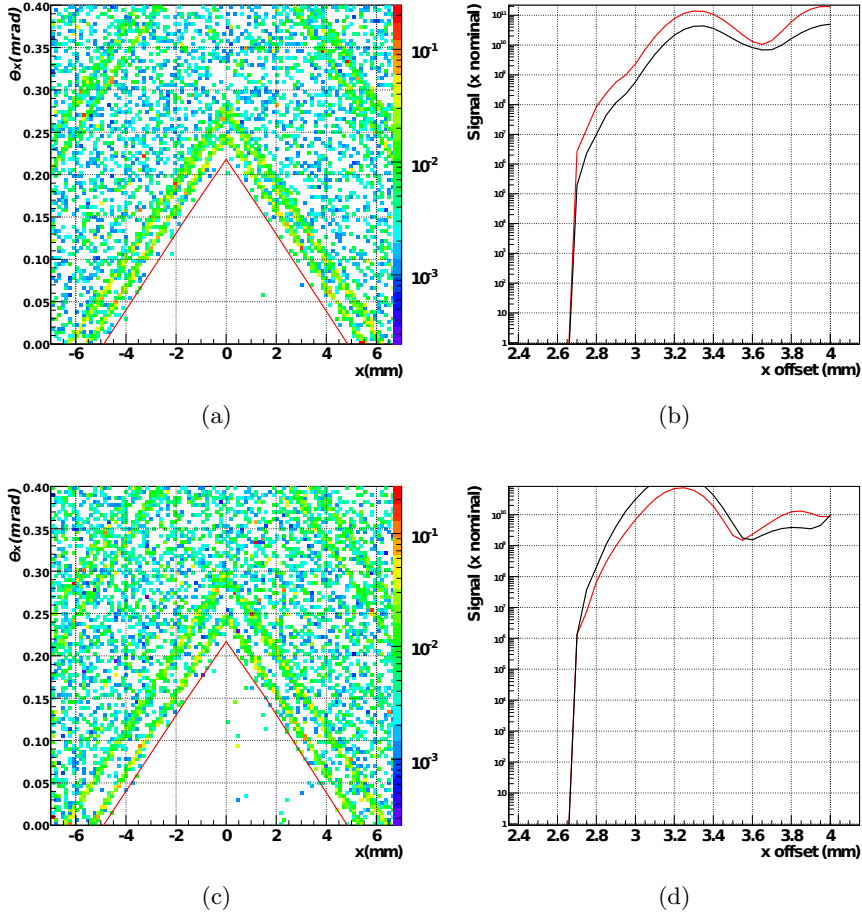


Figure 6.11: Beam dump range for 7 TeV beam energy. The top figures represent beam 1, while the lower are for beam 2. In figure 6.11(a) and 6.11(c) the red line indicates the central x_0 and θ_{x_0} parameter of a full 7 TeV beam expected to reach the beam dump level in the downstream and upstream BCM respectively. Figure 6.11(b) and 6.11(d) show a profile of the signal in the BCM (red) and VELO (black) as multiples of the nominal signal. The plot shows a scan in x_0 offset at a beam angle (θ_{x_0}) of 0.1 mrad.

From figure 6.11(b) one can see that the signal in the VELO and the downstream BCM behaves very similarly, and that any beam scraping would result in a signal increase in both devices. As such only one sensitivity line is indicated in figure 6.11(a). For a full 7 TeV beam with standard parameters any variations in the x_0 and θ_{x_0} parameter exceeding the red line is expected to cause a beam dump in the downstream BCM.

In the same way as for beam 2 450 GeV scenario, due to the overlapping sensitivity areas the VELO is expected to experience the same order of signal increase as the BCM

when scraping occurs.

Beam 2

Beam 2 scraping sensitivity is shown in figure 6.10(c) and 6.10(d). Intuitively only the BCM located after the RF-Foil with respect to the beam direction is sensitive in the same range as the VELO. Thus for beam 2 the upstream BCM can provide protection.

Due to the overlapping sensitivity regions of the VELO and the BCM, the expected signal strength in the two devices is expected to have similar variations. As can be seen in figure 6.11(c), this is a reasonable assumption. Figure 6.11(d) displays the beam dump limit for beam 2. Its behavior is in all respects similar to that of beam 1.

6.5 Status of the BCM at LHCb

The BCM stations are currently installed at the LHCb experiment and are performing according to the expectations as can be seen from figure 6.12. The system has ordered the beam to be dumped multiple times, each time with a valid reason. As such the beam dump thresholds chosen have been proven to be well suited. No false positives have been occurred resulting in unprovoked beam dump, while at the same time the BCM has reacted to adverse conditions with the appropriate action.

The positioning of the device close to and on each side of the smallest aperture of the experiment enables the full protection of the detectors in all considered scenarios, from remote particle showers to scraping on the RF-foil. This has been shown through the usage of extensive simulations. The BCM specific algorithms, custom particle generators and extensions of the standard detector description, including magnetic fields, has been developed and included in the LHCb software suit, available to the whole collaboration.

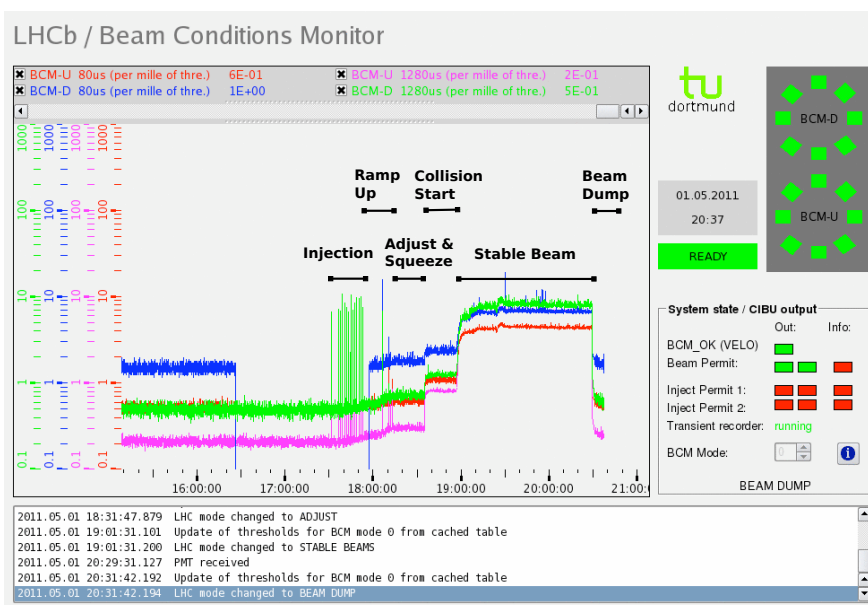


Figure 6.12: BCM online monitoring page. The graphs show the BCM signal levels as a per mille of the threshold level. Red and blue curves show the RS0 value for the upstream and downstream station, respectively. Pink and green are the equivalent for RS32. The various phases of the run are displayed; injection, energy ramping, beam adjustment and squeezing, start of collisions, stable beam and beam dump. The abrupt jumps in signal before and after stable beam are caused by changes in BCM thresholds.

Chapter 7

Inclusive ϕ Trigger

The second step of the high level trigger, HLT2, aims to reconstruct and select physics events in much the same way as physics analysis. Taking the information provided from the various detectors, particle track candidates are reconstructed. Depending on the characteristics of these tracks, they are in turn transformed into specific particle candidates. By combining these particles, taking their measured physical properties into account, decay chains can be reconstructed. A complete and non-ambiguous decay chain is referred to as an exclusive selection, while a partial or generic chain is called inclusive.

Because of computing resource limitations at the online computing farm, the tracking algorithms used are less efficient than the corresponding offline versions. Simulations show that only 96.6% of the tracks that are found offline are also reconstructed in the HLT [53]. For a four prong decay this results in an expected efficiency of 87.1% just due to this effect.

Several interesting decay channels contain a ϕ meson as a daughter particle. It can be envisaged that instead of reconstructing the complete decay chain one could trigger inclusively on this ϕ , thus only requiring the two kaon tracks from the decay $\phi \rightarrow K^+K^-$ to be found. The expected tracking efficiency for such a scheme is 93.3% for channels containing a single ϕ .

At TU Dortmund investigations are being conducted into the decay $B_s \rightarrow \phi\phi$ [5] as well as inclusive ϕ production [54]. An inclusive ϕ trigger line provides an efficient selection for events relevant to these analyses, binding in well with the work performed by the TU Dortmund LHCb group.

The main argument against the viability of such a trigger is the difficulty in separating between kaons and pions. As an average LHCb event at 7 TeV is expected to contain about 25 pions and 5 kaons, the pions have to be suppressed in order to attain a reasonable selection rate and efficiency. The two LHCb Ring Imaging Cherenkov (RICH) detectors (see section 3.5.2) have been designed for this task. According to simulations the average kaon identification efficiency of these detectors is about 89.5% with a corresponding pion misidentification of 1.6% [55], thus providing an excellent particle separation. Though computationally demanding, by using simplified algorithms on a

subset of the HLT2 events it is possible to use this detector component in the online environment. Earlier studies into this subject are documented in [56] and [57].

As mentioned, the RICH algorithms can only be applied to a subset of events. To this effect, the inclusive ϕ trigger has been split into three levels; robust, track fitted and RICH. These will be covered in section 7.4, 7.5 and 7.6, respectively. The inclusive ϕ line has been assigned a 200 Hz output rate limit. As the ultimate HLT2 input rate is 30 kHz, the line needs to have a reduction factor of 150.

In section 7.7 the addition of sidebands will be discussed while section 7.8 considers the timing issues of the trigger line. Finally in section 7.9 an alternative set of selections is presented giving various reduction factors without the use of the robust step.

7.1 The RICH Algorithms

As the generation of the RICH information can be slow (in the order of seconds per event), it has been envisaged that it will only be available for offline analysis. However “fast” algorithms have been developed which could run online [58].

The RICH reconstruction consists of two steps; track and ring projection, and likelihood optimization.

7.1.1 Track and Ring Projection

As can be seen from figure 7.1 due to the circular form of the mirrors, photons created along the path of a charged particle track are reflected back to a circular shape with a fixed radius, independently of their point of generation. These photons are registered by hybrid photon detectors, resulting in an image similar to figure 7.1.

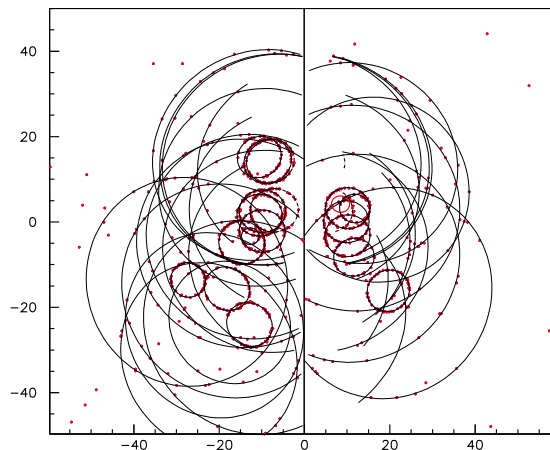


Figure 7.1: RICH photons and reconstructed rings. Individual photon hits are combined into rings related to the Cherenkov angle of the traversing particle. [22]

Misalignment as well as the design of the detector result in distortion of the rings. An adjustment is made to the data to compensate for such effects, resulting in circular

rings. The projections of the reconstructed particle tracks are superimposed on the photon ring map, as if they had been reflected by the mirror. The ideal result is thus a set of track points acting as center of photon rings. The radius of the rings is a measure of the angle of the projected Cherenkov light.

7.1.2 Likelihood Optimization

Each track has a measured momentum. If the radius of the Cherenkov photon ring, and thus the Cherenkov angle, is known, a particle velocity can be calculated from equation 3.7. Combining the momentum and velocity gives a mass hypothesis for the traversing particle.

In the RICH algorithm, the inverse calculation is utilized. Each track is given a pion mass hypothesis and thus an expected Cherenkov photon ring radius according to the measured momentum. A global likelihood is calculated for this configuration, taking the density of photons in the vicinity of the projected rings into account. Each track is tested with another mass hypothesis, giving a change in likelihood. The combination that gives the largest increase in the overall likelihood is tagged with the new hypothesis. This is repeated until no further increase is possible. While the offline algorithm investigates five particle hypotheses (e^\pm , μ^\pm , π^\pm , K^\pm and p^\pm), the online algorithm uses a simplified procedure with only pions and kaons. The aim is to create an optimized particle combination by varying the particle species of each track until the overall global likelihood is maximized.

The offline algorithm has a computing time in the order of seconds, the average global online speed is of the order of 10 ms. However, the computing time of the algorithm has a strong dependence on the number of tracks in the event.

The particle ID value (PID) is calculated in the form of a *delta log likelihood* ($\Delta \log \mathcal{L}_{x-y}$) between the two mass hypothesis x and y . This value is calculated as the logarithm of the likelihood value in the case of the relevant track having mass hypothesis x subtracted by the equivalent with mass hypothesis y . All other tracks have the particle species as defined by the optimization. Resultingly if for example $\Delta \log \mathcal{L}_{x-y}$ is positive, the x particle hypothesis is considered more likely than y for the relevant track. One can thus cut on this value to separate between various particle species hypotheses.

7.2 Relevant Physics Channels

Initial studies were performed on the decay $B_s \rightarrow \phi\phi$ due to the high efficiency expected by the existence of two ϕ mesons. The event could thus be selected on both daughter particles of the decay.

As the selection is an inclusive one, the goal is to select all types of events where a ϕ is the result of a B -decay. Several of the key physics channels display this characteristics. Most known is the “golden” channel $B_s \rightarrow J/\psi\phi$. In addition to an exclusive trigger, this channel is effectively triggered on the di-muon line, looking for the decay $J/\psi \rightarrow \mu\mu$. With the inclusive ϕ trigger acting on the other daughter, this provides a double-check.

Further channels investigated are $B_s \rightarrow \phi\gamma$ and $B_s \rightarrow D_s\pi$ where D_s decays to ϕ with a branching fraction of about 16%. Other channels have been briefly checked, however, as they are not part of the core channels they will not be shown in this document.

7.3 Efficiency Determination

In order to set limits on the cuts, efficiency plots are used. These show the fraction of events retained (selection efficiency) after applying a certain cut, versus the output rate of the trigger. This is done individually for each physics channel investigated.

In order to measure the trigger rate, the HLT group has created a “triggered background sample”. This contains standard minimum bias events that have successfully survived the L0 and HLT1 trigger decisions, thus appearing similar to the expected input data.

For the signal samples, the least biased approach would be to repeat the above procedure with those samples. This would allow the fraction of events produced that survive the trigger to be used in the optimization. However, the trigger is created to provide the physics groups with the data they desire, and thus another approach has been used by the HLT group.

The signal samples are not passed directly to the trigger, but are rather run through the offline reconstruction. Only events that are selected by their related physics channel preselection are kept. These are thus the events that are considered “useful” to the related analysis, having the relevant characteristics for the measurement. The subsample is passed through L0 and HLT1, and the surviving events give the basis for efficiency calculations.

Optimization on HLT2 thus aims to select a high fraction of signal events that have already been deemed of interest for the various physics analysis groups. As a result, the various channels can not be directly compared to each other as the preselections vary. However, the resulting selection is more likely to be appropriate for the related physics analysis.

The following procedures have been performed on the DC06 simulated data samples.

7.4 Cuts on Robust Tracks for the Inclusive ϕ Trigger

The HLT2 has all detector information available, in particular the various particle hits. Tracks are created by combining hits from the detectors in a way consistent with a traversing particle. This can, however, be a time consuming process as the combinatorics and fitting of the tracks is computationally resource demanding.

HLT thus uses a simplified tracking algorithms, creating *robust* tracks. These tracks are created by combining particle hits and projecting the track from detector to detector. To reduce time consumption the magnetic fields is parametrized, giving the track an abrupt kink, and no track fitting procedure is used. As a result the tracks are rather rough approximations to reality thus the measured kinematic parameters have higher errors than the fitted tracks.

The tracks are turned into particle candidates, which in turn can be combined to form constellations relevant to a certain particle decay. For the inclusive ϕ trigger charged kaon candidates are combined to form ϕ mesons. Cuts on the kaons are performed first. Only those who survive this step are eligible to be combined into ϕ mesons, and thus be exposed to the related cuts.

Due to the tracking procedure used for the robust tracks, the error based cut variables are not trusted. As such all cuts are performed on the more explicit properties of the selection. Five variables are used at the robust step; kaon impact parameter, kaon transverse momentum, distance of closest approach between the kaon tracks, ϕ measured mass and ϕ transverse momentum.

7.4.1 Kaon Impact Parameter

The kaon impact parameter is the tracks distance of closest approach to the primary vertex (PV). This variable is used to separate between prompt ϕ and those arriving from the decay of a b-meson. Prompt particles are those who originate directly from the proton-proton interaction, or PV. The kaons from prompt ϕ would, due to the short lifetime of the ϕ , point towards the PV. By demanding a minimum impact parameter, the fraction of prompt ϕ can be reduced.

7.4.2 Kaon Transverse Momentum

A signature of a b-meson decay is a comparatively high transverse momentum (p_T) of the daughter particles. Thus kaons arriving from such a decay should display this behavior. The additional transverse momentum from the decay $\phi \rightarrow K^+K^-$ is small as the mass difference between a single ϕ meson and two kaons is low. Like the impact parameter, p_T reduces the amount of prompt ϕ , as kaons from the decay of these particles would be expected to have a lower transverse momentum.

7.4.3 Kaon Distance of Closest Approach

The two kaons arriving from a ϕ meson decay necessarily arrive from the same point in space. A measure of this is the kaon distance of closest approach (DOCA). As the name indicates, this variable gives a measure of the minimal distance between the two kaon tracks along their path.

The assumption is that the ϕ decayed close to the area where DOCA occurs, thus the value represents a vertexing criterion. Kaons that are not related to each other should on average have a higher DOCA as they do not originate from the same point.

7.4.4 ϕ Measured Mass

The measured kinematic properties of the kaon candidates are combined to build the ϕ candidate in order to determine the mass of the combination. If the combination is correct, and thus the kaons are daughters of a ϕ decay, the measured mass should be close to the PDG value for a ϕ meson. A mass window cut (upper and lower) can

be applied to the ϕ candidate in order to remove kaon combinations that result in the wrong mass. This cut reduces the amount of events where two non-related kaons are combined.

7.4.5 ϕ Transverse Momentum

In the same way as for the kaons, the ϕ transverse momentum is an indicator as to whether the meson arrives directly from the interaction point, or from a b -decay. ϕ mesons with a certain minimal p_T are kept. A cut on the transverse momentum of both the kaons and the ϕ meson is performed in order to reduce combinatorics.

7.4.6 Cut Optimization

As mentioned the maximal HLT2 input rate is 30 kHz. Due to timing issues only a fraction of these events can pass through the track fitting procedure. The robust inclusive ϕ trigger level thus has to select such a subset. An output rate of 1 to 2 kHz has been deemed appropriate as a compromise between trigger efficiency and subset size. For the transverse momentum, only that of the ϕ is considered. The kaon transverse momentum is chosen so that it does not affect the efficiencies and rates, but rather reduces the combinatorics.

By tweaking the cut parameters, a selection of robust cuts is attained. These are not objectively the most efficient cuts attainable, but rather a set of selections created in dialog with the various physics groups. In general the physics analyses also need data from outside the signal parameter range in order to investigate and account for the various components contained in the selection, for example combinatorial background.

Due to correlations between the cut variables, the optimization is an iterative process. A set of starting cuts are selected. Each cut variable is varied individually, keeping the others fixed in order to attain the rate and efficiency change. The cuts are adjusted to increase efficiency while keeping the rate stable, and the process is repeated. The optimization is performed using an optimization script, though with human intervention to account for the wishes of the physics groups.

Table 7.1 shows the cuts attained from this process while the efficiencies are listed in table 7.2. The efficiency plots are shown in figure 7.2. One cut variable is scanned while all other parameters are kept at the selected values. The figures thus displays the change in efficiency and rate when varying this cut.

Table 7.1: Robust cut values.

Variable	Cut value
Kaon Imp. Par.	> 0.05 mm
Kaon P_T	> 800 MeV/ c
Kaon DOCA	< 0.2 mm
ϕ Mass Win.	± 12 MeV/ c^2
ϕ P_T	> 1.8 GeV/ c

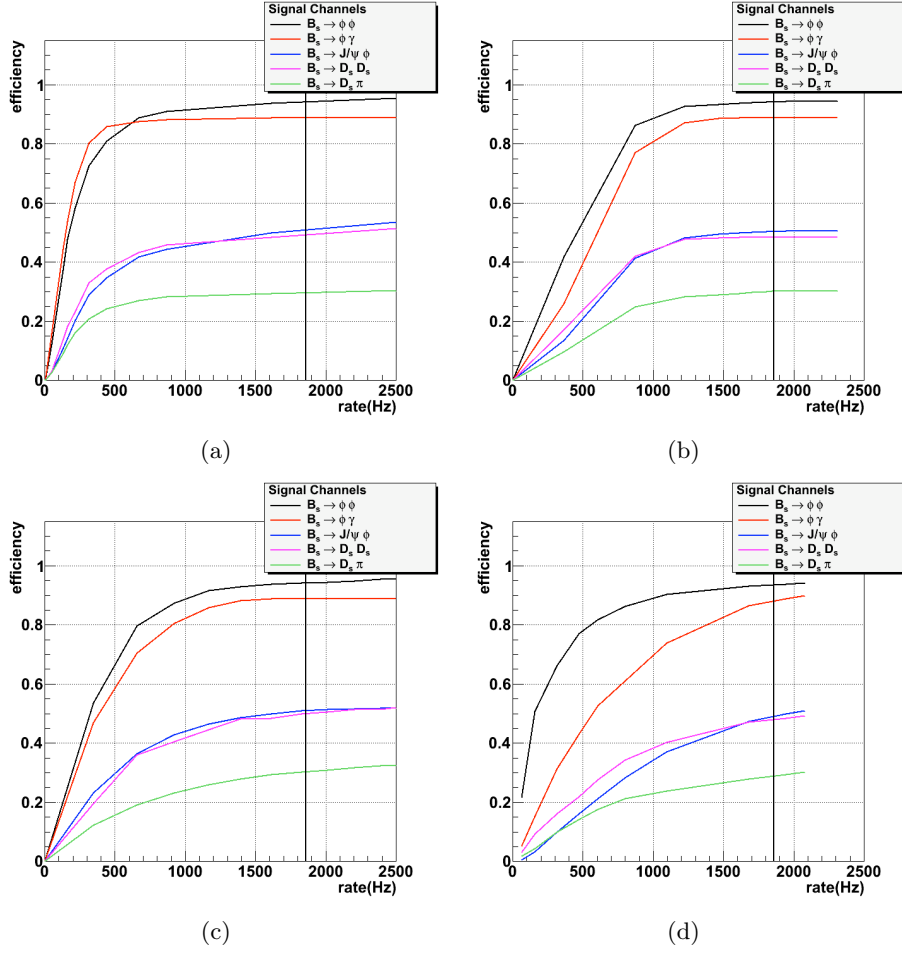


Figure 7.2: Robust cut efficiency plots. The plots show the selection efficiency versus trigger rate for a given signal sample as the cut variable is varied. The vertical line indicates the cut value chosen. All cuts except the one investigated are kept constant in the plots. Figure 7.2(a), 7.2(b), 7.2(c) and 7.2(d) show variations on Kaon impact parameter, ϕ DOCA, ϕ mass and ϕP_T respectively.

Table 7.2: Robust cut efficiencies for various signal channels.

Channel	Efficiency
$B_s \rightarrow \phi\phi$	95%
$B_s \rightarrow \phi\gamma$	89%
$B_s \rightarrow D_s\pi$	30%
$B_s \rightarrow J/\psi\phi$	53%
$B_s \rightarrow D_s D_s$	49%

The variations in the selection efficiencies are partially an effect of the efficiency

measurement method. $B_s \rightarrow \phi\phi$ has a high efficiency because of the existence of two ϕ mesons, giving the possibility to trigger on either. The efficiency of $B_s \rightarrow D_s\pi$ and $B_s \rightarrow D_sD_s$ is low because D_s only partially decays to ϕ . If at least one D_s is forced to decay to a ϕ , the efficiency goes up to 75%. For $B_s \rightarrow J/\psi\phi$ one would expect more or less the same efficiency as for $B_s \rightarrow \phi\gamma$, as both contain a single ϕ . However, the most efficient L0 and HLT1 trigger for $B_s \rightarrow J/\psi\phi$ is the muon trigger, reacting on the decay of the J/ψ -meson. In those events the reconstructability of the ϕ is lower than in the events where the hadronic HLT1 trigger was fired.

The estimated output rate of the robust trigger is 1.9 kHz at nominal conditions.

7.5 Cuts on Fitted Tracks for the Inclusive ϕ Trigger

The events having survived the robust cuts are passed through the track fitting procedure. This is a single pass Kalman fit with simplified detector geometry [59, 60], improving the precision and reducing the error of the tracks. This procedure is somewhat time consuming and must thus be performed on a subset of events and not the full 30 kHz. This procedure is not uniquely used by the inclusive ϕ trigger, but is also called by several other trigger lines. The fit is performed if one or more trigger lines request it.

Two new parameters are used at the track fitted trigger step; kaon impact parameter significance and ϕ vertex χ^2 .

7.5.1 Kaon Impact Parameter Significance

The kaon impact parameter significance is the error based version of the impact parameter. Instead of measuring the distance between the PV and the track in millimeter, it is measured in standard deviations based on the error of the track and PV fit.

A track with a small error which is demanded to keep a distance of at least one standard deviation from the primary vertex thus can physically pass closer to it than one with a large error. In general the variable defines the confidence in the tracks separation from the PV.

7.5.2 ϕ Vertex χ^2

Like the above mentioned variable the ϕ vertex χ^2 has a robust cut equivalent, namely the DOCA. Instead of measuring the minimum distance between the tracks, they are combined into a vertex and the error of this vertex is calculated. A combination of tracks with a low error that pass in close vicinity to each other get a low χ^2 . Tracks with high errors and/or pass each other at a large distance get a higher χ^2 . Only vertices with a value below a given threshold are kept.

7.5.3 Cut Optimization

As this is the second step of the optimization, the efficiencies are based on the events having already survived the robust step, i.e. if all events from the robust step survive, the efficiency is 100%. Figure 7.3 shows the efficiency plots for these two parameters. In the same way as for the robust cuts, the cut values have been determined in communication with the physics working groups.

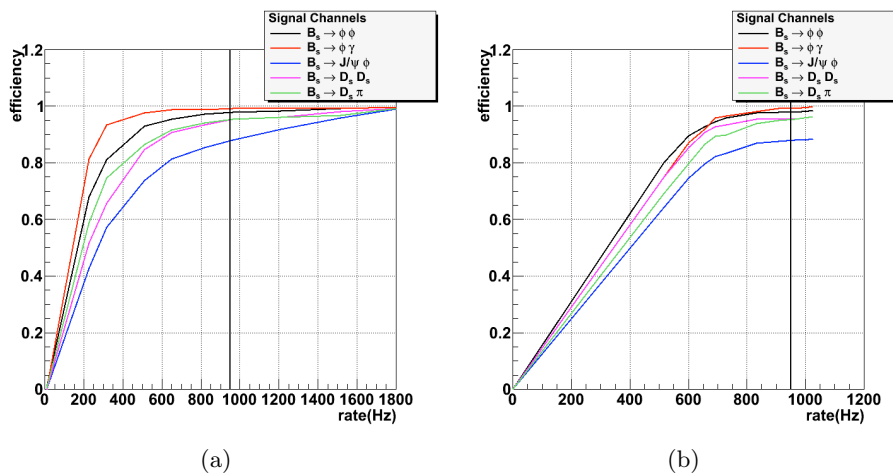


Figure 7.3: Track fitted cut efficiency plots. The plots show the selection efficiency versus trigger rate for a given signal sample as the cut variable is varied. The vertical line indicates the cut value chosen. Figure 7.3(a) and 7.3(b) show variations on Kaon impact parameter significance and ϕ vertex χ^2 respectively.

Cuts on mass and momentum are also re-applied at this step, though they have a limited effect, and are there mainly for completeness. Table 7.3 show the cut values applied at the track fitted trigger step while table 7.4 show the resulting efficiencies.

Table 7.3: Track fitted cut values.

Variable	Cut value
Kaon Imp. Par. Sig.	$> \sqrt{6} \sigma$
ϕ Vertex χ^2	< 20
ϕ Mass Win.	$\pm 12 \text{ MeV}/c^2$
ϕP_T	$> 1.8 \text{ GeV}/c$

With an input rate of 1.9 kHz, the track fitted trigger step has an output rate of about 940 Hz, i.e. a reduction factor of about 2.

Table 7.4: Track fitted cut efficiencies for various signal channels.

Channel	Efficiency
$B_s \rightarrow \phi\phi$	98%
$B_s \rightarrow \phi\gamma$	99%
$B_s \rightarrow D_s\pi$	95%
$B_s \rightarrow J/\psi\phi$	88%
$B_s \rightarrow D_s D_s$	95%

7.6 Cuts on RICH Information for the Inclusive ϕ Trigger

The last step of the inclusive ϕ trigger involves the application of the RICH data in order to separate kaons from pions. Through the rate reduction from the two preceding steps (factor 30), the computing time involved in generating the RICH PID data on the surviving events is acceptable. The generation of this variable is explained in section 7.1.

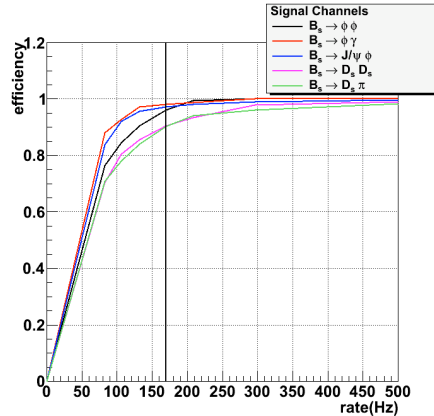


Figure 7.4: RICH cut efficiency plots. The plots show the selection efficiency versus trigger rate for a given signal sample as the cut variable is varied. The vertical line indicates the cut value chosen.

Figure 7.4 shows the efficiency of the RICH PID cut, where this cut represents the value $\Delta \log \mathcal{L}_{x-y}$. As can be seen, this is a powerful cut, reducing the rate by a factor 5 with very little efficiency loss. The final expected output rate is thus about 200 Hz, with a total reduction factor of 150.

Combining the efficiencies of the various steps, table 7.6 gives the overall selection efficiencies. As can be seen, it is possible to attain an inclusive ϕ trigger with a sufficient reduction rate and an acceptable efficiency on the relevant channels.

Table 7.5: RICH cut efficiencies for various signal channels.

Channel	Efficiency
$B_s \rightarrow \phi\phi$	96%
$B_s \rightarrow \phi\gamma$	98%
$B_s \rightarrow D_s\pi$	90%
$B_s \rightarrow J/\psi\phi$	97%
$B_s \rightarrow D_sD_s$	89%

Table 7.6: Overall Inclusive ϕ Cut Efficiencies

Channel	Robust	Fitted	RICH	Full
$B_s \rightarrow \phi\phi$	95%	98%	96%	89%
$B_s \rightarrow \phi\gamma$	89%	99%	98%	84%
$B_s \rightarrow D_s\pi$	30%	95%	90%	25%
$B_s \rightarrow J/\psi\phi$	53%	88%	97%	46%
$B_s \rightarrow D_sD_s$	49%	95%	89%	41%

7.7 Sidebands

In addition to the normal three stage line, a separate scaled line runs with a mass window of $30 \text{ MeV}/c^2$. All other settings are kept equal to the normal line, though the increased rate caused by the loosening of this variable is compensated for by a pre-scaling factor thus only considering a fraction of the overall event sample. The shape of the distribution away from the central signal mass peak can be used to understand the underlying background, and is thus needed by a variety of physics analyses. The value of $30 \text{ MeV}/c^2$ is chosen in cooperation with the physics groups.

Furthermore, a pre-scaled version of the various steps of the line is saved. Specifically, this means the robust step and the kalman fitted step without RICH. This assures that future investigations into the effects of the three staged approach can be investigated. The pre-scaling factors are chosen in such a way that the resulting output rate is about 5-10% of the inclusive ϕ rate.

7.8 Timing Issues

As previously mentioned, both the track fitting and RICH algorithms are comparatively slow. Though the track fitting is used by multiple trigger lines, the RICH is only used by inclusive ϕ . Determining the amount of computing time consumed by the line is important when considering its viability. A high efficiency is useless if the trigger is too slow to be run.

Measurements on simulated minimum bias events show that the generation of the RICH data consumes a time roughly equivalent to the time needed for the robust

reconstruction. If it was applied to all events, it would thus double the computing time. As a reduction factor of 30 is used for the robust and tracks fitted steps, the increase is rather of the order of 3-4%. For an inclusive line, capable of triggering on several different physics channels, this can be considered an acceptable number.

Furthermore, work is being invested at TU-Dortmund in the improvement of the HLT framework [61], aiming to reduce the overall resource consumption of the application. This will affect all parts of the trigger and thus enable more efficient selection algorithms for the same amount of computing power.

7.9 Alternative Settings

In addition to the aforementioned setup, a set of alternative lines has been developed giving a reduction factor of 50, 100, 200 and 400. Though not decided upon at the time of writing, the robust step of the trigger might be eliminated. As a result, cuts can be performed immediately on the track fitted step. Like in the standard settings, the RICH cuts are always performed at the end.

The choice of reduction factors 50, 100, 200 and 400 are given by the HLT group. In order to attain a flexible set of settings for the HLT2 trigger, several standard scenarios have been created. Three types of trigger setups have been chosen: charm, leptonic and hadronic. In the first two the inclusive ϕ trigger is given 5% of the bandwidth while in the last it has 10%. Furthermore, three HLT2 overall reduction factors are used: 5, 10 and 20. Combining these scenarios gives the reduction factors 50, 100, 200 and 400 for inclusive ϕ depending on HLT2 settings. For example hadronic setup with reduction factor 10 requires an inclusive ϕ reduction factor of 100.

Unlike the optimization performed on the standard setup, for the alternative lines all parameters can be considered simultaneously as no stepped procedure is required. The optimization procedure, however, is the same as previously shown. I.e. the efficiency is based on a pre-selection by the relevant physics analysis group. The optimization for the alternative lines has been performed on the MC09 simulated data sample, thus differences between the standard and alternative lines come from both changes in cuts as well as the software involved.

As before the cuts were determined using efficiency versus reduction rate plots, aiming for the relevant reduction factor while optimizing the efficiency. Due to wishes from the physics groups a wider mass window was used for these lines than in the previously shown standard settings. The cuts used are shown in table 7.7 giving the efficiencies shown in table 7.8. The related efficiency plots are given in appendix B.

7.10 Status of the Inclusive ϕ Trigger Line

The inclusive ϕ trigger has been included as a standard component of the HLT2 trigger. For the 2010 data HLT2 was run in a “pass-through” mode as the data rate was not high enough to justify the use of the full trigger system. However, the inclusive ϕ

Table 7.7: Alternative cut values. Cuts are directly performed on the Kalman fitted tracks. Reduction factors 50, 100, 200 and 400 are shown.

Variable	Factor 50	Factor 100	Factor 200	Factor 400
Kaon Imp. Par. Sig.	$> 2 \sigma$	$> \sqrt{6.25} \sigma$	$> 3 \sigma$	$> 4 \sigma$
ϕ Vertex χ^2	< 25	< 25	< 25	< 25
ϕ Mass Win.	$\pm 20 \text{ MeV}/c^2$	$\pm 20 \text{ MeV}/c^2$	$\pm 20 \text{ MeV}/c^2$	$\pm 20 \text{ MeV}/c^2$
ϕP_T	$> 0.6 \text{ GeV}/c$	$> 0.7 \text{ GeV}/c$	$> 0.9 \text{ GeV}/c$	$> 1.2 \text{ GeV}/c$
Kaon $\Delta \log \mathcal{L}_{x-y}$	> 0	> 0	> 0	> 0

Table 7.8: Alternative inclusive ϕ cut efficiencies. Reduction factors 50, 100, 200 and 400 are shown.

Channel	Factor 50	Factor 100	Factor 200	Factor 400
$B_s \rightarrow \phi\phi$	97%	96%	95%	93%
$B_s \rightarrow \phi\gamma$	91%	91%	91%	90%
$B_s \rightarrow D_s\pi$	34%	34%	33%	30%
$B_s \rightarrow J/\psi\phi$	70%	68%	64%	56%

trigger has been seen to work well within the online environment and is ready for usage in future data taking periods.

As mentioned, the selection efficiency optimization of the inclusive ϕ trigger is based on simulated interaction events and the expected detector reaction to this. Current calibration procedures based on recorded data aim to improve and validate, amongst others, particle tracking and RICH information generation. The results of the calibrations are included in the simulation framework as they become available, resulting in improved accuracy of the simulated data. A re-assessment of the inclusive ϕ trigger cuts should be performed when RICH calibration has been concluded. The trigger line is fully usable in its current configuration, though the calibration is crucial for gaining a full understanding of selection efficiencies and purity.

Through being the most efficient trigger line for multiple key channels the inclusive ϕ compensates well for its relative high computing resource consumption. Furthermore, due to the stepped design of the trigger line, the rate of events arriving at the RICH algorithms can be tweaked in order to adjust the resource consumption to a given level. This can be of importance if the particle flux in the experiment differs from the expected, as the RICH algorithm calculation time is sensitive to particle multiplicity in the event. Through the flexibility of the stepped design the applicability of the line is assured even in unexpected conditions.

The inclusive ϕ trigger fits well with the current HLT2 philosophy of using generic inclusive triggers as opposed to channel specific exclusive triggers, and should be well suited for further data taking at 3.5 TeV as well as future 7 TeV runs.

Chapter 8

Conclusions

In the context of this thesis, the development of the software components related to the simulation of machine induced background in the LHCb experiment has been conducted. This involves the development of a custom generation tool for the Gauss simulation application able to import, parse and generate particle showers in a way consistent with external estimates and user definable options. Though any particle distribution can be imported into the generator, the re-creation of machine induced background showers entering the experiment is the main use case.

A complete chain of software components is available for the full estimation and simulation of background sources for the LHCb experiment. This ranges from the estimation of initial proton losses, the transport of the resulting particle shower towards the experiment to their impact on the various detector systems. This novel multi-stepped approach is currently fully implemented, having provided various estimates for multiple machine induced background sources and energy levels. The software is ready for the simulation of future conditions, in particular the nominal energy upgrade of 2013.

The effect of machine induced particles on the experiment has been investigated for various energy level and conditions with an aim to understand the expected particle rates and distributions, as well as their effect on the LHCb trigger. An event selection procedures has been developed in order to separate the relevant particle sources from each other in order to measure their respective signal fraction and overall rates. Current estimates show the machine induced background rate to be comparatively low, though small changes in collimation efficiency or vacuum conditions can result in significant contributions.

Unwarranted Level Zero trigger responses due to machine induced background has been investigated for various energy level and trigger settings. At the expected background levels, the trigger rate increase caused by these particles is negligible. However, single machine induced background events are seen to have a trigger probability comparable to that of normal proton-proton events. An increase of machine induced background events can be caused by various effects, depending on source type. Keeping the machine induced background rate under control and understanding the various sources

involved is thus essential in order to understand and avoid problems with the trigger rate.

To protect the experiment from machine induced background and beam related failure scenarios, the beam condition monitor has been created. The Beam Condition Monitor has been created to protect the detector elements close to the IP and thus the device has been placed upstream and downstream of this position.

In this thesis it has been shown that the Beam Condition Monitor positions are well chosen as the coverage range of the devices is sufficient for all expected failure scenarios. As the Beam Condition Monitor is able to dump the beam, signal threshold for this action must be determined. The thresholds have been determined through simulations, and current experience with beam in the machine show that the device has successfully dumped the beam when appropriate with no false positives occurring.

For the Beam Condition Monitor simulations an extension of the LHCb detector description with the associated magnetic fields as well as particle generator tools and Beam Condition Monitor specific software has been developed and is available to the collaboration in the standard LHCb software.

The high level trigger of the LHCb experiment contains multiple selection lines. In this thesis the development of the inclusive ϕ trigger line has been shown. This line aims to reconstruct the decay $\phi \rightarrow K^+ K^-$ where ϕ is the daughter of a B -meson decay. This is characteristic of several of the key channels of the LHCb physics program, making the trigger line of utmost relevance.

Due to certain computing intense algorithms, the line uses a triple stage approach. Each step demands more computing time per event than the last, though fewer candidate events arrive at each step. The three steps are robust cuts, using simple particle reconstruction and kinematic cuts. Track fitted, improving on the reconstruction and utilizing error based cuts. And finally, particular to the inclusive ϕ trigger, the RICH step, utilizing the LHCb ring imaging Cherenkov detectors to separate the relevant kaons in the decay from the abundance of pions in an average LHCb event.

The inclusive ϕ trigger has been shown to be effective on multiple decay channels while keeping a low trigger rate and an acceptable computation time. In addition to the optimized standard set of cuts, a set of alternatives have been investigated in order to cover various trigger setup possibilities.

During the 2010 data taking the inclusive ϕ trigger was part of the High Level Trigger 2. Though the High Level Trigger 2 did not filter events and was in a “pass-through” mode at this time, it shows that the trigger line is fully functional in an online environment and can be utilized in future data taking.

Appendix A

Acronym List

BB	Beam-Beam
BCM	Beam Condition Monitor
BCMU	Upstream Beam Condition Monitor
BCMD	Downstream Beam Condition Monitor
BE	Beam-Empty
BG	Beam-Gas
BIS	Beam Interlock System
CERN	European Organization for Nuclear Research
CKM	Cabibo-Kobayashi-Maskawa
CPV	CP Violation
CVD	Chemical Vapor Deposition
DDDB	Detector Description DataBase
DOCA	Distance of Closest Approach
EB	Empty-Beam
ECAL	Electromagnetic CALorimeter
GEM	Gas Electron Multiplier
HCAL	Hadronic CALorimeter
HH	Horizontal Halo
HLT	High Level Trigger
IP	Interaction Point
IR	Interaction Region
IT	Inner Tracker

L0	Level Zero Trigger
LEP	Large Electron Positron Collider
LHC	Large Hadron Collider
LHCb	Large Hadron Collider beauty experiment
LSS	Long Straight Section
MB	Minimum Bias
MC	Monte Carlo
MIB	Machine Induced Background
MWPC	Multi Wire Proportional Chamber
OT	Outer Tracker
PID	Particle ID
PS	Preshower Detector
PU	Pile Up
PV	Primary Vertex
RF	Radio Frequency
RICH	Ring Imaging Cherenkov Detector
SPD	Scintillator Pad Detector
TCK	Trigger Configuration Key
TCT	Tertiary Collimator
TCTH	Horizontal Tertiary Collimator
TCTV	Vertical Tertiary Collimator
TT	Tracker Turicensis
VELO	VErtex LOcator
VH	Vertical Halo

Appendix B

**Inclusive ϕ Trigger Optimization
Plots for Reduction Factor 50,
100, 200 and 400**

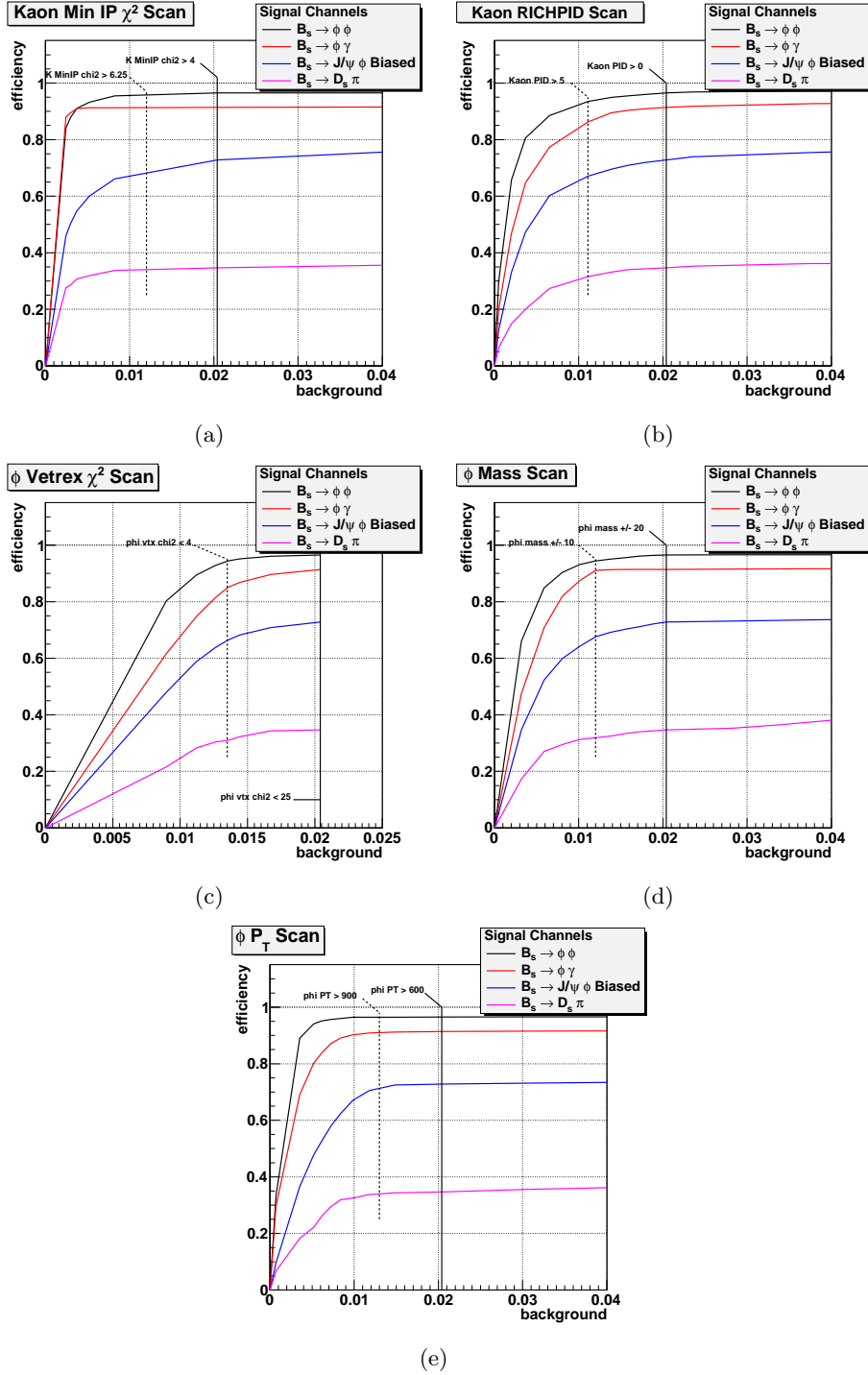


Figure B.1: Factor 50 cut efficiency plots. The plots show the selection efficiency versus trigger rate for a given signal sample as the cut variable is varied. The vertical line indicates the cut value chosen. Figure B.1(a), B.1(b), B.1(c), B.1(d) and B.1(e) show variations on Kaon impact parameter significance, Kaon RICH PID, ϕ vertex χ^2 , ϕ mass and ϕ P_T respectively.

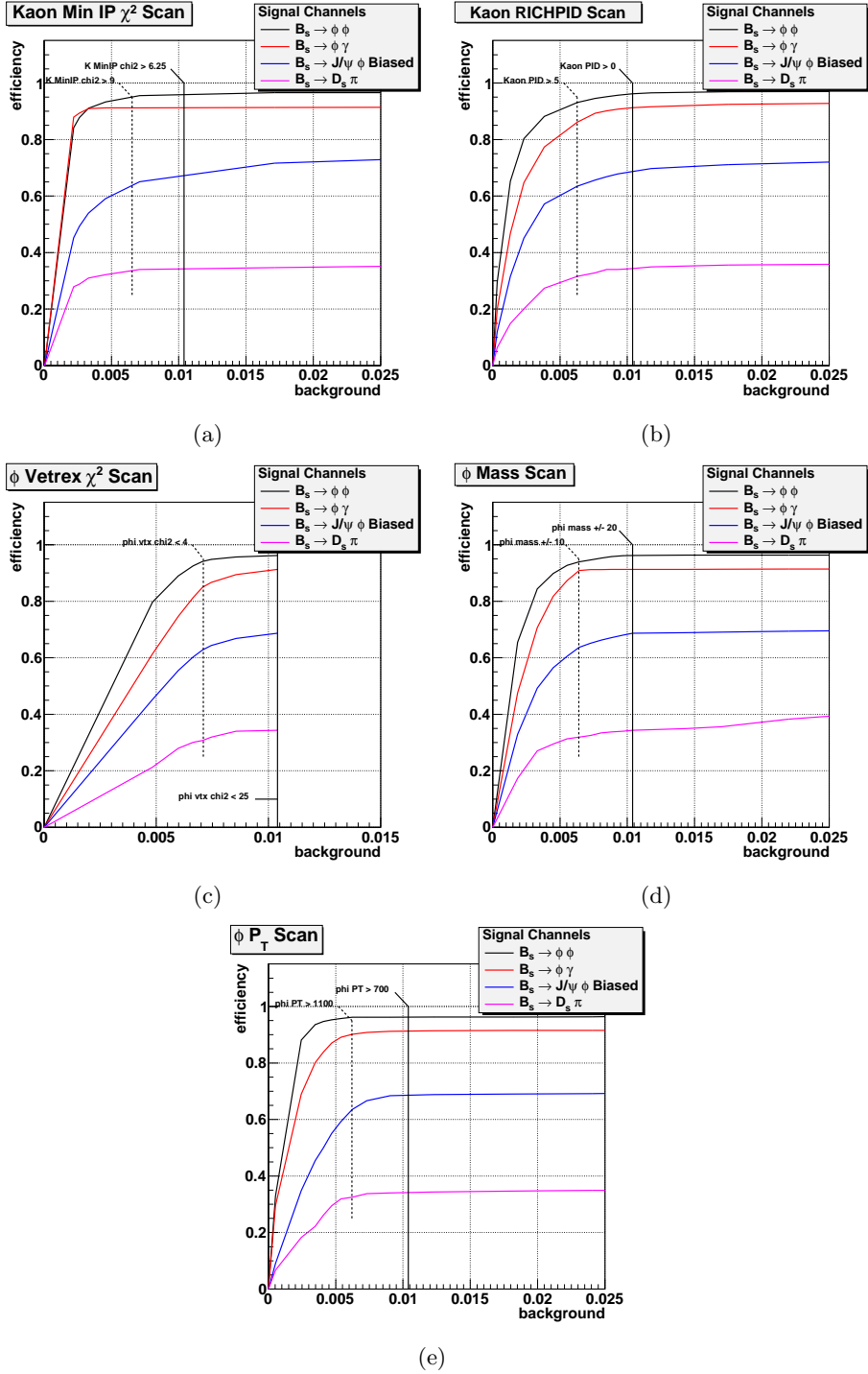


Figure B.2: Factor 100 cut efficiency plots. The plots show the selection efficiency versus trigger rate for a given signal sample as the cut variable is varied. The vertical line indicates the cut value chosen. Figure B.2(a), B.2(b), B.2(c), B.2(d) and B.2(e) show variations on Kaon impact parameter significance, Kaon RICH PID, ϕ vertex χ^2 , ϕ mass and ϕ P_T respectively.

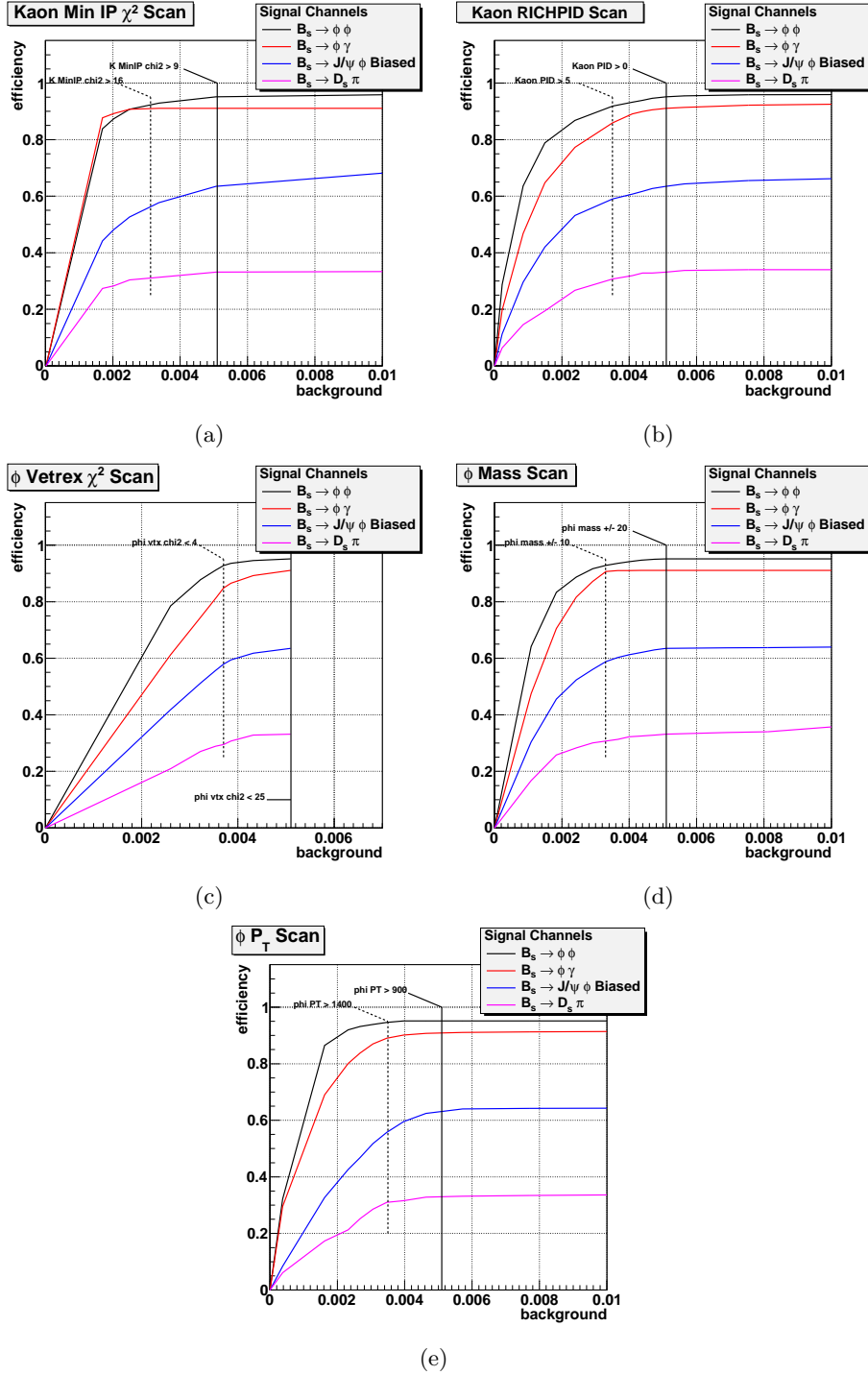


Figure B.3: Factor 200 cut efficiency plots. The plots show the selection efficiency versus trigger rate for a given signal sample as the cut variable is varied. The vertical line indicates the cut value chosen. Figure B.3(a), B.3(b), B.3(c), B.3(d) and B.3(e) show variations on Kaon impact parameter significance, Kaon RICH PID, ϕ vertex χ^2 , ϕ mass and ϕP_T respectively.

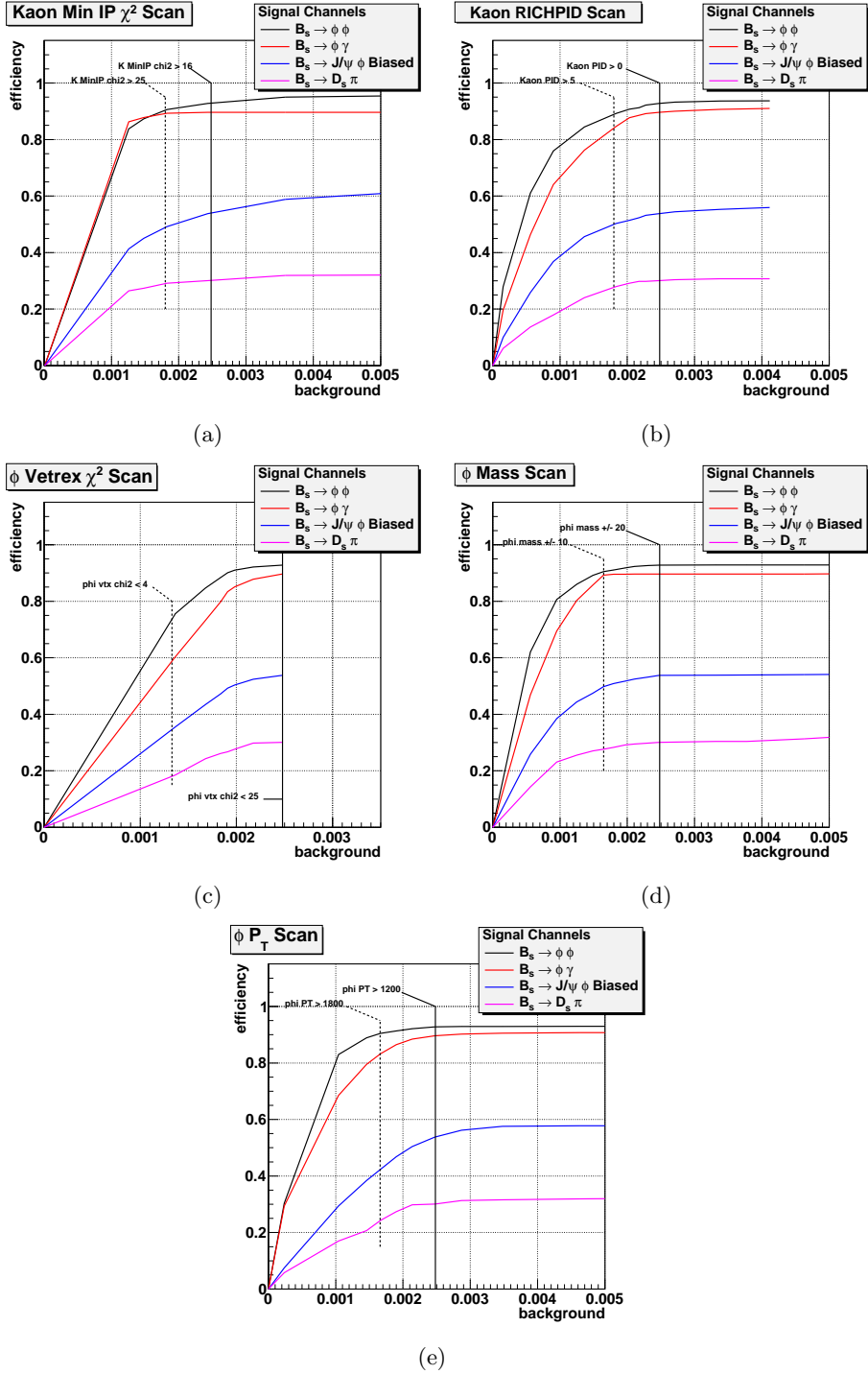


Figure B.4: Factor 400 cut efficiency plots. The plots show the selection efficiency versus trigger rate for a given signal sample as the cut variable is varied. The vertical line indicates the cut value chosen. Figure B.4(a), B.4(b), B.4(c), B.4(d) and B.4(e) show variations on Kaon impact parameter significance, Kaon RICH PID, ϕ vertex χ^2 , ϕ mass and ϕ P_T respectively.

Acknowledgements

There are several people that have aided me through these last few years both professionally and personally, and I would like to take this opportunity to show them my gratitude.

Firstly I would like to thank Herr Prof. Dr. Spaan for giving me the opportunity to participate to the LHCb experiment, enabling me to work at the forefront of modern science. For the fruitful cooperation during the BCM development I give my thanks to Christoph Ilgner and Sebastian Schleich and others at EV. In particular I would like to thank Gloria Corti for helping me get the grips on the LHCb software and aiding me in the work related to BCM and MIB. This also goes out to the other members of the B&B Working group, especially Vadim Talanov and Robert Appleby. For the cooperation on the Inclusive ϕ trigger I thank Kim Vervink and the HLT group.

Furthermore, to all my friends and family in Norway, Germany, France and Switzerland I would like to show my appreciation for their support and understanding even when they could not comprehend my work. By providing weekly distractions and pizza, Halo-Night has been a welcome variation to the daily work routine.

Finally, I would like to give all my gratitude to my girlfriend Natacha who has given me support, patience and love through the last five years and has made me strive to reach my goals.

This work has been supported by Bundesministerium für Bildung und Forschung.

Vit han tarv
som vidt skal fara;
d'er mangt heime høvelig.
Til bisn han vert
som veit for lite,
når han sit med kloke folk
saman.

Bibliography

- [1] J. Dunkley, E. Komatsu, M. R. Nolte, D. N. Spergel, D. Larson, G. Hinshaw, L. Page, C. L. Bennett, B. Gold, N. Jarosik, J. L. Weiland, M. Halpern, R. S. Hill, A. Kogut, M. Limon, S. S. Meyer, G. S. Tucker, E. Wollack, and E. L. Wright. Five-year wilkinson microwave anisotropy probe observations: Likelihoods and parameters from the WMAP data. *The Astrophysical Journal Supplement Series*, 180(2):306, 2009.
- [2] A.D. Sakharov. Violation of CP invariance, C asymmetry, and baryon asymmetry of the universe. *Journal of Experimental and Theoretical Physics Letters*, 5:24–27, 1967.
- [3] M.B. Gavela, M. Lozano, J. Orloff, and O. Pène. Standard model CP-violation and baryon asymmetry (i). zero temperature. *Nuclear Physics B*, 430(2):345 – 381, 1994.
- [4] M.B. Gavela, P. Hernandez, J. Orloff, O. Pène, and C. Quimbay. Standard model CP-violation and baryon asymmetry (ii). finite temperature. *Nuclear Physics B*, 430(2):382 – 426, 1994.
- [5] S. Scheich, T. Brambach, J. Wishahi, and M. Lieng. CP Asymmetries in $B_s \rightarrow \phi\phi$. In *3rd Annual Workshop of the Helmholtz Alliance. Physics at the Terascale*, 2009.
- [6] O.S. Bruning, P. Collier, P. Lebrun, S. Myers, R. Ostojic, J. Poole, and P. Proudlock. *LHC Design Report*. CERN, Geneva, 2004.
- [7] L. Evans and P. Bryant. LHC machine. *Journal of Instrumentation*, 3(08):S08001, 2008.
- [8] CERN. CERN Web. www.cern.ch.
- [9] R.W. Assmann, F. Schmidt, F. Zimmermann, and M.P. Zorzano-Mier. Equilibrium beam distribution and halo in the LHC. oai:cds.cern.ch:569470. (CERN-LHC-Project-Report-597. CERN-LHC-Project-Report-592.):4 p, Jul 2002.
- [10] J.B. Jeanneret. A specification for the momentum cleaning. Technical Report LHC-Project-Note-115, CERN, Geneva, Oct 1997.

- [11] B. Todd, R. Schmidt, and C. Da Via. *A Beam Interlock System for CERN High Energy Accelerators*. PhD thesis, Brunel Univ., 2006.
- [12] J.H. Christenson, J.W. Cronin, V.L. Fitch, and R. Turlay. Evidence for the 2π decay of the k_2^0 meson. *Phys. Rev. Lett.*, 13(4):138–140, Jul 1964.
- [13] M. Kobayashi and T. Maskawa. CP-violation in the renormalizable theory of weak interaction. *Progress of Theoretical Physics*, 49(2):652–657, 1973.
- [14] L. Wolfenstein. Parametrization of the kobayashi-maskawa matrix. *Phys. Rev. Lett.*, 51(21):1945–1947, Nov 1983.
- [15] LHCb Collaboration. *LHCb reoptimized detector design and performance: Technical Design Report*. Technical Design Report LHCb. CERN, Geneva, 2003.
- [16] The CKMfitter Group. CKM Fitter. <http://ckmfitter.in2p3.fr>.
- [17] LHCb Collaboration. Roadmap for selected key measurements of LHCb. 2009.
- [18] J. Wishahi. Opposite side flavour tagging with charged b decay channels at the LHCb experiment — integration of the sherpa MC-generator into the LHCb software framework, 2008.
- [19] R. Lindner. Definition of the coordinate system. Technical Report LHCB-C-EN-0001, EDMS-372642, CERN, 2003.
- [20] LHCb Collaboration. The LHCb detector at the LHC. *Journal of Instrumentation*, 3(08):S08005, 2008.
- [21] LHCb Collaboration. *LHCb VELO (VERtEx LOcator): Technical Design Report*. Technical Design Report LHCb. CERN, Geneva, 2001.
- [22] LHCb Collaboration. *LHCb RICH: Technical Design Report*. Technical Design Report LHCb. CERN, Geneva, 2000.
- [23] LHCb Collaboration. *LHCb magnet: Technical Design Report*. Technical Design Report LHCb. CERN, Geneva, 1999.
- [24] LHCb Collaboration. *LHCb inner tracker: Technical Design Report*. Technical Design Report LHCb. CERN, Geneva, 2002.
- [25] LHCb Collaboration. *LHCb outer tracker: Technical Design Report*. Technical Design Report LHCb. CERN, Geneva, 2001.
- [26] LHCb Collaboration. *LHCb muon system: Technical Design Report*. Technical Design Report LHCb. CERN, Geneva, 2001.
- [27] LHCb Collaboration. *LHCb calorimeters: Technical Design Report*. Technical Design Report LHCb. CERN, Geneva, 2000.

- [28] LHCb Collaboration. *LHCb trigger system: Technical Design Report*. Technical Design Report LHCb. CERN, Geneva, 2003.
- [29] CERN. Gaudi web page. <http://cern.ch/proj-gaudi>.
- [30] The LHCb Collaboration. *LHCb computing: Technical Design Report*. Technical Design Report LHCb. CERN, Geneva, 2005.
- [31] CERN. Gauss web page. <http://cern.ch/LHCb-release-area/DOC/gauss>.
- [32] T. Sjostrand, S. Mrenna, and P.Z. Skands. PYTHIA 6.4 Physics and Manual. *JHEP*, 05:026, 2006.
- [33] J. Allison, K. Amako, J. Apostolakis, et al. Geant4 developments and applications. *Nuclear Science, IEEE Transactions on*, 53(1):270–278, feb. 2006.
- [34] G. Corti, L. Fernández, P. Robbe, and O. Schneider. Monte carlo event type definition rules. Technical Report LHCb-2005-034. CERN-LHCb-2005-034, CERN, Geneva, Jul 2005. revised version submitted on 2007-01-19 09:25:51.
- [35] Ch. Ilgner et al. The Beam Conditions Monitor of the LHCb Experiment. 2010.
- [36] W. Kalbreier, G. de Rijk, D. Gerard, V. Petrov, and A. Soukhanov. Technical specification for the MBXW resistive dipole magnets for the LHC insertions. Technical Report LHC-MBXW-CA-0002, EDMS-316620, CERN, 2001.
- [37] CERN. LHC Optics Web. www.cern.ch/lhcoptics.
- [38] CERN. LHC Beam-Gas Background Web. <http://project-lhc-bkg-sim.web.cern.ch/project-LHC-bkg-sim/>.
- [39] G. Robert-Demolaize, R.W. Assmann, S. Redaelli, and F. Schmidt. A new version of sixtrack with collimation and aperture interface. Technical Report CERN-AB-2005-033, CERN, Jul 2005.
- [40] CERN. LHC Collimation Group Web. <http://lhc-collimation-project.web.cern.ch>.
- [41] S. Roesler, R. Engel, and J. Ranft. The monte carlo event generator DPMJET-III. In *Proc. of the Monte Carlo 2000 Conference, Lisbon*, pages 1033–1038, 2000.
- [42] A. Rossi and N. Hilleret. Residual gas density estimations in the LHC experimental interaction regions. Technical Report LHC-Project-Report-674. CERN-LHC-Project-Report-674, CERN, Geneva, Sep 2003.
- [43] R.B. Appleby, Y.I. Levinsen, and H. Burkhardt. Beam-gas simulations for 2009 LHC running and first comparisons with data. Technical Report LHC-Project-Note-429. CERN-LHC-Project-Note-429, CERN, Geneva, Feb 2010.
- [44] R.B. Appleby and A. Mereghetti. The FLUKA model of ir8. Technical Report LHC-Project-Note-427. CERN-LHC-Project-Note-427, CERN, Geneva, Feb 2010.

- [45] A. Ferrari, P.R. Sala, A Fassò, and J. Ranft. *FLUKA: A multi-particle transport code (program version 2005)*. CERN, Geneva, 2005.
- [46] G. Corti, R.B. Appleby, H. Burkhardt, Y.I. Levinsen, M H Lieng, and V Talanov. Simulation of machine background in the LHCb experiment: Methodology and implementation. Dec 2010.
- [47] I. Antcheva, M. Ballintijn, B. Bellenot, M. Biskup, R. Brun, N. Buncic, Ph. Canal, D. Casadei, O. Couet, V. Fine, L. Franco, G. Ganis, A. Gheata, D. Gonzalez Maline, M. Goto, J. Iwaszkiewicz, A. Kreshuk, D. Marcos Segura, R. Maunder, L. Moneta, A. Naumann, E. Offermann, V. Onuchin, S. Panacek, F. Rademakers, P. Russo, and M. Tadel. ROOT – a C++ framework for petabyte data storage, statistical analysis and visualization. *Computer Physics Communications*, 180(12):2499 – 2512, 2009.
- [48] X.N. Wang and M. Gyulassy. HIJING: A Monte Carlo model for multiple jet production in p p, p A and A A collisions. *Phys. Rev.*, D44:3501–3516, 1991.
- [49] CERN. Field Description for LHC Web. www.cern.ch/fidel.
- [50] P. Burchat A.J. Edwards, M. Bruinsma. Radiation monitoring with CVD diamonds in BABAR. *Nuclear Instruments and Methods in Physics Research A*, 552:176–182, 2005.
- [51] S. Schleich C. Ilgner, M. Lieng. Beam-dump logic of the LHCb beam-conditions monitor system. Technical Report EDMS-904972, Technische Universitaet Dortmund, 2008.
- [52] R.B. Appleby. LHCb injected beam accidents. Technical report, CERN, 2008.
- [53] S. Hansmann-Menzemer. HLT2 tracking compared to off-line, 2008. <http://indico.cern.ch/conferenceDisplay.py?confId=42082>.
- [54] T Brambach, M Kaballo, T M Karbach, F Kruse, J Merkel, S Schleich, and J Wishahi. Measurement of the inclusive ϕ cross section in pp collisions at $\sqrt{s} = 7$ tev. Nov 2010.
- [55] M. Adinolfi, N. Brook, R.W. Forty, M. John, J. Libby, B. Simmons, and G. Wilkinson. A simulation study of the LHCb RICH performance. Technical Report LHCb-2000-066, CERN, Geneva, Jun 2001. revised version number 1 submitted on 2001-06-07 11:17:26.
- [56] M. Patel. An inclusive ϕ stream for the LHCb high level trigger. Technical Report LHCb-2006-041. CERN-LHCb-2006-041, CERN, Geneva, Jul 2006.
- [57] M. Lieng. An inclusive phi stream for the LHCb high level trigger, DC06 analysis. Technical Report LHCb-2009-010. CERN-LHCb-2009-010, CERN, Geneva, Jan 2009.

- [58] C. Lazzeroni, C. Jones, R. Muresan, G. Wilkinson, R W Forty, and M Patel. Reconstruction and calibration strategies for the LHCb rich detector. 2006.
- [59] P. Koppenburg. An introduction to hlt lines. <https://indico.cern.ch/conferenceDisplay.py?confId=87097>.
- [60] M Gersabeck. Lhcb tracking, alignment and physics performance. oai:cds.cern.ch:1314528. Dec 2010. LHCb-TALK-2010-052.
- [61] S. Nies. Hlt1 timing performance. <https://indico.cern.ch/conferenceDisplay.py?confId=58528>.